MCCXXII

Università degli Studi di Padova

Department of Information Engineering

Master Thesis in Telecommunication Engineering

Reconfigurable Leaky Wave Antenna based on Metamaterial Substrate Integrated Waveguide for 5G oriented beamsteering application

Master Thesis based on an internship at Adant Technologies Inc.

Supervisor:

Prof. Andrea Galtarossa

Co-Supervisor:

Ing. Mauro Facco

Master Candidate:

Guglielmo Fortuni

ID 1128006

Padova, April 9, 2018

Academic year 2017/2018

Abstract

This work presents the study and the development of a Leaky Wave Antenna, based on a Composite Right-Left Handed transmission line and a Substrate Integrated Waveguide. The antenna system is designed to work in the frequency band of 26 GHz - 30 GHz, demonstrates beamsteering functionalities and a high gain. The conducted study is envisioned in the background of the fifth generation mobile networks (5G), in order to fulfil the requirements for the realization of a small cell antenna.

Sommario

Questa tesi tratta lo studio e lo sviluppo di un’antenna di tipo Leaky Wave, basata su una linea di trasmissione Composite Right-Left Handed e una guida di tipo Substrate Integrated Waveguide. Il sistema d’antenna è disegnato per funzionare nella banda di frequenze dai 26 GHz ai 30 GHz, dimostra funzionalità di beamsteering e un alto guadagno. Lo studio realizzato è inquadrato nell’ottica della quinta generazione di rete mobile (5G), in modo da soddisfare i requisiti per la realizzazione di un’antenna per small cell.

Contents

List of Figures

Acronyms

3GPP 3rd Generation Partnership Project.

AR Axial Ratio.

BS Base Station.

CRLH Composite Right-Left Handed.

DL Downlink.

eMBB Enhanced Mobile Broadband.

FWHM Full Width at Half Maximum.

HMSIW Half-Mode Substrate Integrated Waveguide.
HPBW Half Power Beam Width.

IMT-2020 International Mobile Telecommunication-2020.
IMT-A IMT Advanced.
IoT Internet of Things.
ITU International Telecommunications Union.

LH Left Handed.
LOS Line Of Sight.
LTE-A Long Term Evolution Advanced.
LWA Leaky Wave Antenna.

M2M Machine-to-Machine.
MBA Multi-Beam Antenna.

MIMO Multiple-Input Multiple-Output.
mmWave Millimetre Wavelength radio frequencies.
MTC Machine Type Communication.
MTM Metamaterial.

NFV Network Function Virtualization.
NLOS Non Line Of Sight.
NRI Negative Refractive Index.

OFDM Orthogonal Frequency Division Multiplexing.

PCB Printed Circuit Board.

QoE Quality of Experience.

RH Right Handed.
RTT Round Trip Time.
RWG Rectangular Waveguide.

SCMA Sparse Code Multiple Access.
SDN Software Defined Networking.
SINR Signal to Interference plus Noise Ratio.
SIW Substrate Integrated Waveguide.
SLL Side Lobe Level.

TL Transmission Line.

UE User Equipment.
UL Uplink.
uRLLC Ultra-Reliable and Low Latency Communications.

Introduction

The **fifth generation mobile networks (5G)** is the last generation of mobile connectivity, and it's raising a lot of interest in many engineering fields, together with a strong push to the scientific community. To support the development of mobile internet, 5G networks will increasingly become the primary means of network access for person-to-person and person-to-machine connectivity. The new system will need to match various service requirements and characteristics, besides the classical increase of bit-rate speed. Three main goals have been established: extreme broadband connectivity, massive number of connection, ultra-low latency.

The 5G mobile network indeed will provide a higher data transmission speed, in the order of the Gb/s for a single user, sensibly increasing the experienced bit-rate. The service will be diversified in order to be able to connect at the same time users and massive numbers of machine-type equipments, e.g. sensors and Internet of Things (IoT) devices. These indeed will become more pervasive and integrated in our lives, and will work thanks to a Machine-to-Machine (M2M) connection that should support a high devices density per area. Finally, through an optimized network architecture, the latency (i.e. the end-to-end delay of the connectivity) will be lowered enough to reach the threshold of 1 ms, to enable services like autonomous driving, tactile internet, and remote control of machineries.

Particularly regarding the **Enhanced Mobile Broadband (eMBB)** aspect, the use of wide frequency bands will be fundamental, to allow, together with a higher spectral efficiency, an increase in the data transmission speed. For this reason, the system will move from traditional frequencies, that however will be used and revised, shifting to less overcrowded higher frequencies, in order to have available larger chunk of spectrum. A highly interesting spectrum is the so-called band of **Millimetre Wavelength radio frequencies (mmWave)**, that comprehends approximately the frequencies from 3 GHz to 300 GHz, and in particular the portion 26 GHz - 30 GHz, that will be our target band.

As well known, higher frequency means smaller wavelength, thus arises the drawback of a greater free space attenuation and significant blocking due to buildings, concrete walls, and the user itself. Therefore, the communication range will be shortened, leading to the deployment of a large number of *small* and *pico* cells, that will support also M2M and IoT connectivities since these devices use low-powered and short-range wireless transmissions.

Small cells working at mmWave frequencies cannot rely on traditional antennas, like those already used in the mobile network, because of the propagation issues related to this band. To make the connectivity efficient and adequate, it's necessary that the radiating elements provide a high directivity beam, in such way the antenna gain will increase and the radiated EM energy will be concentrated in the desired direction. If the beam becomes narrower, in order to serve a significant number of devices with a single Base Station (BS), we must enable a **beamsteering** capability in the antenna system. This means that the beam can be pointed in different directions, moving in one or two planes and varying the angle of maximum irradiation, through an analog or digital control. These small cells therefore will use a narrow beam shape, reconfigurable and with high gain, that can be steered to the desired directions. In this way, besides overcoming the characteristic issues of mmWave propagation, the antennas will provide also a higher Signal to Noise Ratio (SNR), essential to get Gb/s bitrate.

This is the general background in which the thesis will settle. The objective is therefore the development of an antenna that demonstrates a high gain, a narrow and reconfigurable beam, and that works at a fixed frequency in the band 26 GHz - 30 GHz. Moreover, the solution should be low-cost and suitable for a large scale production, expecting a possible commercial diffusion. The peak gain must be in the order of 15-20 dBi, and the indicative beamsteering range of 30°. The antenna should guarantee the good functioning on a wide bandwidth, approximately of 1 GHz, and must be possible its integration with other elements in order to compose an array-like structure that increases the maximum gain, enables a 2-plane beamsteering, and provides Multi-User Multiple-Input Multiple-Output (MU-MIMO).

In collaboration with Adant Technologies, we opt for an innovative solution: a **Leaky Wave Antenna (LWA)**, based on a **Composite Right-Left Handed (CRLH)** Transmission Line (TL) (i.e. a Metamaterial TL), developed on a **Substrate Integrated Waveguide (SIW)**. This configuration has been chosen because it can provide some advantages with respect to traditional antennas. Firstly, with the LWA we can get a high gain (that moreover can be adjusted, as we will see in the results chapter) with a relatively simple structure, avoiding the need of antennas array. This type of antenna provides intrinsically a beamsteering functionality, thanks to its EM characteristics and in particular the behaviour of the phase constant, with a main beam that changes direction with the frequency sweep. Clearly our goal is to steer the beam at a fixed frequency, to do this, the CRLH structure will be perturbed with **varactor diodes**, i.e. variable capacitor voltage controlled. In this way we can change the constitutive parameters of the line, and we'll be able to steer the beam at a fixed working frequency and with a voltage control.

The main advantage is that this is an alternative to traditional phased array, that avoids the use of phase shifters, components that greatly increases the overall production cost and dissipate significant amount of power. Generally the solution is quite innovative since are not present many configurations of LWA on SIW, in particular with varactor tuning at mmWave frequencies. Finally, besides the low-cost and low-power consumption benefits, the large scale production is possible thanks to the planar structure of the SIW, that can be implemented with PCB methods on a traditional substrate.

Clearly there are some drawbacks: in particular the LWA radiates a beam that is frequency variable, therefore using a wide bandwidth the overall pattern will be modified with respect to that of a single frequency. Moreover we encountered some critical issues regarding the varactors placement, since they easily disturb the field propagation and thus degrade the beam. The overall performances depend mostly on the optimization of the unit cell, the element that will be periodically replicated to compose the LWA.
The needed precision on such small features, regarding the size of the antenna, the availability of the varactors, and some timing issues prevented the realization of a prototype, thus unfortunately there are not measured results, but only simulated. The entire design however have been thought in a way that it will be immediately implementable. Generally, the effort has focused on the understanding of which characteristics affect the peak gain, the beam shape, the efficiency, the scanning range, pointing out the antenna trade off, issues and strength.

The thesis is organized as follows:

- **Chapter 1** gives an overview on the incoming 5G system, with its objectives and principal innovations, followed by a resume of the characteristics of mmWave propagation, highlighting advantages and disadvantages. A complete background for the antenna development is thus delineated.

- **Chapter 2** explains the two transmission line technologies that will be used, the SIW and the CRLH. The state of the art will be presented, together with their functioning and characteristics.
  The SIW is a recent type of waveguide, that emulates the rectangular waveguide combining good EM guiding performances with the advantage of a planar structure. It is then particularly suitable for mmWave applications. The CLRH line, with its unique EM characteristics, demonstrates a non linear phase constant, fundamental for the LWA functionalities.

- **Chapter 3** focuses on the Leaky Wave Antenna theory and radiating mechanism, explaining important relations regarding the phase constant and the main beam radiation angle. Moreover will be underlined the characteristics of metamaterial based LWAs, that is the structure that will be implemented.

- In **Chapter 4** the developed antenna system is reported. Initially are explained the steps followed in the antenna design, and which are the fundamental parameters to be observed. Subsequently are presented the two versions of the antenna: the frequency scanning LWA and the varactor tuned LWA.
- Finally, **Chapter 5** reports the simulated results of both the antennas. First the frequency scanning version, then the varactor tuned version, have been analyzed showing the achieved performances, principally in terms of gain and scanning range. In particular, the study has focused on which parameters one can act in order to tune the peak gain and the maximum angle variation, underlining also how the varactor affects the beam pattern.

Chapter 1

5G System and mmWave Communication

1.1 Overview on 5G System

The new generation mobile network recently saw an improvement in its development when, during the plenary meeting of the 3rd Generation Partnership Project (3GPP) TSG RAN (Technical Specification Groups of Radio Access network) in Lisbon, the first implementable non-standalone 5G New Radio specification has been successfully completed [1]. This is a big step forward for the newborn 5G system, having reached a first standard version almost 2 years before the initial commercial deadline, set in the year 2020. After the WRC-15 (World Radio Conference 2015) held in Geneva, another important appointment will be the WRC-19, where, among other studies, frequency bands above 6 GHz will be investigated, standardized and allocated. This acceleration has been possible thanks to the incentive of the biggest player on the market that are waiting for the advent of this new technology, that will bring a big improvement in the world's connectivity.

Other factors that pushed these researches are the incoming sport events of 2018 Olympic Winter Games in Pyeongchang (South Korea), FIFA 2018 World Cup in Russia and 2020 Olympic Games in Tokyo. The organizers promised that during these appointments we will see the first utilization of the new technology, having a huge available audience. For the Olympic Winter Games, Korea Telecom (KT) announced that will deliver the first broad scale 5G network paired with Intel technologies that will enable a series of immersive on-site 5G powered experiences[1].

In this chapter I will give an overview on the main characteristic of the 5G system, focusing on its objective and its enabling technologies, then I will concentrate on the new frequency

---

[1] *Intel to Bring 5G Technologies to Life With Industry Leaders for World's Largest 5G Showcase at Winter Games*, from `https://newsroom.intel.com/editorials/intel-power-5g-network-2018-olympic-games/` (visited on 20-01-2018)

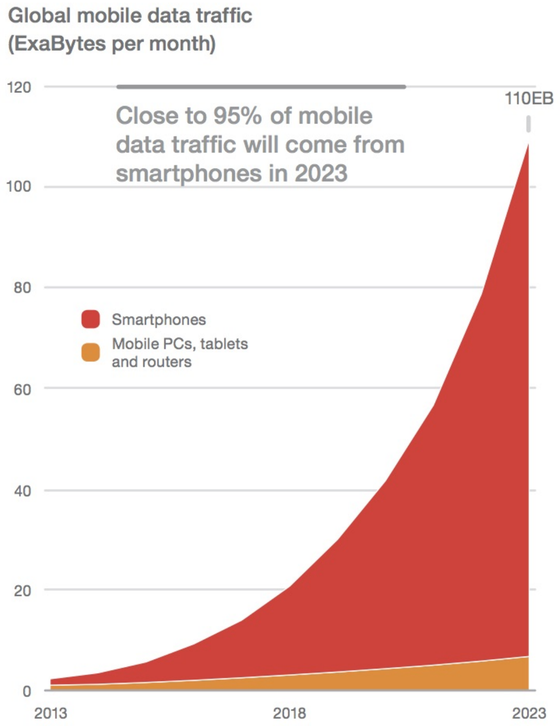

Fig. 1.1: Ericsson forecast on monthly global mobile data traffic, from [2]

bands utilization, Millimetre Wavelength radio frequencies (mmWave), with the related problems and advantages, and finally I will present some existing solution of 5G mmWave antennas.

1.1.1 5G Requirements

The researches and the studies on 5G requirements and goals are driven by forecasts that predict an increase of mobile internet traffic, both human generated and machine generated. According to latest edition of Ericsson Mobility Report [2], the company is expecting 1 billion 5G subscriptions for enhanced mobile broadband by 2023. Ericsson, among other data, analyzed the monthly mobile data traffic per smartphone: North America has the highest usage, with a traffic that was expected to reach 7.1 GB per month per smartphone by the end of 2017 and will increase to 48 GB by the end of 2023. Western Europe has the second highest usage, with traffic expected to reach 28 GB by the end of 2023. We can observe the predicted global traffic in Fig. 1.1, noticing the exponential-like growth. Also, by the same year, over 30 billion connected[2] devices are forecast, of which around 20 billion will be related to the Internet of Things (IoT); at the end of 2017, there are around 0.5 billion

---

[2] Here, we mean connected by one of the available technologies: Wi-Fi, Bluetooth, Zigbee, Sigfox, LoRa, cellular connections, etc.

IoT devices with cellular connections, and this number is projected to reach 1.8 billion in 2023.

These data can demonstrate the size of the phenomena, that will introduce major changes in the telecommunication world. The new mobile communication system, also denominated International Mobile Telecommunication-2020 (IMT-2020) will modify our way of thinking the connectivity [3]. The future network will focus on many business applications and new user experience other than just the increase of bandwidth and data volume. The main change that the new radio technology will enable is the massive presence of Machine-to-Machine (M2M) type of communication, together with the disruptive diffusion of the IoT, two strongly connected aspects. Moreover we will see a big increase of the available bandwidth and then a growth of the experienced bitrate. Therefore, creating a unified platform which is scalable for new applications, services and use cases, will require the development of a new scalable and adaptable air interface and core network. The latest improvement of the evolved IMT Advanced (IMT-A), the ITU denomination for 4G, will prepare the way towards 5G era and provide networking framework to fulfill the needs of new markets.

In the following, we discuss the performance requirements in terms of data rate, latency, network capacity, and energy cost [4–6]. The International Telecommunications Union (ITU) defines 3 main types of use case scenarios for 5G [7]:

- Enhanced Mobile Broadband (eMBB), e.g. smartphones and mobile devices with increased bitrate;
- Ultra-Reliable and Low Latency Communications (uRLLC), e.g. for self-driving car and *Tactile Internet*
- Massive Machine Type Communication (MTC), e.g. for wireless sensor nodes and IoT networks.

In Fig. 1.2 we can observe a schematic overview on 5G application, possibilities and requirements. The three usage scenarios can be used alone or combined as variable new services. eMBB increases the transmission speed over Long Term Evolution Advanced (LTE-A) standard, and will support about 1 Gb/s for both Downlink (DL) and Uplink (UL). This will enable, for example, high definition video transmission such as 4K and 8K display and augmented reality experience. uRLLC aims to eliminate the transmission errors, and decreases the Round Trip Time (RTT). This is required to enable technologies such as round-way gaming, self-driving cars and remote-controlled robotic surgery. MTC will provide infrastructure when almost every device will be connected to the Internet. It should be noted that not all of these performances aspects need to be satisfied simultaneously since different applications have different performance requirements. For example, very high-rate applications such as high definition video streaming may have relaxed latency and reliability

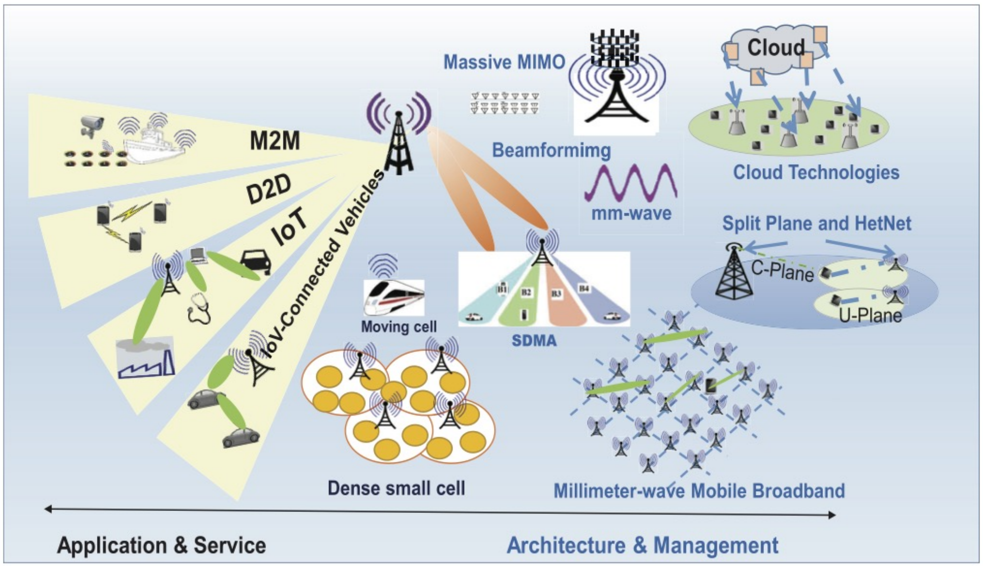

Fig. 1.2: An overview on future 5G network, from [8]

requirements compared to driverless cars or public safety applications, where latency and reliability are extremely important but lower data rates can be tolerated.

The spider diagram shown in Fig. 1.3 is the best way to illustrate the wide range of the 5G requirements in comparison to the previous cellular generation. 5G networks should support [6]:

- **Data Rate**: The available bitrate plays the most significant role in the design of 5G cellular networks since mobile traffic explosion is the main driver behind 5G. Data rate can have a specific target for each metric:

  i) *Edge rate* or *minimum user experienced data rate* is the worst data rate experienced by a user within the range of the network. Targets for the 5G edge rate range from 100 Mb/s to 1 Gb/s. Considering the fact that current 4G systems have a typical edge rate of about 1 to 10 Mb/s, this requirement needs at least 100 times advance.

  ii) *Peak rate* is the best data rate a user can achieve (a marketing number), that likely will be in the range of 10 to 20 Gb/s.

- **Latency**: Current 4G RTT are on the order of 10 - 15 ms, and are based on the 1 ms subframe time with necessary overheads for resource allocation and medium access control. Driven by the emerging new applications, the latency for 5G cellular networks will be below 10 ms, with values around 1 ms for the most demanding application, an order of magnitude better than 4G. In addition to shrinking down the subframe structure, such severe latency constraints may have important implications at several layers of the protocol stack.

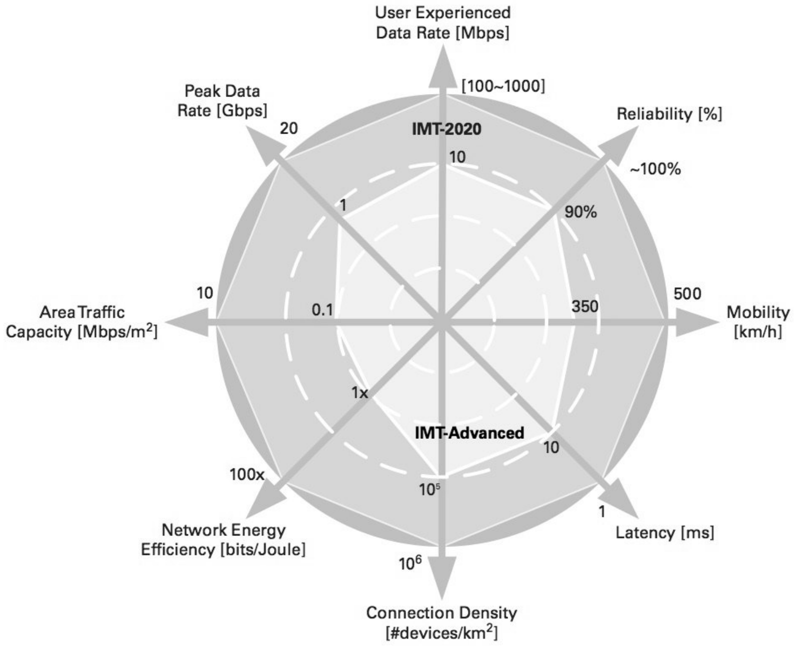

Fig. 1.3: Comparative diagram between IMT-2020 and IMT-A requirements, from [9]

- **Energy** and **Cost**: For 5G cellular networks, it is ideally expected that the per-link energy consumption should decrease. Since data rates being offered will be increasing by about 100 times, this means that the energy consumption per bit and cost per bit need to decrease by at least 99 percentages. Some promising technologies such as mmWave communication and small cell would provide reasonable cost and power scaling.
- **Area Traffic Capacity** and **Density**: Area traffic capacity is defined as the total amount of data that the network can support, characterized in bit/s per unit area. Generally, the aggregate data rate will need to increase by 100 times from 4G to 5G, to enable *infotainment* applications in shopping malls and stadiums. Moreover, for massive IoT and MTC, the network is required to support a number of simultaneous connection 10 times higher than LTE-A, with connection density in the range of 1 million devices per km^2.
- **Mobility**: Communication is required to work up to the speed of 500 km/h to be applicable for magnetic levitation trains and high speed vehicle.

1.1.2 5G Key Technologies

Knowing the features required for the new mobile communication system, it is clear that there are several challenges to address in order to satisfy these requirements. The low latency objective, for example, may require a redesign of the core network. The massive MTC deployment will need cheap electronics and simple networking procedures. The main challenge is however to reach the ultra-high throughput objective. A possible enabler is the use of a new radio access technology combined with the extent to the band of mmWave. Indeed, the spectrum at lower microwave frequencies is very fragmented and overcrowded, and the allocation of large chunks of spectrum (in order to obtain large available bandwidths) is not possible. We will discuss about mmWave topic in section 1.2.

Now we present an overview on some of the technologies that will contribute to the development of 5G networks [10, 11]:

- **Massive MIMO**: Multiple-Input Multiple-Output (MIMO) provides the ability to transmit and receive multiple spatial streams, which multiply the throughput (and therefore spectral efficiency) delivered in the same part of spectrum. The basic principle is to use a high number of antenna elements at the Base Station (BS) that can serve simultaneously tens of users thanks to spatial multiplexing and beamforming. By operating in the mmWave frequency band, it is possible to pack more smaller antennas inside a User Equipment (UE) and in a BS, since the overall dimensions shrink due to smaller wavelength.

  There are several types of MIMO: Single User and Multi User MIMO (SU-MIMO and MU-MIMO), where multiple stream are used to enhance the connectivity of one or more users; Full Dimensional or 3D-MIMO, where narrow beams are optimized in both horizontal and vertical planes; Massive MIMO, using up to thousand antenna elements (totally), that can ideally track the user. Massive MIMO is a commercially attractive solution since almost 100 times higher efficiency is possible without installing 100 times more base stations [10]. Limitations can be the need for a timely channel estimation in order to track the user mobility, and the complexity of the radio interface of BS and UE that has to control much more radio signal. Moreover, coordinated multipoint (CoMP) transmission-reception in LTE can support multiple BSs cooperating and acting as a single effective MIMO transceiver, thus some of the interferences in the system are turned into useful signals.

- **Heterogeneous Networks** and **Small Cell**: In order to provide a ubiquitous high Quality of Experience (QoE) gigabit accessibility, 5G small cells can be coupled with the overlaid 4G macro cells. These picocells (range under 200 meters) or femtocells (WiFi-like range), are covered by low-power and low-cost BSs relaying on the same backhaul and access features as macrocells. They primarily provide multi Gb/s throughput with high QoE to mobile users over the bands above 6 GHz. Meanwhile, the 4G BS can serve as a control channel to 5G cells, exploiting the legacy spectrum, to maintain the connection, to perform handover, to provide real-time services. Shorter cell range and dense BS deployment can achieve the spectrum reuse in the whole coverage area and, consequently, fewer number of users will compete for the resources of each BS. Total network capacity vastly increase by shrinking cells and reusing the spectrum, and future nomadic BSs and direct device-to-device connections between UEs are envisioned to emerge in 5G for even greater capacity per user [12]. The antenna presented in this thesis is thought for an application in a picocell capable of beamforming and MIMO technique.

- **New Air Interface**: New air interface consists of building blocks and configuration mechanisms such as adaptive waveform, adaptive frame structure, adaptive coding and modulation family and adaptive multiple access schemes that can improve the network functionality. Various key elements of layer 1 (PHY) and 2 (MAC) will evolve [13]:

  i) Orthogonal Frequency Division Multiplexing (OFDM) is already used in LTE, but has some shortcomings such as out-of-band emission and side lobes, which decrease the spectrum efficiency. In 5G system, the introduction of filtered-OFDM will facilitate the co-existence of different waveforms with different OFDM parameters. For example, a number of sub-band filters can be used to create OFDM subcarrier groupings with different inter-subcarrier spacing, OFDM symbol durations and guard times. By enabling multiple parameter configurations, filtered-OFDM is able to better overall system efficiency and throughput [14].

  ii) Sparse Code Multiple Access (SCMA) is a non-orthogonal waveform that can allow a new multiple access scheme in which sparse codewords of multiple layers of devices are overlaid in code and power domains and carried over shared time-frequency resource. SCMA can support massive connectivity, reduce transmission latency and provide energy saving.

  iii) Polar codes are a major breakthrough in coding theory. A lot of performance simulations show that polar codes concatenated with cyclic redundancy codes (CRC) and an adaptive decoder can outperform turbocodes and Low Density Parity Check (LDPC) codes for short and moderate code block sizes.

iv) Full Duplex (FD) communications: FD breaks the barrier of known TLC by supporting bi-directional communications without time or frequency duplex. The key to achieve FD is to reduce self interference, its dominant issue. In addition to passive methods such as directionality and antenna placement, signal processing is essential to further cancel self-interference both with RF and digital processing.

- **Advanced Networks Architectures**: Novel topologies, such as Software Defined Networking (SDN), where network control is decoupled from forwarding and is directly programmable, or Network Function Virtualization (NFV), which aims at implementing the network functions in software without the need of installation of new equipment, will contribute to significantly reduce the network complexity. This will lower also latency and costs, and will help mobile operators to allocate network resources more efficiently and effectively [8]. At the same time, local caching and edge computing could help to ensure the contents is delivered more quickly to users.

1.2 mmWave Communication and Antennas

The growing traffic demand necessitates an increase of the amount of spectrum that may be utilised by the 5G systems, indeed channel bandwidths will be more than ten times greater than today's LTE 20 MHz cellular channels. The well known portion of frequencies below 3 GHz is already densely occupied, and it is quite difficult to reach target bandwidth of the order of hundreds of MHz. High frequency bands in the so called centimetre wave (cmWave) and millimetre wave (mmWave) range will be adopted due to their potential for supporting wider channel bandwidths and the consequent capability to deliver high data rates. Millimeter wave is precisely the band of spectrum between 30 GHz and 300 GHz, where the free space wavelength $\lambda = c/f$ takes values from 10 mm to 1 mm, hence the name; centimetre wave comprehends the frequencies between 3 GHz and 30 GHz (λ goes from 10 cm to 1 cm). In literature, it is common use to extend the denomination mmWave to both these frequency bands, because electromagnetic waves in these frequency ranges have similar propagating characteristics, and also to highlight the investigation of new portion of spectrum different from the classical cellular frequency (700 MHz, 800 MHz, 1600 MHz, 1900 MHz, etc.),

My thesis' work will be focused on the 26 GHz to 30 GHz range. This is a band of interest since ITU and FCC (U.S. Federal Communication Commission) took steps to facilitate mobile broadband and next generation wireless technologies in frequencies above 24 GHz [15, 16], particularly allocating bands in the portion of 24.25 - 27.5 GHz; 27.5 - 28.35 GHz (FCC); 31.8 - 33.4 GHz and more others above 35 GHz up to 80 GHz.

There are several benefits given by the adoption of such high frequencies, as well as some drawbacks. As we said, the main advantage is the huge frequency allocation, typically of several GHz, that can allow multi Gb/s transmission rates. Moreover, considering that the antenna components scale down with the reduction of λ, the use of massive MIMO is easily implementable since the possibility of packing, in the same physical area, more antennas in UE and BS with respect to a microwave system, enabling multi-stream transmission for high spectrum efficiency and beamforming application. Directional transmission of narrow beams can reduce interference and increase spatial multiplexing capabilities for cellular applications [17]. This helps by focusing energy into smaller regions of space to bring huge improvements in throughput and radiated energy efficiency. MIMO, finally, can facilitate the extensive use of inexpensive low-power components, and allows reduced latency, simplification of the MAC layer, robustness against intentional jamming.

Finally, the problem of high propagation loss can be an advantage if we consider that it allows deploying of overlapping networks that do not interfere each other: spatial frequency reuse result in relatively low multi-user interference, so that more concurrent transmissions can be supported and further improve the aggregate data rate. This will help developing a dense small cell network that exploit directional antenna with high directivity gain.

1.2.1 Propagation Characteristic

Although this new frequency band has gained great interest for 5G cellular systems, there are many concerns about its transmission characteristics. Also the biological safety at mmWave frequencies is under scrutiny [8], indeed for safety concerns non-ionizing and thermal characteristic of mmWaves is analyzed. Apart from this, we report the main propagation issues regarding mmWave propagation for 5G cellular communication [10, 11, 18]:

- **Free Space Path Loss**: In Friis equation (eq. (1.1), where P_r [dBW] is the received power in free space, P_t [dBW] is the transmitted power, G_t [dBi] and G_r [dBi] are the transmit and receive antenna gains, r [m] is the distance between the transmitter and receiver, f_c [Hz] is the carrier frequency, and c [m/s] is the speed of light) the last term is the free space path loss, that grows quadratically with frequency. Therefore it is commonly assumed that path loss increases dramatically by moving up to higher frequencies, but we have to consider that the entire Friis link budget (1.1) decreases only when the antennas gain is assumed to be constant over frequency.

$$P_r = P_t + G_t + G_r + 20\log_{10}\left(\frac{c}{4\pi r f_c}\right) \text{ [dBW]} \tag{1.1}$$

The free space path loss is dependent on the carrier frequency, if the size of the antennas is kept constant, which is measured by the wavelength λ. Now as the carrier frequency increases, the size of the antennas got reduced and their effective aperture increases with the factor of $\lambda^2/(4\pi)$, while the free space path loss between a transmitter and a receiver antenna grows with f_c^2. So, if we increase the carrier frequency f_c of a factor 10, it will correspondingly add 20 dB of power loss irrespective of the transmitter-receiver distance. But for increased frequency, if the antenna aperture at one end of the link is kept constant, then the free-space path loss remains unchanged. Additionally, if both the transmitter and receiver antenna apertures are kept constant, then the free space path loss decreases with f_c^2.

Given the same physical aperture size, therefore, transmit and receive antennas at higher frequencies, in fact, send and receive more energy through narrower directed beams. To confirm this, in [19] a patch antenna at 3 GHz and an array antenna at 30 GHz of the same physical size were designed and placed within an anechoic chamber at each communication ends. As expected, they measured the same amount of propagation loss regardless of the operating frequency. In addition, when array antennas are used at both transmitting and receiving ends at 30 GHz, the measured received power is 20 dB higher than that of the 3 GHz patch antenna case.

- **Atmospheric absorption**: The propagation characteristics of mmWave communication are different over such huge frequency band, and there are various issues regarding rain attenuation and atmospheric absorption [18]. The resonances of oxygen and other gasses in air cause certain bands to suffer from signal absorption in the atmosphere. As we can see in Fig. 1.4, the bands of 183 GHz, 325 GHz, 380 GHz suffer much greater attenuation over distance due to the molecular resonances of components of the atmosphere, beyond the natural Friis free space loss. We notice also that our band of interest (26 GHz to 30 GHz) is placed near a local minimum of the absorption diagram, so it has favourable condition with respect to other frequencies.

  Rain, hail and snow cause substantial attenuation at frequencies above 10 GHz and then flattens out at 100 GHz to 500 GHz, as Fig. 1.5 illustrates. For all mmWave frequencies, rain or snow attenuation may be overcame with additional antenna gain or transmit power. Also, the size and orientation of rain drops and clouds may determine the particular amount of attenuation on wireless links such that satellites or drones could undergo more localized and perhaps less rain attenuation than terrestrial links at mmWave frequencies. However, it is important to remember that small cell sizes in urban environments will be on the order of 200 m and less, therefore it becomes clear that mmWave communication can overcome these issues. In our band of interest absorption is not critical, indeed atmospheric absorption does not create

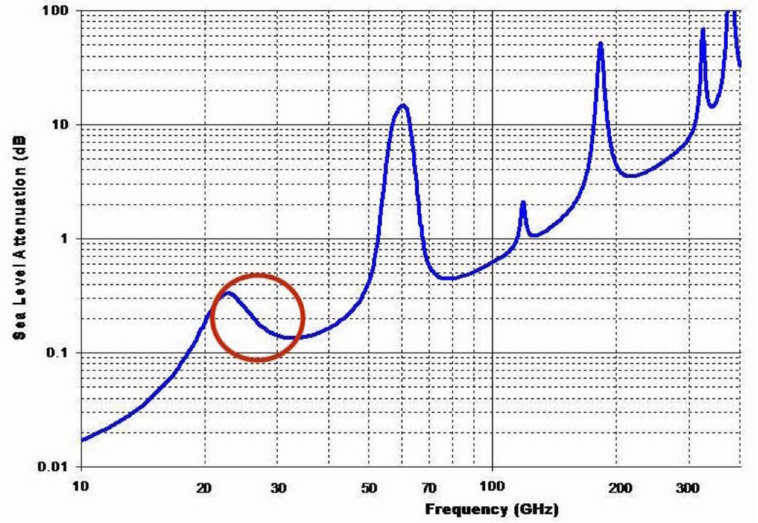

Fig. 1.4: Atmospheric and molecular absorption [dB/km] at mmWave frequencies, with highlighted band of interest, from [20]

significant additional path loss, and only 7 dB/km of attenuation is expected due to heavy rainfall rates of 25 mm/hr at 28 GHz, which results to be 1.4 dB of attenuation over 200 m [18].

- **LOS and NLOS propagation**: The relatively short wavelengths in mmWave bands impose challenges such as greater signal diffusion and difficulty in diffracting around obstacles, that lead to a higher sensibility to blockages. Non Line Of Sight (NLOS) transmissions in mmWave channels suffer from significant attenuation and shortage of multipaths. Therefore, mmWave systems rely mostly on Line Of Sight (LOS) transmissions to achieve the high data rate. The obstacles and moving people can easily block the LOS transmission, and greatly reduce the transmission data rate. MmWave signals have difficulties on penetrating through solid building materials, for example, brick can attenuate signals by as much as 40 - 80 dB and the human body itself can result in a 20 - 35 dB loss [21]. Measurements at 28 GHz [18] showed that outdoor tinted glass and brick pillars had penetration losses of 40.1 and 28.3 dB, respectively, but indoor clear glass and drywall only had 3.6 and 6.8 dB of loss. Has to be considered also foliage attenuation, that increases with the frequency and with the foliage depth. Such high attenuation makes mmWave connection unavailable sometimes in environment with dense high-rise buildings: LOS propagation will predominate, therefore attention must be kept in developing high directivity and user tracking antenna, and in deploying small cell network. We can consider that mmWave signals will be mostly confined to only outdoor or indoor environment [10], because very little signal penetrate indoor through glass doors, open doors and windows ,and viceversa. The indoor - outdoor isolation emphasizes the need for different nodes to serve different

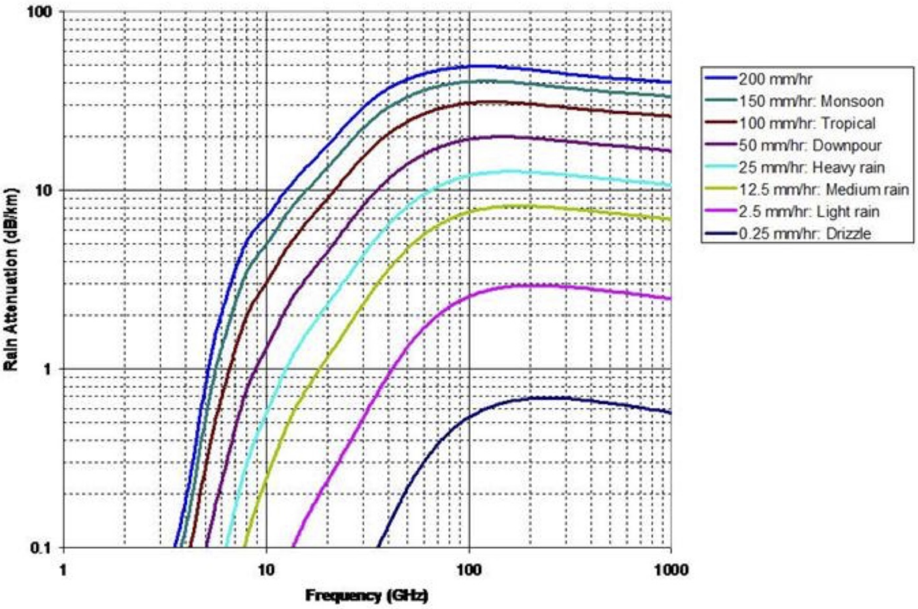

Fig. 1.5: Rainfall attenuation [dB/km] at microwave and mmWave frequencies, from [20]

coverage sites, however, this characteristic also helps in confining the energy in the intended area, facilitating frequency reuse.

- **Scattering and Channel modelling**: If there's no LOS path between the transmitter and the receiver, the signal may still reach the destination thanks to reflection from objects in the surrounding environment or via diffraction. mmWave signals exhibit low diffraction characteristic, but are more subjected to shadowing and reflection. Moreover, shorter wavelengths cause the reflecting material to appear relatively rougher, which results also in greater diffusion of the signal and less specular reflection. Diffuse scattering from rough surfaces may introduce large signal variations over very short travel distances (just a few centimeters), such rapid variations of the channel must be anticipated with the design of channel state feedback algorithms, link adaptation schemes, and beamforming/tracking algorithms. Measurement of diffuse scattering at 60 GHz on several rough and smooth wall surfaces, demonstrated large signal level variations in the first order specular and in the nonspecular scattered components (with fade depths of up to 20 dB) as a user moved by a few centimeters [22]. Measurements at 10, 20, and 26 GHz demonstrate that diffraction loss can be predicted using well-known models as a mobile moves around a corner using directional antennas, and human body blockage causes more than 40 dB of fading [22].

For all these reasons, accurate propagation models are vital for the design of new mmWave signalling protocols. Channel models are required for simulating propagation in a reproducible way, and are used to accurately design and compare radio air interfaces and system deployment. In [23], the large scale fading $F(d)$ is modelled as follows:

$$F(d) = PL(d_0) + 10n\log_{10}\frac{d}{d_0} - S_\sigma\,[\mathrm{dB}] \tag{1.2}$$

where $PL(d_0)$ is the path loss at reference distance d_0, d is the distance between Tx and Rx, n is the path loss exponent, S_σ is the shadowing loss with σ its standard deviation. Researchers found statistical parameters of the path loss model obtained in a corridor, a LOS hall, and a NLOS hall. They observed that the n in the LOS hall is 2.17, while in the NLOS hall is 3.01.

The channel measurement in [18] conducted at 28 GHz in urban propagation in New York City, showed a average LOS path loss exponent of 2.55, and a average NLOS path loss exponent of 5.76.

The 3GPP [24], attempts to provide channel model from 0.5 GHz - 100 GHz: 3GPP documents are a continual work in progress and serve as the international industry standard for 5G cellular. For realizing the propagation channel, distance dependent path loss and shadow fading are considered and assumed that the channel is experiencing Rayleigh fading. As presented in [22], where many models are reported, one of the 3GPP path loss equation is, in the LOS case:

$$PL = 32.4 + 10n\log_{10}(d) + 20\log_{10}(f_c)\,[\mathrm{dB}] \tag{1.3}$$

with n to be chosen between 2 and 4.1 varying with the distance d and depending also by other parameters like antenna heights. The distribution of the shadow fading is log-normal, and the standard deviation for LOS is $\sigma_{SF} = 4.0$ dB.

In the NLOS case we have:

$$PL = 22.4 + 10n\log_{10}(d) + 21.3\log_{10}(f_c) - 0.3\,(h_{UE} - 1.5)\;[\mathrm{dB}] \tag{1.4}$$

with a fixed $n = 3.67$ and h_{UE} is the height of the UE. The shadow fading standard deviation for NLOS is $\sigma_{SF} = 7.82$ dB.

Despite all the challenges listed above, the use of mmWave is justified by the major advantages already explained. To enable this possible benefits, advanced antenna systems have to be developed. The BS and UE antennas have to overcome the characteristic propagation problem, to provide reliable and high-speed communication links. High gain system and antennas capable of producing a narrow beam that can be steered and ideally track the user are the main desirable solution. In particular, adaptive antenna arrays are essential for mmWave communications to compensate the intrinsic path loss and the one caused by blockage. In the next section I will present some existing solution for 5G mmWave antennas.

1.3 Example of mmWave Antennas

Millimeter wave antennas have enjoyed an extended history of development, since the early studies on mmWave propagation characteristic by J.C. Bose in the beginning of 20th century: he's believed to be the first researcher to conduct quantitative measurements down to 5 mm wavelength [25]. Researches and development of mmWave communication system has then continue through decades, mostly pushed forward by studies conducted in military field, at the Bell Laboratories, then for radar application, and recently for automotive industries. In the last 10 years, the scientific literature has seen a major increase of researches on mmWave antennas and RFIC (Radio Frequency Integrated Circuit), clearly driven by the incoming 5G system. In this section we will have a look at some recent progress in this field.

Recently, many TLC operators have tested the possible technologies (e.g., Docomo, KT, AT&T, TIM, Verizon) toghether with leading equipment manufacturers (Huawei, Ericsson, Nokia, Samsung) indicating that the theoretical potential is realizable in real world deployments [26]. High gain antennas with directional beam have been developed, which greatly enhances the Signal to Interference plus Noise Ratio (SINR), mitigates Doppler effect, and improves the data security, and have been widely used in long range mmWave point-to-point communications with a LOS link. In addition, for NLOS communications, the single directional beam can be steered either electronically or mechanically (beamsteering) in order to establish a reliable link. Alternatively, the Multi-Beam Antenna (MBA) [27], which are capable of generating a number of concurrent but independent directive beams with a high gain value to cover a predefined angular range, provide a solution to overcome restrictions of directive beam antennas.

Beamsteering technique and MBA serve as the key hardware technologies for enabling massive MIMO, which makes a clear break from the conventional MIMO technology through utilizing a very large number of service antennas that operate fully coherently and adaptively.

Phased array is one of the most used technique for beamforming antenna: it denotes a digital or analogical controlled array of $M \times N$ antennas which creates a beam steered to point in different directions, thanks to phase shifting applied to single antennas. It is usually composed of printed patch antennas, printed dipoles, Yagi-Uda or planar inverted-F antennas. At mmWave, these antennas are often built on top of thick substrates with high

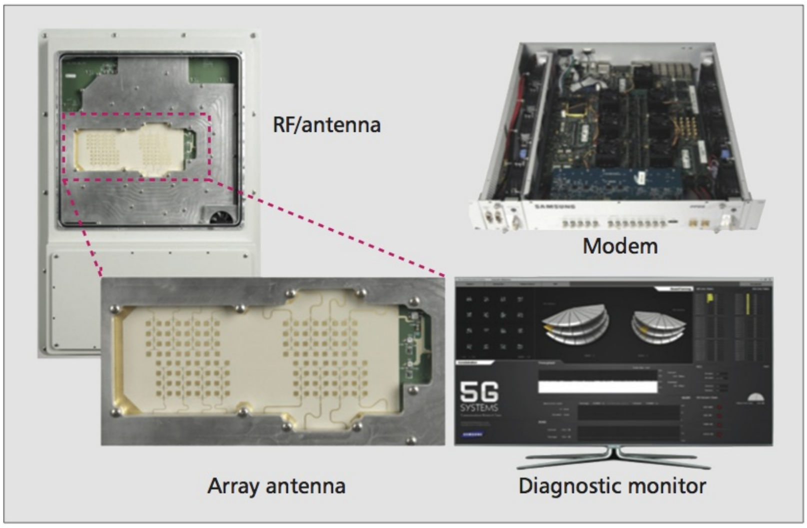

Fig. 1.6: Configuration of the mmWave module and antenna array, from [19]

permittivity, and serious limitations are often associated with printed antennas, like their low power-handling capability, low efficiency, and very narrow achievable bandwidths, although there are many techniques that have been thoroughly investigated that yield better performances.

In [19], a uniform planar array (UPA) of 32 antenna elements working at $f_c = 27.925$ GHz is prototyped and tested, in R&D Center, Samsung Electronics. It’s arranged in the form of 8 horizontal and 4 vertical patch elements, confined within an area of 60 x 30 mm. The array antenna is connected to the RF unit, which contains a set of phase shifters, mixers, and related RF circuitry that control the radiating system. This was one of the first test in which a 5G enabling antenna technology was completely developed and tested in a urban environment, and gave useful information to following researches. The antenna system (Fig. 1.6) achieve a horizontal beam scanning range of ± 30°, with a Full Width at Half Maximum (FWHM) of the beam at the antenna boresight (the direction of maximum gain) of approximately 10° horizontally and 20° vertically, with an overall beamforming gain of 18 dBi. A set of beam patterns is predefined to reduce the feedback overhead required for the adaptive beamforming, and the maximum transmit power was set to 31 dBm, corresponding to 1.26 W. In the transmission test, using a 500 MHz bandwidth, an aggregated peak data rate of 1.056 Gb/s was achieved in the laboratory with negligible packet error, using two channels at the base station supporting two mobile stations with 528 Mb/s each. In outdoor range test with LOS path, the communication range with negligible errors was verified up to 1.7 km, and also satisfactory communications links were tested in NLOS condition at distances of 200 m.

The researchers in [28] proved the concept of mmWave HetNets (Heterogeneous Networks) by developing a demonstration system, in particular a fast mmWave access at 60 GHz between a small cell BS and a smartphone, achieving 6.1 Gb/s. A 60 GHz wireless access module is developed based on their previously developed CMOS RF module, together with a mmWave *GATE* (Gigabit Access Transponder Equipment) antenna with 32 x 32 massive antenna elements connected to the mmWave BS to provide specially shaped communication area. This technology will be probably available in 2020 Tokyo Olympic Games, and can be installed in public areas such as in corridors and escalators, in stations and shopping malls and in other crowded locations for the purpose of a mmWave wireless access.

Giving an insigth into available commercial product, surely interesting is Anokiwave's 5G Active Antenna Innovator's Kit [29]: the manufacturer developed a early all-in-one solution for 5G fixed wireless access, using planar antenna technology. It works at 28 GHz, with an array of 64 antenna element, and achieved Gb/s data rates in OTA trials. The electronic 2D beam steering is achieved using analog RF beamforming, with independent phase and gain control in both Tx and Rx operating modes, allowing a beam scanning range of ±60°.

Recently, at the International Solid-State Circuits Conference (ISSCC), IBM and Ericsson announced [30] a Silicon mmWave phased array antenna module operating at 28 GHz. The module [31] consists of four MMICs (Monolithic Microwave Integrated Circuits) and 64 dual-polarized antennas, and measures approximately 7.1 x 7.1 cm. The organic-based multi-layered phased array antenna module is able to form two beams simultaneously, doubling the number of users that can be served, with a beamsteering resolution of less than 1.4°. The conducted tests has confirmed optimum performances: a 35 dBi gain and a steering range of ±40°, with a 3 GHz bandwidth. In Fig. 1.7 we can observe the schematic illustration of antenna-in-package assembly system.

Apart from phased array-like solution, other structures have been investigated. In [32] for example, two linearly-polarized transmit-arrays working at 60 GHz are presented: they are related to lens antenna type, and they're based on a similar concepts as for reflect-arrays, except that they operate in a transmission mode rather than reflection. The paper report two types of unit cell: a Patch-via hole-Patch (PVP) and Slot-Resonator-Slot unit-cell (SRS). The PVP consists of two identical patch antennas connected by a via hole in the substrate and separated by a ground plane, while the SRS is composed by two identical slot antennas coupled by a L-shaped strip-line placed in the intermediate layer. A 10 dBi linearly-polarized

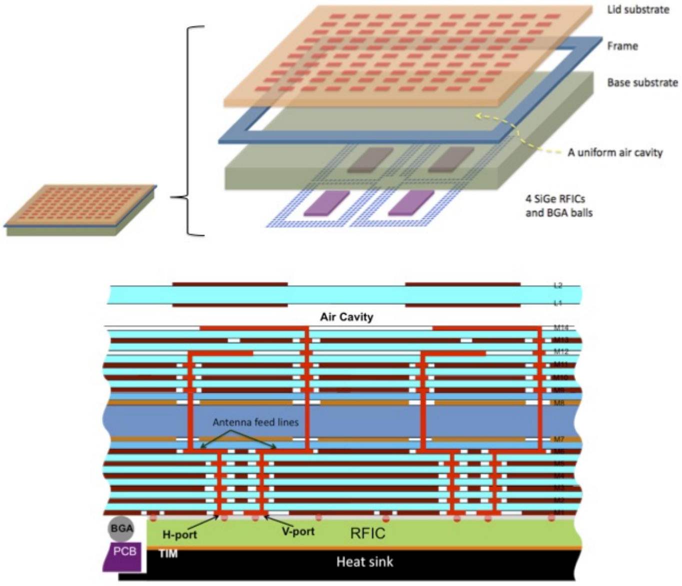

Fig. 1.7: Schematic illustration of antenna-in-package assembly system and substrate layer, from [31]

horn antenna is placed in the focal source and used as feed, 25 mm in front the array of unit cells. The system can achieve a specific beam shape by applying a 180° specific phase-shift distribution to the array unit cell. It is composed by 20 × 20 cells fed by the horn antenna. The simulated test showed a realized total gain of 22.76 dBi (PVP cell) and 22.21 dBi (SRS cell), with a 3-dB gain bandwidth of 11.3 % and 8.7 %, respectively. Interestingly, with respect to reflect arrays, this type of structure presents several advantages such as reduction of blockage effects due to the primary feed, easiness of integration and mounting onto various platforms, although its design is relatively more complex.

Differently, in [33], researchers present several gap waveguide planar array antennas for mmWave fixed beam point to point communication systems at 60 GHz. Waveguide slot array antennas are expected to provide high efficiency and high gain at mmWave frequency range due to lower losses in antenna feed networks. The paper investigate different design, using groove gap waveguide, ridge gap waveguide and inverted microstrip gap waveguide technology. The designed antenna array have 16 × 16 radiating slot elements and simulated tests showed over 15 % relative bandwidth from 57 - 66 GHz frequency range with simulated directivity of 33.3 dBi. The main feature of these gap waveguide antennas is the flexibility in mechanical assembly which will allow low cost manufacturing techniques and will lower the overall cost of the mmWave modules, maintaining good overall performances.

In mmWave research field many other structure and type of antenna are present and are currently being investigated by manufacturers and research teams. Among various kind of radiating element, interesting innovation are being developed in the metamaterial Leaky Wave Antenna (LWA) field. This particular type of antenna presents some advantages like a simpler feeding circuitry, due to absence of phase shifter, and a more compact packaging, maintaining good beamsteering performance. In chapter 3 I will explore LWA theory and application, reporting some example of ongoing researches.

Chapter 2

Substrate Integrated Waveguide and Electromagnetic Metamaterials

Substrate Integrated Waveguide (SIW) technology represents an emerging and very promising candidate for the development of circuits and components operating in the microwave and mmWave range. SIW permits the development of classical Rectangular Waveguide (RWG) components in planar form, together with printed circuitry, active devices and antennas, reaching a compromise between the interoperability of planar components and the good guiding performances of RWG. Another advantage is the easy implementation of a transition between SIW and microstrip line, that can then be interconnected with standard components. This structure is versatile, indeed it gives the possibility of integrating all the elements on the same substrate, including passive components, active elements and even antennas. Moreover, it is possible to mount one or more chip-sets on the same substrate.

Furthermore, SIW can be easily modified with slots on its metal surface and with active components such as varactor diodes, to create parasitic capacitances and inductances, and then altering the constitutive parameters of the Transmission Line (TL). In this way we obtain a Composite Right-Left Handed (CRLH) structure, or Metamaterial (MTM) TL, that can be properly tuned to modify the propagation characteristics of electromagnetic signal, e.g. introducing phase delay, obtaining Zero Order Resonance (ZOR), and switching from guided wave to radiated wave behaviour.

In this chapter I will illustrate the main characteristics of Substrate Integrated Waveguide, its components and functioning, then I will explain how to dimension it based on working frequency and how SIW can be interconnected to microstrip line through a transition. In the second part a brief resume of electromagnetic metamaterial and CRLH theory is presented, pointing out their main features like backward wave propagation, Left Handed frequency range, and dispersion diagram, concluding with some examples.

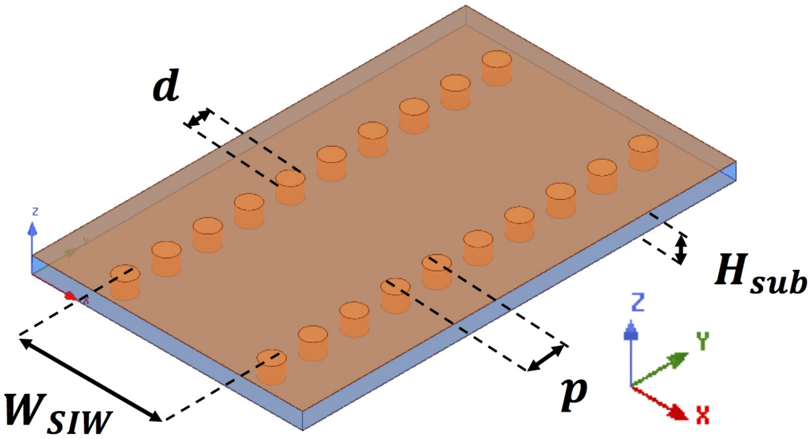

Fig. 2.1: 3D model of an SIW with its main design parameters

2.1 Substrate Integrated Waveguide

2.1.1 Structure and Dimensioning

Researchers have been studying SIW for the past decades, since the early studies on this structure, called *post-wall waveguide* in the very first paper on this subject [34], and also, later, *laminated waveguide* [35]. Since the introduction of SIWs, various SIW based components, interconnects, circuits and antennas have been developed and their advantages are justified in comparison to their milled waveguide or transmission line based counterpart.

Substrate integrated waveguides are fabricated by using two rows of conducting cylinders or slots embedded in a dielectric substrate that connects two parallel metal plates. It is essentially an RWG-like structure, where the conductor side-walls are replaced by two rows of metallized vias, and therefore it presents many affinities to a dielectric filled rectangular waveguide. The transmission line formed by the SIW not only have the favourable physical characteristics of planar printed transmission lines, but also possess the excellent guiding performance of bulky RWG. By adopting the Printed Circuit Board (PCB) fabrication method, SIW scales down the RWG height to the thickness of PCB substrate, that can be considered as the inner-filled dielectric of a waveguide. Indeed one of the main advantage of SIW technology is the possibility of its easy implementation using common PCB fabrication process. In Fig. 2.1 we can observe a 3D model of an SIW, designed with Ansys HFSS [36].

The fundamental design parameters are: W_{SIW}, the width of the SIW (center-to-center distance between the rows of vias), related to a_{RWG}, the width of the equivalent RWG; p, the via holes pitch, i.e. longitudinal center-to-center distance between the pins; d, the pin diameter; H_{sub}, the dielectric height, usually fixed by standard substrate dimensions.

The upper and bottom copper sheets and via holes, replacing the RWG conductive walls, form a current loop in the sectional view (xz plane), which is similar to the cross-section case of traditional solid metal waveguide. The surface current on pin cylinders is limited to vertical direction ($\mathbf{z}$): the side wall current clearly cannot flow longitudinally across the regular intervals ($\mathbf{y}$ direction). Therefore, the propagation in an SIW can only perform TE_{m0} (Transverse Electric) modes of traditional RWG, in which the E-field is perpendicular to the propagation direction $\mathbf{y}$ and will not change across the z-axis. Thus, the first propagation mode of SIW is the TE_{10} mode, and as in RWG, SIW transmission line has a specific allowable lowest transmission frequency, the cutoff frequency f_{cut}.

The wavelength λ_{cut} of the cutoff frequency is in proportion to the width of the SIW. For a standard RWG with a_{RWG} and b_{RWG} lateral dimensions, filled with a dielectric of relative dielectric constant ε_r, the cutoff frequency of mode (m, n) is [37]:

$$f_{m,n} = \frac{c}{2\sqrt{\varepsilon_r}} \sqrt{\left(\frac{m}{a_{RWG}}\right)^2 + \left(\frac{n}{b_{RWG}}\right)^2} \, ; \tag{2.1}$$

in our case, we consider $m = 1$ and $n = 0$, obtaining

$$f_{1,0} = f_{cut} = \frac{c}{2\, a_{RWG} \sqrt{\varepsilon_r}} \, . \tag{2.2}$$

Therefore, the first step to design an SIW is to dimension the equivalent rectangular waveguide, choosing the dielectric material and f_{cut}, and obtaining a_{RWG}:

$$a_{RWG} = \frac{c}{2\, f_{cut} \sqrt{\varepsilon_r}} \, . \tag{2.3}$$

Various studies have investigated the relation between RWG and SIW dimensions [38–40]. In particular, in [40], we find a closed form to obtain W_{SIW} from a_{RWG} (provided that the pitch p and the ratio d/W_{SIW} are sufficiently small):

$$W_{SIW} = 0.5 \left[a_{RWG} + \sqrt{(a_{RWG} + 0.54d)^2 - 0.4d^2} \right] + 0.27d \, . \tag{2.4}$$

This formula can be used to get an approximate value of W_{SIW}, to set a frequency range in which the waveguide can operate: we will see in the design phase (Chap. 4) that the numeric result is purely indicative and will be increased in order to lower f_{cut} and putting our working frequency f in a range far enough from the cutoff region.

Indeed, also a simpler equation is sufficient to have a good approximation of SIW width, given a_{RWG}, d and p [38, 41]:

$$W_{SIW} = a_{RWG} + \frac{d^2}{0.95\,p}\,. \tag{2.5}$$

We observe that Eq. (2.4) and (2.5) depend on p and d. There are not closed form expressions for their values, but we can find some constraints to guarantee good propagation and low losses [40]:

$$\begin{aligned} d &\leq \frac{\lambda_g}{5}\,, \\ p &\leq 2d\,, \end{aligned} \tag{2.6}$$

where

$$\lambda_g = \frac{\lambda_0}{\sqrt{1-\left(\frac{f_{cut}}{f}\right)^2}} \tag{2.7}$$

λ_g is the guided wavelength, $\lambda_0 = c/f$ is the free space wavelength. To reduce manufacturing costs and problems related to milling precision, p and d should be selected as large as possible, so we will use their upper limits.

Similarly to RWG, SIW structures are limited in compactness and bandwidth. The width W_{SIW} of the SIW determines the cutoff frequency f_c of the fundamental mode. The operation bandwidth, corresponding to the monomode bandwidth of the waveguide, is then theoretically limited to one octave: from the cutoff frequency f_c of the TE_{10} mode to cutoff frequency $f_{2,0} = 2f_c$ of the TE_{20} mode. Therefore, we have a useful frequency range of width f_c, that will result in a large enough spectrum of approximately 20 GHz, choosing f_c in these values.

Dimensions and materials chosen for the waveguide are also related to loss mechanisms of SIW [42]. Loss minimization is particularly critical when operating at mmWave frequencies. There are three main sources of losses: conductor losses (due to the finite conductivity of metal walls), dielectric losses (due to the lossy dielectric material) and radiation losses (due to the energy leakage through the gaps).

Propagation occurs in an RWG-like manner, so conductor losses are not dominant, and can be significantly reduced by increasing the substrate thickness H_{sub}. Conversely, dielectric losses depend only on the dielectric material and not on the geometry of the SIW structure, therefore they can be reduced only by using a better dielectric substrate. Attenuation because of the dielectric losses is related to $\tan\delta$ of the material. Generally speaking, the contribution of dielectric losses is dominant at mmWave frequencies, when using typical substrate thickness and commercial dielectric materials [43] . Attention must be paid in choosing the substrate material, since at mmWave it is necessary to reach a compromise between costs of manufacturing and dielectric losses. Finally, radiation losses can be kept reasonably small if $p/d < 2.5$ [38], usually setting $p = 2d$. In fact, if the pitch p is small and the diameter d of the metal vias is large, the gap between the metal vias is small, thus approaching the condition of continuous metal wall and minimising the radiation leakage. In conclusion, the goal is to choose SIW dimensions so that we can get a feasible structure (considering practical application) and at the same time maintain small losses.

The choice of this type of waveguide as the base of our antenna system is justified by its good behaviour at high frequencies. The SIW technology has already experienced a rapid development over more than one decade, that allowed the demonstration and applications of innovative systems in particular at mmWave frequencies, covering a very broad frequency range from sub-GHz to sub-THz. SIW has been found well suited for the mmWave range, since the transmission line technology is critical for developing high-frequency electromagnetic hardware. The transmission line should allow high-density integration and mass-production scheme at low cost. As clock frequencies and circuit densities continue to increase, closely spaced microstrip and stripline interconnects will no longer be viable options for interconnection of system modules, due to their open structure and susceptibility to crosstalk and electromagnetic interference (EMI). These factors will induce employing the SIW technology in future ultra-high frequency and broadband applications and highly integrated systems. It has been shown [42] that SIW interconnects, due to their enclosed structure, efficiently confine electromagnetic fields, and can be exploited to reduce crosstalk. Having a shielded signaling medium is critical in reducing unwanted noise and EMI in dense circuit layouts. An easy-to-handle and low cost hybrid design strategy is of critical importance for the development of mmWave ICs and systems.

2.1.2 Microstrip to SIW Transition

The transition between planar transmission line and SIW represents another important element related to SIW structures. As we said, one of the main advantage of adopting this waveguide lies in the possibility of an easy integration with planar components, especially microstrip line, since it is one of the most common planar lines used in PCB. Several broadband transitions between microstrip or coplanar waveguide and SIW have been developed [40, 42, 44, 45]. In particular, microstrip to SIW transition can be easily based on a simple tapered section [45], provided that the microstrip and the SIW structure are integrated on the same substrate, that is our case. To adapt microstrip to SIW, parametric simulations have been conducted, for example in [46], to offer a guideline for fast design.

Starting from the working frequency f and the chosen substrate with dielectric constant ε_r, the first step is to dimension the microstrip line, imposing a standard characteristic impedance Z_0 of 50 Ω. Using the following formulas [37] we can find the ratio W_0/H_{sub} between the width W_0 of the microstrip line and the substrate height H_{sub}:

$$\frac{W_0}{H_{sub}} = \begin{cases} \frac{8e^A}{e^{2A}-2} & \text{for } \frac{W_0}{H_{sub}} < 2 \\ \\ \frac{2}{\pi}\left[B-1-\ln(2B-1)+\frac{\varepsilon_r-1}{2\varepsilon_r}\left(\ln(B-1)+0.39-\frac{0.61}{\varepsilon_r}\right)\right] & \text{for } \frac{W_0}{H_{sub}} < 2 \end{cases} \tag{2.8}$$

where

$$\begin{aligned} A &= \frac{Z_0}{60}\sqrt{\frac{\varepsilon_r+1}{2}} + \frac{\varepsilon_r-1}{\varepsilon_r+1}\left(0.23+\frac{0.11}{\varepsilon_r}\right), \\ B &= \frac{377\pi}{2Z_0\sqrt{\varepsilon_r}}. \end{aligned} \tag{2.9}$$

Therefore, once fixed ε_r and H_{sub} by standard substrate fabrication characteristics, and Z_0 to a standard 50 Ω, we get the width W_0.

Microstrip to SIW transition is essentially a tapered microstrip line connecting the microstrip section of width W_0 to the waveguide of width W_{SIW}, as shown in Fig. 2.2. Following the formulas retrieved in [46], we obtain an indication on the two main design parameter: length L_{tap} and width W_{tap} of the tapered section connecting the microstrip line to the upper metal plate of the SIW structure:

$$\begin{aligned} &\frac{W_{tap}}{W_{SIW}} \simeq 0.4, \\ &\frac{\lambda_{g,micro}}{2} < L_{tap} < \lambda_{g,micro}, \end{aligned} \tag{2.10}$$

where $\lambda_{g,micro} = \lambda_0/\sqrt{\varepsilon_r}$ is the wavelength of the propagating quasi-TEM (transverse electromagnetic) mode in the microstrip line. The design of this type of transition will be mostly realized by optimizing the dimensions obtained with (2.10) while monitoring the fullwave

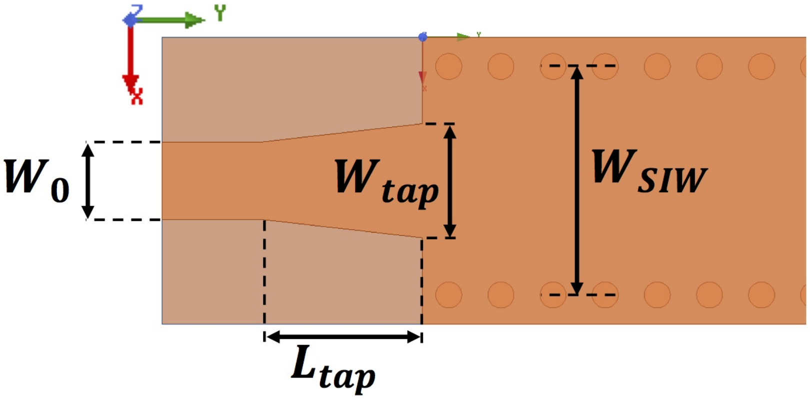

Fig. 2.2: Microstrip to SIW transition and its main parameters

simulation results, checking the main indicative scattering parameters like S_{11} and S_{21}, to assure that the propagation occurs without major reflection due to the transition points.

This transition is a trade off between simplicity and good performance, since it gives the opportunity to adopt a standard feeding network solution with microstrip line. The taper is used to transform the quasi-TEM mode of the microstripline into the TE_{10} mode in the SIW. It provides a gradual transformation of the characteristic impedance Z_0 of microstrip line to the impedance of SIW line.

The characteristic impedance in a transmission line supporting a TEM wave can be defined in one of the three following ways: Z_{PV}, Z_{PI}, Z_{VI}, depending on the parameters used for the ratio calculation (Voltage V, Current I and power P). In a rectangular waveguide, and similarly in an SIW, however, the choice of voltage and current is not unique and these definitions do not produce the same results, therefore the choice of which definition is more suitable depends on the application. In our case, I noticed that Z_{PI} (Eq. 2.11) provided better results according to fullwave simulation. Z_{PI} can be approximately calculated with [43]:

$$Z_{PI} = Z_{TE} \frac{H_{sub}\, \pi^2}{8\, a_{RWG}}, \tag{2.11}$$

where Z_{TE} is the wave impedance of TE mode and η is the intrinsic impedance of the medium:

$$Z_{TE} = \frac{\eta}{\sqrt{1 - \left(\frac{f_{cut}}{f}\right)^2}}, \tag{2.12}$$

$$\eta = \sqrt{\frac{\mu}{\varepsilon}} \simeq \frac{120\,\pi}{\sqrt{\varepsilon_r}}. \tag{2.13}$$

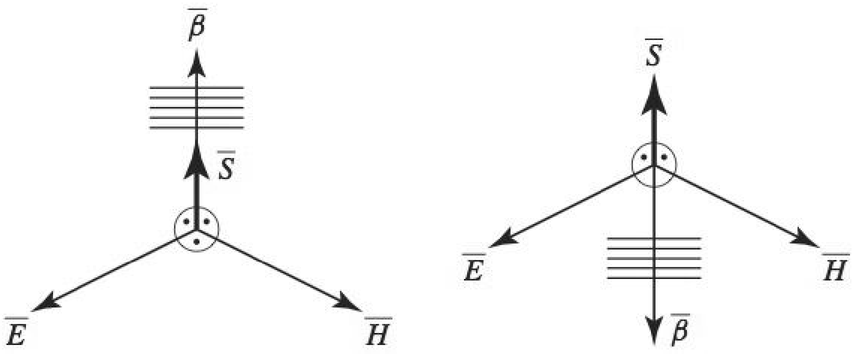

Fig. 2.3: Electric field **E**, magnetic field **H**, phase constant vector $\boldsymbol{\beta}$ triad and Poynting vector **S** for an electromagnetic wave, in a RH medium and in a LH medium, from [50]

2.2 Electromagnetic Metamaterials

The rise of a new class of engineered electromagnetic materials, known as Negative Refractive Index (NRI) Metamaterial (MTM), realized using either split-ring resonators and wires [47] or reactively loaded Transmission Line (TL) [48], has generated great interest within the scientific community, for their potential to create devices and components that exhibit new phenomena or improved performance characteristics compared to their conventional counterparts. The term NRI indicates that these materials can have simultaneously negative constitutive parameters (permittivity ε and permeability μ), and therefore a negative refractive index $n = \pm\sqrt{\varepsilon_r \mu_r}$, showing behaviours that are not naturally present, hence the prefix *meta* (ε_r and μ_r are the relative permittivity and permeability). More generally, the parameters can be engineered to have positive, negative, and zero values using dispersion engineering techniques.

In 1968, Veselago was the first to examine media having negative dielectric and magnetic constitutive parameters [49]. In his paper, Veselago called these "substances" Left Handed (LH), to express the fact that the electric field **E**, the magnetic field **H**, and the phase constant vector $\boldsymbol{\beta}$ form a left handed triad, contrary to conventional materials where this triad is Right Handed (RH) (Fig. 2.3).

Afterwards, there has been a considerable amount of researches into metamaterials over the last several years, to expand the range of possible applications, and various researchers have investigated and reported in particular the electromagnetic MTM theoretical bases [48, 50–52].

Materials with such propagation characteristics do not exist in nature, indeed there are three main methods to realize metamaterials structure [51]: i) the resonant approach, based on pairing split ring resonators (SRR) with metal wires to provide an effective negative permeability and negative permittivity, respectively; ii) the evanescent mode approach, using dielectric resonators placed inside a cutoff background; iii) the transmission line approach, based on realizing a LH TL unit cell, which consists of a series capacitance and shunt inductance. Since natural RH effects are unavoidable, a Composite Right-Left Handed (CRLH) TL is a practical realization of a LH TL. Our interest will be focused on this last approach. The CRLH TL can support both forward and backward waves, as well as standing waves with zero propagation constant: these characteristics are the bases for their use in many antenna applications, as leaky-wave antennas, compact resonant antennas, and multiband antennas.

2.2.1 Composite Right-Left Handed Transmission Line

An arbitrary transmission line can be described in terms of an equivalent circuit model. In the lossless case, the model comprises a series inductance L_R, induced by magnetic fields around conductors, and parallel capacitance C_R, resulting from the conductor spacing. This is the case of a classical RH TL. The TL approach towards LH metamaterials is based on realizing a TL that supports a backward wave, i.e. that has a phase velocity v_p which is in the opposite direction of its group velocity v_g. As a result, the refractive index n of such a structure is negative.
A LH TL is composed by a sequence of unit cells, that are represented by a series capacitance C_L and shunt inductance L_L [50]. However, the pure LH TL is not physically possible because, theoretically, the group velocity of the supported wave exceeds the speed of light in vacuum as the operational frequency increases. Moreover, a pure LH structure is not feasible because of the presence of RH parasitic series inductance L_R and shunt capacitance C_R effects, respectively due to current flow along the metallization and to development of voltage gradients between the metal patterns of the trace and the ground plane. The CRLH TL is then a practical realization of a LH TL which includes parasitic RH effects that naturally occur with any physical LH TL implementation. For simplicity, we consider only the lossless case.

The series C_L and shunt L_L elements are responsible for LH propagation, whereas the shunt C_R and series L_R elements cause RH propagation at higher frequencies. Indeed, the LH and RH propagation properties can be tuned to some desired frequency range by controlling the unit cell parameters. In Fig. 2.4 we can observe the equivalent circuit model of lossless RH TL, LH TL, and CRLH TL.

The above considerations about LH and CRLH TL are valid in condition that the structure is *effectively homogeneous*. This means that the average cell size Δz is much smaller than the

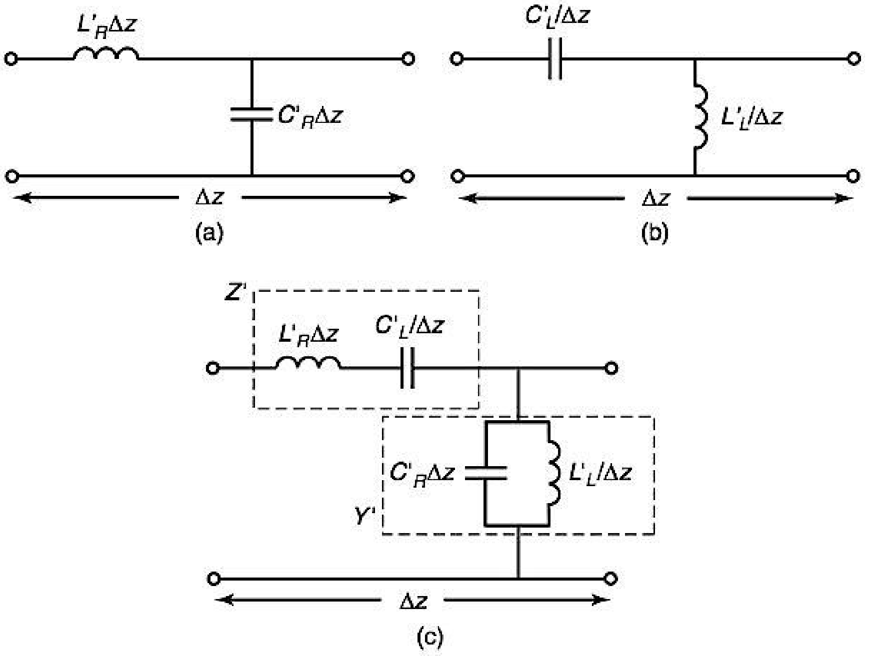

Fig. 2.4: Equivalent circuit model for lossless a) pure RH TL, b) pure LH TL, c) CRLH TL, from [48]

guided wavelength λ_g in the considered structure ($\Delta z \ll \lambda_g$, at least $\Delta z < \lambda_g/4$). If this could be accomplished, a non resonant LH medium would be obtained, and the design would be perfectly realizable.

In our notation, primes are used to represent per-unit-length quantities: C'_R [F/m], L'_R [H/m], C'_L [F·m], L'_L [H·m] defined in a way to keep consistency with impedance, admittance, and propagation constant units of measurement, according to [50]. From the cell parameters we can compute per-unit-length impedance Z' and admittance Y'. Resuming, we have:

- RH series inductance $L_R = L'_R\,\Delta z$ [H] and RH shunt capacitance $C_R = C'_R\,\Delta z$ [F];
- LH series capacitance $C_L = C'_L/\Delta z$ [F] and LH shunt inductance $L_L = L'_L/\Delta z$ [H];
- per-unit-length impedance $Z'(\omega) = j\left(\omega L'_R - \frac{1}{\omega C'_L}\right)$ [Ω/m];
- per-unit-length admittance $Y'(\omega) = j\left(\omega C'_R - \frac{1}{\omega L'_L}\right)$ [S/m];

where we are using the standard notation for angular frequency $\omega = 2\pi f$. Starting from this scheme, following the classical analysis of transmission lines with the generalized telegraphist's equations, propagation characteristics can be derived [50].

The propagation constant of a TL is given by $\gamma(\omega) = \alpha(\omega) + j\beta(\omega) = \sqrt{Z'(\omega)\,Y'(\omega)}$, where α is the attenuation constant and β is the phase constant. The characteristic impedance Z_c is obtained as $Z_c = \sqrt{Z'/Y'}$. We recall that all these quantities are frequency dependent. For an easier notation, we introduce the variables:

$$\begin{aligned}
\omega'_R &= \frac{1}{\sqrt{L'_R C'_R}} \quad [(\mathrm{rad}\cdot\mathrm{m})/\mathrm{s}]\,, \\
\omega'_L &= \frac{1}{\sqrt{L'_L C'_L}} \quad [\mathrm{rad}/(\mathrm{m}\cdot\mathrm{s})]\,, \\
\kappa &= L'_R C'_L + L'_L C'_R \quad [(\mathrm{s}/\mathrm{rad})^2]\,, \\
\omega_{se} &= \frac{1}{\sqrt{L'_R C'_L}} \quad [\mathrm{rad}/\mathrm{s}]\,, \\
\omega_{sh} &= \frac{1}{\sqrt{L'_L C'_R}} \quad [\mathrm{rad}/\mathrm{s}]\,,
\end{aligned} \tag{2.14}$$

where ω_{se} and ω_{sh} are the series and shunt resonance frequencies, respectively. Noticing their units of measurement, coherent with the above cell parameters definition, we underline that ω'_R and ω'_L are not frequencies but only auxiliary variables. Therefore, using this notation, the explicit complex propagation constant for the CRLH TL is:

$$\gamma(\omega) = \alpha(\omega) + j\beta(\omega) = js(\omega)\sqrt{\left(\frac{\omega}{\omega'_R}\right)^2 + \left(\frac{\omega'_L}{\omega}\right)^2 - \kappa\,\omega_L'^2}\,, \tag{2.15}$$

where $s(\omega)$ is the following sign function, that distinguishes between LH and RH range:

$$s(\omega) = \begin{cases} -1 & \text{if} \quad \omega < \min(\omega_{se};\ \omega_{sh}) \quad \text{LH range,} \\ +1 & \text{if} \quad \omega > \max(\omega_{se};\ \omega_{sh}) \quad \text{RH range.} \end{cases} \tag{2.16}$$

The propagation constant γ in (2.15) can be purely real or purely imaginary, depending on whether the radicand is negative or positive, respectively. In the frequency range where γ is purely real, $\min(\omega_{se};\ \omega_{sh}) < \omega < \max(\omega_{se};\ \omega_{sh})$, a stop-band occurs, despite the fact that the line is loss-less. When $\omega < \min(\omega_{se};\ \omega_{sh})$ or $\omega > \max(\omega_{se};\ \omega_{sh})$, we have $\gamma = j\beta$ purely imaginary, and a pass band is present. In the latter case, we distinguish between LH and RH range, frequency bands in which the TL presents different behaviours, and we indicate the propagation constant as β_{LH} and β_{RH}, respectively. We can observe a plot of the CRLH dispersion and attenuation relation (also called dispersion diagram) in Fig 2.5, in comparison with the dispersion curve of the pure RH and pure LH lines.

In the LH range, propagation constant β_{LH} is negative; the phase velocity v_p (slope of the line segment from origin to β curve, Eq. (2.17)) and group velocity v_g (slope of the β curve, Eq. (2.17)) have opposite signs, so they are antiparallel. In contrast, in the RH range, β_{RH} is positive and the phase and group velocities have the same sign.

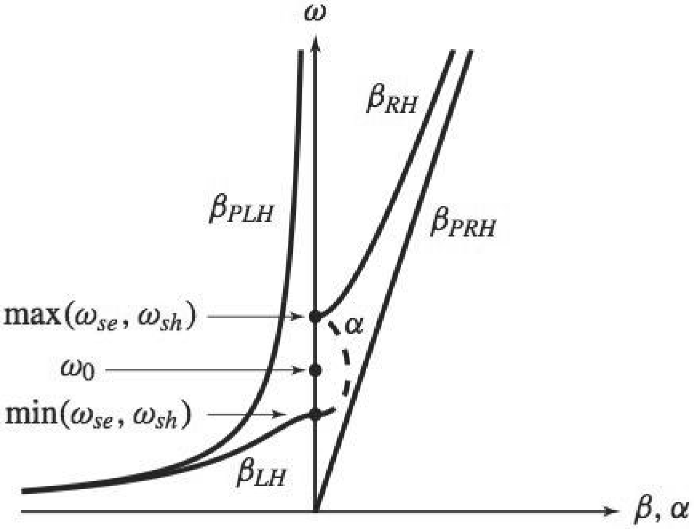

Fig. 2.5: Dispersion/attenuation diagram of a CRLH TL, from Eq. (2.15), in comparison with a pure RH (β_{PRH}) and a pure LH (β_{PLH}) TL, from [50]

Also phase shift $\phi = -\beta L$ along a TL of length L changes trend between RH and LH range. Phase advance ($\phi > 0$) occurs in the LH frequency range, and classical phase delay ($\phi < 0$) occurs in the RH frequency range. We remember here that the phase velocity v_p is the rate at which the phase of the wave propagates in space, and it is associated with the direction of wave vector $\boldsymbol{\beta}$. The group velocity v_g is associated with the direction of power flow, therefore with Poynting vector $\mathbf{S} = \mathbf{E} \times \mathbf{H}^*$. It is then physically possible to have these two velocities with different sings, since phase velocity corresponds to the propagation of a perturbation, and not of energy, therefore v_p can be negative or positive; but v_g has to be of the same sign of direction of power flow (for convention, plus sign).

In the case of a weakly lossy CRLH TL, the expression for Z', Y' and γ change, introducing the loss contributions due to resistance R' and conductance G'. If the losses are not significant, approximations can be made and lead to very similar expressions to that of the lossless case, that is indeed precise enough for our analysis and for this thesis purpose.

$$v_p = \frac{\omega}{\beta}; \qquad v_g = \left(\frac{d\beta}{d\omega}\right)^{-1}. \tag{2.17}$$

2.2.2 Balanced CRLH TL

The stop-band $\min(\omega_{se};\, \omega_{sh}) < \omega < \max(\omega_{se};\, \omega_{sh})$ is a unique characteristic of the CRLH TL, which is not present in the pure RH or the pure LH cases. This gap is due to the different series and shunt resonances ω_{se} and ω_{sh}: when this occurs, the CRLH TL is said to be unbalanced. When these two frequencies are equal, the line is called *balanced* and the

CRLH gap closes up. To obtain $\omega_{se} = \omega_{sh}$, from Eq. (2.14), we need:

$$L'_R C'_L = L'_L C'_R \,. \tag{2.18}$$

It is generally preferable to have a balanced CRLH TL, acting on lumped parameters or TL structure, since it has a number of advantages over the unbalanced CRLH TL. Indeed, its equivalent model and the analysis is simpler than the case of the general unbalanced model.

Firstly, from Eq. (2.15), the propagation constant β results simply expressed as the sum of the propagation constants of a linear and positive pure RH TL and of a negative and hyperbolic pure LH TL:

$$\beta = \beta^{PRH} + \beta^{PLH} = \frac{\omega}{\omega'_R} - \frac{\omega'_L}{\omega} = \omega\sqrt{L'_R C'_R} - \frac{1}{\omega\sqrt{L'_L C'_L}} \,. \tag{2.19}$$

Since the expressions $\sqrt{L'_R C'_R}$ and $\sqrt{L'_L C'_L}$ are measured respectively in (m·rad/s)$^{-1}$ and rad/(m·s), the above expression results in the conventional unity of measurement 1/m. Indeed, we can also highlight its dependence on the unit cell length Δz, obtaining:

$$\beta(\omega) = \frac{1}{\Delta z}\left(\omega\sqrt{L_R C_R} - \frac{1}{\omega\sqrt{L_L C_L}}\right) \,. \tag{2.20}$$

The root of expression (2.19) is the frequency ω_0:

$$\omega_0 = \sqrt{\omega'_R \omega'_L} = \frac{1}{\sqrt[4]{L'_R\, C'_R\, L'_L\, C'_L}} = \frac{1}{\sqrt{L'_R\, C'_L}} = \frac{1}{\sqrt{L'_L\, C'_R}} \,, \tag{2.21}$$

noting that in this case we have $\omega_0 = \omega_{sh} = \omega_{se}$. This quantity is called transition frequency, and we have $\beta(\omega_0) = 0$. It is the point of gap-less transition between the LH ($\omega < \omega_0$) and RH ($\omega > \omega_0$) ranges, if the line is balanced. In Fig. 2.6 we can observe the dispersion diagram for a balanced CRLH TL, noting the transition frequency ω_0 and the absence of the stop-band.

The characteristic impedance becomes frequency independent, therefore the balanced condition allows matching over a theoretical infinite bandwidth:

$$Z_c = \sqrt{\frac{L'_L}{C'_L}} = \sqrt{\frac{L'_R}{C'_R}} \,. \tag{2.22}$$

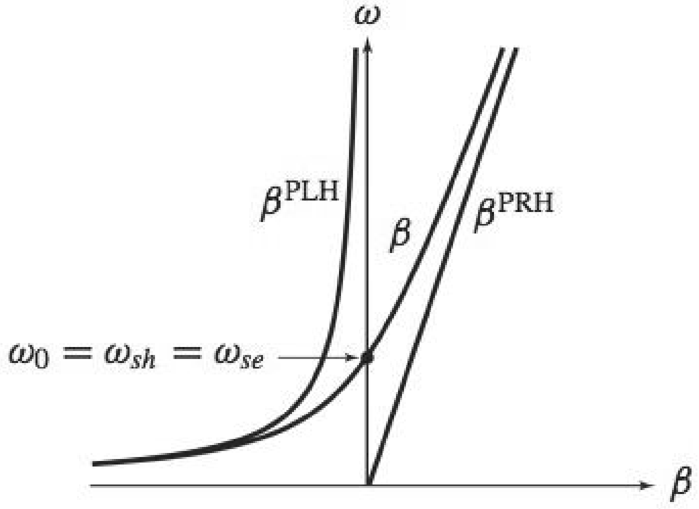

Fig. 2.6: Dispersion diagram of a balanced CRLH TL, from Eq. (2.19), in comparison with a pure RH (β^{PRH}) and a pure LH (β^{PLH}) TL, from [50]

The refractive index can be derived and assumes the expression:

$$n = \frac{c\beta}{\omega} = c\left(\frac{1}{\omega'_R} - \frac{\omega'_L}{\omega^2}\right), \tag{2.23}$$

so it has negative sign in the LH range and positive sign in the RH range, and it is zero at the transition frequency ω_0, which corresponds to infinite phase velocity and infinite guided wavelength. Indeed, phase velocity v_p, group velocity v_g and guided wavelength λ_g are expressed as:

$$v_p = \frac{\omega^2\omega'_R}{\omega^2 - \omega'_R\omega'_L}, \tag{2.24}$$

$$v_g = \frac{\omega^2\omega'_R}{\omega^2 + \omega'_R\omega'_L}, \tag{2.25}$$

$$\lambda_g = \frac{2\pi}{|\beta|} = \frac{2\pi}{\left|\frac{\omega}{\omega'_R} - \frac{\omega'_L}{\omega}\right|}. \tag{2.26}$$

In contrast to the unbalanced CRLH TL, the balanced TL is gapless, so there is no stop band and therefore no frequency at which group velocity is equal to zero. This can be seen because β in Eq. (2.19) is purely real (and then γ purely imaginary) at all frequencies from $\omega = 0$ to $\omega \to \infty$ whereas the unbalanced TL exhibits a usually undesired stop band in the frequency range extending from $\min(\omega_{se};\ \omega_{sh})$ to $\max(\omega_{se};\ \omega_{sh})$, where γ in Eq. (2.15) is purely real. At transition frequency ω_0, the CRLH TL exhibits nonzero group velocity v_g, infinite phase velocity v_p and infinite guided wavelength λ_g, which means that the electrical length of the line is zero. Therefore, although β is zero at ω_0, wave propagation still occurs, and, in addition, the phase shift is zero: $\phi(\omega_0) = -\beta(\omega_0)L = 0$.

2.2.3 CRLH TL Application

Metamaterial structures and, in particular, transmission lines based on CRLH unit cell have generated great interest in the last years. More specifically, this trend is due to the possibility of modifying the dispersion diagram $\beta(\omega)$ according to the needs, thanks to changes in the cell structure using parasitic inductances/capacitances either in distributed or lumped way. With dispersion engineering techniques it's possible to change the shape of β and later exploit its non-linearity in frequency.
In this way, for example, the backward and forward waves that occur on a realized MTM TL were found especially attractive to realize backfire to endfire scanning Leaky Wave Antenna (LWA) (Chap. 3). This is a *radiated wave* application, opposed to *guided wave* application, in which the EM field remains confined in the MTM structure. The often conflicting requirements of, for instance, efficiency, bandwidth, directivity, weight, size, and cost have made the design tasks onerous for antenna engineers with traditional schemes. The metamaterial inspired engineering of antennas and their performance characteristics have provided an alternative approach to address these pressing issues. Moreover, forbidden propagation bands and controllable dispersion properties of electromagnetic band gap (EBG) structures obtained with MTM have also been employed for novel waveguide, resonator, and filter designs.

An example of guided wave application is the microstrip dual-band branch-line coupler (BLC) [53]. Conventional BLC can only operate at their design frequency (f_1) and at their odd harmonics ($3f_1$, $5f_1$, ...). To overcome this limitation, the classical BLC can be modified by replacing its RH TLs with CRLH TLs to obtain a novel BLC with an arbitrary second operating frequency. Since the dispersion curve β_{PRH} of the RH TL is a straight line (see for example Fig. 2.5), the design frequency f_1 at -90° shift determines the next possible working frequency $3f_1$ at -270°. By changing the slope of dispersion diagram and making it non linear in frequency, the two usable frequencies can be varied and can be chosen as any arbitrary pair f_1, f_2 for dual-band operation.

A unique feature of CRLH metamaterials is that a null phase constant β can be achieved at a non-zero frequency, in particular in the balanced version of the CRLH TL as we can see in Fig. 2.6 and Eq. (2.19). Therefore, the electrical length $\Delta\phi = \beta L$ can be zero and negative. This property can be used to create *Zeroth* Order Resonator (ZOR) [54]. The main advantage of this structure is that the resonance frequency is independent of the dimensions

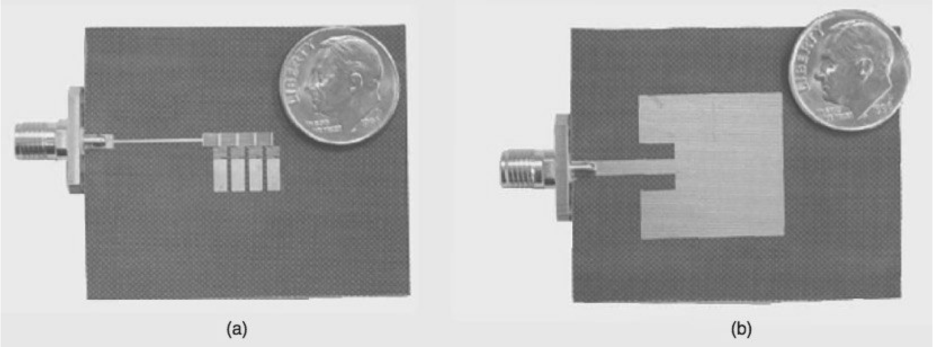
(a) (b)

Fig. 2.7: Four cell ZOR antenna (a) and microstrip patch antenna (b) on the same substrate and same frequency 4.88 GHz, from [54]

of the structure, but depends only on the reactive loadings. Thanks to this characteristic, theoretically arbitrarily small resonators can be developed.

The ZOR concept can be used to construct a zero-order resonating antenna, such as the microstrip CRLH antenna [54] depicted in Fig. 2.7(a). Since resonance does not depend on physical dimensions, the size of the antenna can be smaller than a half-wavelength, and can lead to significant miniaturization techniques. The antenna size is mainly determined by the reactive loadings in its unit cells. The prototype shows the size reduction that is possible with a ZOR antenna with a design frequency of 4.88 GHz. The size of the antenna is 10 mm, while the length of the $\lambda/2$ microstrip patch antenna with the same substrate and design frequency is 20.6 mm. The antenna is realized cascading 4 unit cell composed by interdigital capacitor and shunt meander line, with inter-cell period of 2.5 mm.

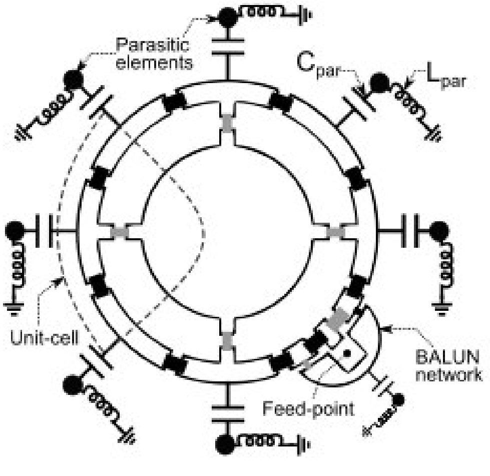

Fig. 2.8: Schematic of the ZOR-loop antenna, with one active element and highlighted unit cell and parasitic elements, from [55]

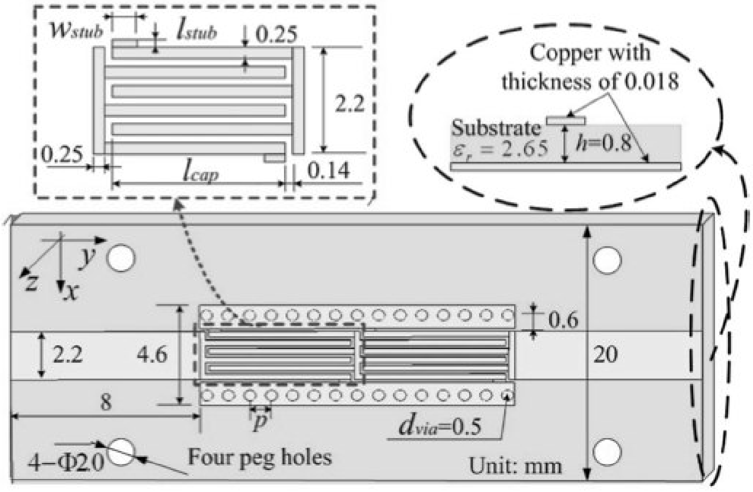

Fig. 2.9: Design of the CRLH unit cell on SIW, with interdigital capacitor, shunt stub inductors and via walls, from [57]

Another example of ZOR antenna is the reconfigurable ZOR-loop antenna presented in [55], actually used in commercial application for wireless router devices. The antenna (Fig. 2.8) exploits microstrip metamaterial structure to achieve small form factor, therefore the loop antenna size can be selected independently from the frequency of operation, set to 2.4 GHz. CRLH TL loading is obtained cascading 4 CRLH unit cells to form a loop, properly tuned to generate a zero order resonance mode. In this way, the design has been optimized to minimize the physical dimensions, maintaining an omnidirectional radiation pattern in the azimuth plane. Self-resonant parasitic elements are used to tune the direction of radiation achieving 8 possible configuration, while preserving good impedance matching for all configuration.

Besides the reported microstrip-based applications, that provide an easy and flexible implementation of LH parasitic elements, also SIW-based metamaterial TLs and antennas have been investigated. These are more recent and mostly related to my thesis' purpose.
In [56, 57], the same team of researchers presents two similar compact CRLH structures, developed on a SIW, investigating a super-wide bandpass filter and a phase-shifting TL. The proposed unit cell (Fig. 2.9) provide LH (C_L and L_L) contribution thanks to a series interdigital capacitor and a shunt stub inductor, shorted to via-walls, and the RH contributions (C_R and L_R) thanks to the shunt capacitance and series inductance provided by the natural parasitics effects of the metal sheets.

Using such a meta-structure, a series of super-wide bandpass filters are designed and fabricated, at different frequency bands, with the advantage of a better miniaturization. Indeed, the area of each unit cell is nearly 20% smaller than that of a CRLH microstrip or Coplanar

Waveguide (CPW) structure, at the same central frequency. Moreover, using the new structure, it's sufficient to change a single parameter (length of the interdigital capacitor L_{cap}) to optimize the filter at different working frequencies, while keeping good performance in both the passband and stopband. With the same concept, the developed phase shifter [56] can achieve different phase shifting varying L_{cap}, exploiting the non-linear phase response characteristic of CLRH TLs, at a fixed frequency of 5 GHz. The prototype has an electric length of only $0.212\lambda_0$, which has been decreased by 68.5% compared to the conventional microstrip line component.

Other significant examples of MTM application are the numerous SIW leaky wave antenna recently developed. These antennas take benefits from both the excellent guiding performance of SIW and the dispersion engineering techniques doable thanks to CRLH TL. The next chapter presents a review on LWA theory and shows some existing solution of SIW LWA based on CRLH TL.

Chapter 3

Leaky Wave Antennas

The Leaky Wave Antenna (LWA) has an history of at least 70 years, traditionally starting with the LWA implemented on a slotted Rectangular Waveguide (RWG), investigated and patented by W. W. Hansen in 1940 [58]. Radiation was achieved by opening a narrow slit along the side of the waveguide. Afterwards, through last years, this field was extensively developed by several researchers, among which the most cited are A. A. Oliner, T. Tamir, and D. R. Jackson [59, 60]. The main attraction of this antenna type is its achievable high directivity, wide matching bandwidth, and ability to scan angle with frequency. Moreover, LWA can be implemented on different transmission line structure, both planar or not, such as RWG, microstrip, coplanar waveguide, Substrate Integrated Waveguide (SIW). As we will see, the antenna can be modified with active elements, such as varactor, to realize a fixed frequency electronically controlled beamsteering [61].

The unique frequency scanning feature is realized by engineering the waveguide so that it can progressively leak energy as the wave propagates down the waveguide. Therefore, LWAs are considered *travelling wave* antennas. The difference with resonant ones is that the currents that generate the radio waves travel through the antenna in one direction, and do not interfere constructively. This is in contrast to a resonant antenna, such as the dipole or the patch, in which the structure acts as a resonator, with currents travelling in both directions, forming a standing wave that enhances radiation.

In this chapter I begin explaining the working principle of LWAs, and what's the relationship between frequency, phase constant β and main angle of radiation θ_{MB}, then reporting a brief classification of leaky wave antennas. I will continue focusing on LWAs based on Composite Right-Left Handed (CRLH) Transmission Line (TL), explaining also how we can steer the beam electronically at a fixed working frequency, concluding with some examples of LWA implemented on CRLH SIW.

3.1 Principle of Leakage Radiation

A Leaky Wave Antenna is a waveguiding structure which radiates its energy out to free space from a travelling wave, at a frequency belonging to *fast wave* region. The LWAs may be uniform, periodic, or quasi-uniform, with some differences in the way the EM field fulfil the radiation condition. Before considering particular features, the antenna firstly has to properly leak energy, and the primary requirement is therefore to ensure that our LWA operates in the fast wave frequency range, i.e. we need $\beta/k_0 < 1$. The term *fast wave* describes the faster phase velocity v_p of the wave travelling in the propagating direction, relative to that of the speed of light c, whereas *slow wave* indicates the frequency range in which $v_p < c$.

For a general understanding of the radiating mechanism [62, 63], we consider a weakly lossy two dimensional waveguide structure with the source located at $z = 0$, as in Fig. 3.1. The lower boundary of the waveguide, at $x = -h$, is a perfect reflecting layer such as a perfect electric conductor (PEC), whereas to permit radiation, the upper boundary of the waveguide, at $x = 0$, should be an imperfect reflecting boundary, that minimally disturbs the guided field and partially leaks energy. The partially reflective interface can take various forms, such as the interface between different material layers, narrow slots, periodic array of apertures or slots, array of parallel wires.

We consider a $\mathbf{y}$-oriented field $\mathbf{\Psi}(x, z)$ propagating along the $\mathbf{z}$-direction with propagation constant β:

$$\mathbf{\Psi}(x, z) = \mathbf{y}\, A_0\, e^{-j(k_c x + \beta z)}, \tag{3.1}$$

where k_c is the cutoff wavenumber, determined by the waveguide dimensions and the propagation mode, and A_0 is the initial amplitude of the field. At the interface between the antenna and free space ($x = 0$), the reflected field amplitude is exponentially reduced in proportion to the attenuation constant α, therefore, the longitudinal wavenumber k_z is complex and it is expressed as $k_z = \beta - j\alpha$. The field inside the antenna will continue propagating through the waveguide, bouncing back and forth between the interfaces in a zigzag manner, until either all the energy is leaked out, or is dissipated, or the line is terminated with a matched load.

From Maxwell equations and known EM boundary conditions, the tangential part of the complex wavenumber vector $\mathbf{k} = \mathbf{k}_x + \mathbf{k}_y + \mathbf{k}_z$ is continuous at the interface between free space and the waveguide. Thus, the waveform in free space exhibits the same z dependence

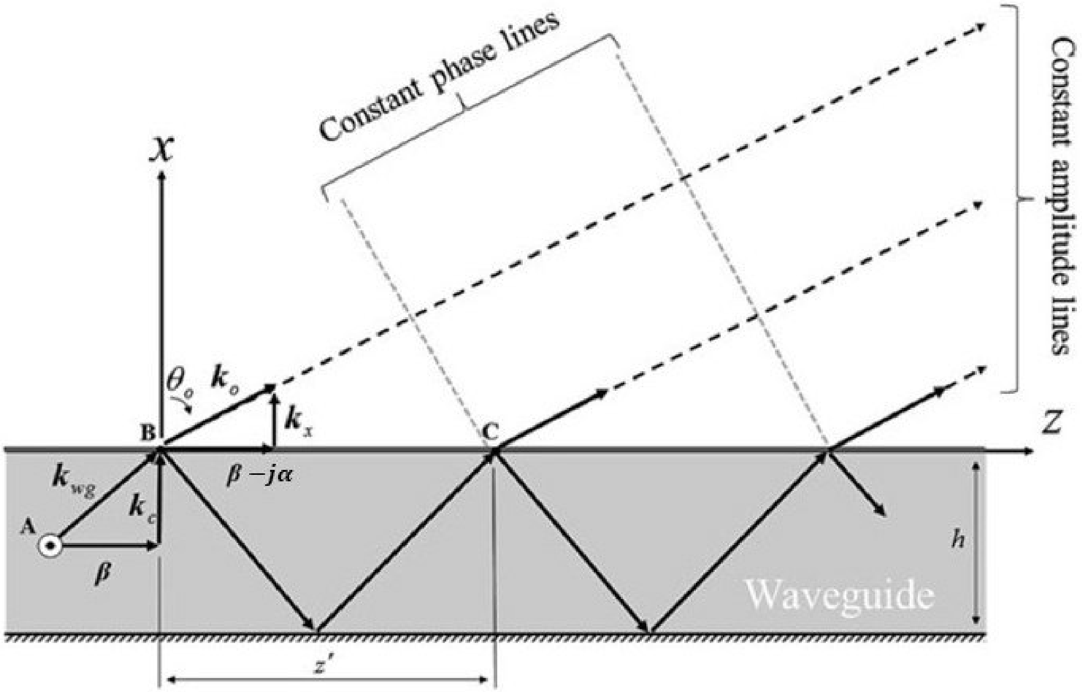

Fig. 3.1: Side view of an ideal waveguide with leakage radiation, from [62]

as in Eq. (3.1) and it is:

$$\mathbf{\Psi}(x,z) = \mathbf{y}\, A_0\, e^{-j(k_x x + k_z z)} = \mathbf{y}\, A_0\, e^{-\alpha z} e^{-j(k_x x + \beta z)}. \tag{3.2}$$

Therefore we can get the dispersion relation directly above the interface of the antenna:

$$k_x = \sqrt{k_0^2 - (\beta - j\alpha)^2}, \tag{3.3}$$

where $k_0 = \omega / c$ is the free space wavenumber. Considering small losses, we have $\alpha \ll \beta$ and we can neglect α simplifying Eq. (3.3) to:

$$k_x = \sqrt{k_0^2 - \beta^2}\,. \tag{3.4}$$

To support wave propagation away from the interface, k_x has to be real. Then, underlining the dependence on frequency of the propagation constant $\beta = \beta(\omega)$, we need:

$$\beta(\omega) < k_0\,. \tag{3.5}$$

This important relation indicates that the antenna has to operate in the fast wave region to enable energy radiation. A property of leaky wave structures related to the distinction between slow and fast wave is the switch between guided wave and radiated wave, respectively. If the phase velocity $v_p = \omega/\beta$ is smaller than the speed of light in free space $c = \omega/k_0$ (slow wave), then $\beta(\omega) > k_0$, consequently k_x is imaginary and this translates in an evanescent wave that decays exponentially in the free space away from the structure; it is thus the case of a purely guided wave, confined in the waveguide. In contrast, if $v_p > c$ (fast wave), or equivalently $\beta(\omega) < k_0$, the wavenumber k_x is real and therefore the structure radiates into free space (radiated wave).

The radiation pattern can be obtained by taking the Fourier transform of the aperture distribution. In the case where the geometry is kept consistent along the length of the antenna, we have an exponentially decaying amplitude distribution along the length of the guide. If the length of the antenna is modelled as being theoretically infinite, the resulting radiation pattern can be computed with acceptable accuracy as [59, 64]:

$$R(\theta) \approx \frac{\cos^2\theta}{\left(\frac{\alpha}{k_0}\right)^2 + \left(\frac{\beta}{k_0} - \sin\theta\right)^2} . \tag{3.6}$$

This pattern does not contain any sidelobes, but as the length is decreased the expression for $R(\theta)$ changes and sidelobes appear, that in a leaky wave antenna are often significant. We observe that the frequency dependent propagation constant $\beta(\omega)$ mainly dictates the beam scanning angle, and α shapes the amplitude distribution of the antenna. The main beam angle $\theta_{MB}(\omega)$ of the LWA, operating in the fast-wave condition, is determined by the ratio between $\beta(\omega)$ and k_0:

$$\theta_{MB}(\omega) = \sin^{-1}\left[\frac{\beta(\omega)}{k_0}\right] = \sin^{-1}\left[\frac{c\beta(\omega)}{\omega}\right] . \tag{3.7}$$

We underline that θ indicates the angle between x and z axis (Fig. 3.1), i.e. the angle with respect to the normal of the structure. Therefore, we distinguish between:

- $\beta(\omega) < 0$, consequently $\theta_{MB} < 0$: radiation towards ***backfire***;
- $\beta(\omega) = 0$, consequently $\theta_{MB} = 0$: ***broadside*** radiation;
- $\beta(\omega) > 0$, consequently $\theta_{MB} > 0$: radiation towards ***endfire***.

From the above relation, it is clear the importance of choosing an appropriate structure (such as a CRLH TL) that permits the possibility of modifying the shape and the values of β, to enable a beamsteering application.

Moreover, for antennas with axial physical length L, the main beam width $\Delta\theta_{MB}$ can be approximately found as:

$$\Delta\theta_{MB} \approx \frac{1}{\frac{L}{\lambda_0}\cos\theta_{MB}}\,. \tag{3.8}$$

The unity factor in the numerator of Eq. (3.8) changes depending on the particular amplitude distribution [64]. For example, for an aperture distribution that remains consistent over the length of the antenna, the numerator is replaced by 0.88, while a tapered distribution could have a numerator greater than 1.25.

The length L is generally adjusted so that approximately 90% of the power is radiated. The remainder is then absorbed by a matched load, and L depends on a set value of α. An initial length satisfying this condition can be estimated by taking the ratio of the power leaving through the opposite end of the antenna structure over the input power, and then equating the ratio to 10%, obtaining [62]:

$$L \approx \frac{0.18\,\lambda_0}{\alpha/k_0}\,. \tag{3.9}$$

Whereas in a purely guiding structure the real part of the complex propagation constant usually represents an undesirable loss coefficient, the leakage factor α in a LWA is clearly necessary, as it is related to radiation. If α is small, the structure can be made long before all the power is leaked out: therefore, the radiation aperture is large and high directivity is obtained [50]. An LWA may therefore achieve very high directivity for large antenna lengths, as we can see also in Eq. (3.8): if we increase L, the beam width shrinks. These properties translate in a high achievable gain, that with the increase of L can be increased toward a limit value G_{max}, as we will see in the simulations.

Moreover, there are not strict constraints about structure dimensioning, since the length L can be increased independently of frequency, as long as most of the power is left near the end of the structure.

In contrast to array antennas, LWAs do not require a complex feeding network: they can be fed by a simple transmission line connection, while they offer directivity and scanning performances comparable to those of arrays. We can obtain beamforming without the need of phase shifter, and this could lead to a simpler structure, minimal losses, and to lower costs. Generally, a unidirectional *fan* beam is achieved, and subsequently several LWAs can naturally be arrayed to form a 2D aperture and radiate a pencil beam, which may be steered by frequency tuning along the longitudinal plane (θ angle, elevation beam steering) and by phase shifter tuning along the transverse plane (φ angle, azimuth beam steering). It is then clear that an LWA can be a promising candidate for small cell mmWave application in a 5G network, where are required high directivity radiation and beam steering capability.

3.1.1 LWAs Classification

Leaky Wave Antennas can be divided into several categories: the first distinction is between one and two dimensional LWAs, then they can be identified as periodic, uniform or quasi-uniform structures [63, 65]. A 1D structure supports a wave travelling in a single, fixed direction, whereas a leaky wave that originates from a 2D guiding structure propagates radially from the feed point.

Uniform LWAs have an invariant transverse cross-section along the propagation-leakage **z**-axis, and radiate in the dominant mode or a higher order fast wave mode of the structure. Since their phase constant β is generally positive and non-zero for all frequencies, they are confined to forward radiation, excluding broadside, and their applications are therefore quite restricted. A uniform LWA can be realized by partially opening the closed structure to allow the fundamental mode to couple energy to the free space. Among the three classes of LWAs, the uniform ones have a relatively simpler form factor, but a limited beam-scanning range.

Periodic LWAs have a structure with a periodic modulation along the axis of propagation. This is usually in the form of periodic discontinuities for one of their features (metallizations, slots, permittivity or permeability). Due to their periodicity, according to Bloch-Floquet theory, they support an infinite number of space harmonics [63]: $\beta_n(\omega) = \beta_0(\omega) + 2\pi\, n/p$, where p is the period and n is an integer. They typically radiate in a higher-order space harmonic, often the order $n = -1$, since their fundamental space harmonic β_0 is generally slow and therefore non radiative. In this case the structure is designed so that the desired space harmonic is placed in the fast-wave region of the dispersion diagram, and also it has to avoid overlapping with other space harmonics: radiation with single beam scanning will be achieved, and the field behaves as described in the previous section, where β now represents the phase constant of the appropriate space harmonic β_n. In contrast to their uniform counterparts, periodic LWAs can scan from backfire to endfire range, since many of their space harmonics fully cross the positive and negative fast-wave dispersion regions, i.e. β can assume negative, positive, and zero value. However, they suffer from very poor radiation efficiency at broadside ($\beta = 0$) due to the standing-wave regime occurring at the corresponding frequency, where the leakage constant drops to zero.

Quasi-uniform LWAs are topologically similar to periodic antennas and electromagnetically similar to uniform ones. They have a periodic structure, but their period is much smaller than the guided wavelength λ_g of the travelling wave, so that they radiate in their fundamental space harmonic $n = 0$. This configuration is very interesting, considering that it can solve the broadside issue of periodic and uniform LWAs. In particular this is the case of a leaky wave antenna implemented on a CRLH TL. Caloz, Itoh and Liu [65, 66] are among the first researchers that investigated and elaborated this particular type of antenna.

3.2 Metamaterial Based LWA

Metamaterial (MTM) TL concept and its implementation on CRLH TL have been applied to leaky wave antennas, and have led to a remarkable amount of applications, turning out to represent a powerful scientific innovation. These applications included the first LWAs capable to scan the entire space, from backfire to endfire, without suffering from the collapse of gain at broadside [66] produced by a stopband in previous LWAs.

As discussed in Sec. 2.2.1, CRLH TL are metamaterial structures composed by a series of periodic unit cell, modelled as a LH series capacitance C_L and shunt inductance L_L and a RH series inductance L_R and shunt capacitance C_R. The size (and period) of the unit cell p must be much smaller than the guided wavelength ($p \ll \lambda_g$) so that, in the frequency range of interest, the structure behaves as an effectively homogeneous transmission line. In this way, MTM LWAs macroscopically behave as uniform LWAs, and may be considered electromagnetically belonging to this category even if they are structurally periodic [50].

In principle, any open CRLH TL structure can operate as a LWA, since the CRLH dispersion curve always penetrates in the radiation region, i.e. where $\beta < k_0$. We start considering the general dispersion relation (2.20) of a balanced CRLH TL structure (Sec. 2.2.2):

$$\beta(\omega) = \frac{1}{p}\left(\omega\sqrt{L_R C_R} - \frac{1}{\omega\sqrt{L_L C_L}}\right) . \tag{3.10}$$

We remember that in the balanced case: i) there is no band gap; ii) at transition frequency ω_0 we have $\beta(\omega_0) = 0$, $v_p(\omega_0) = \infty$, $v_g(\omega_0) \neq 0$; iii) the characteristic impedance Z_c is independent of frequency, allowing broadband impedance matching.
Moreover we distinguish between i) RH range, where $\omega > \omega_0$ and $\beta > 0$; ii) LH range, where $\omega < \omega_0$ and $\beta < 0$. The dispersion diagram of a balanced CRLH TL in Fig. 3.2 highlights the working frequency regions of a CRLH LWA.

The *airline* $\omega = \pm k_0\, c$ delimits the radiation (leaky) region $\beta < k_0$, indeed the $\omega - \beta$ diagram shows the following four distinct regions: the LH guided region, the LH leaky region, the RH leaky region, and the RH guided region. If the CRLH structure is unbalanced, there is an additional gap region between the LH leaky and RH leaky regions, that is unfavourable for antennas because it prevents broadside radiation and introduces a gap in the scanning range. We remember that the quantity $\beta(\omega)/k_0$ depends on frequency, therefore the main beam angle θ_{MB} is function of frequency (Eq. 3.7).

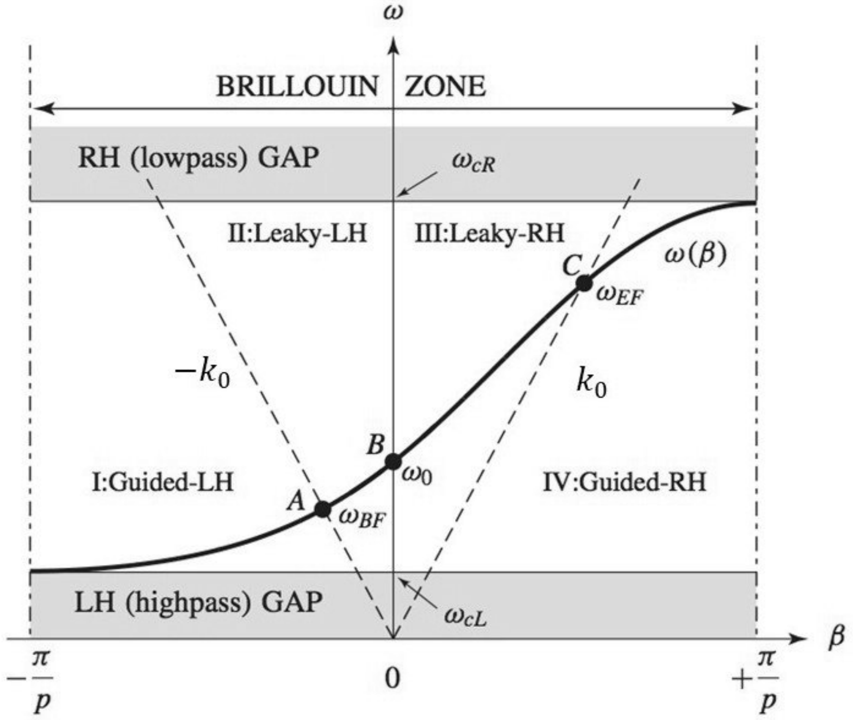

Fig. 3.2: Dispersion diagram of a balanced CRLH TL structure, operating as an LWA, with its 4 distinct regions, from [50]

Observing Fig. 3.2 and Fig. 3.3 we can distinguish between three fundamental frequency ranges:

- **Backward region,** $\omega_{BF} \leq \omega < \omega_0$: We have $\beta < 0$, therefore, according to Eq. (3.7), in this frequency range the main beam is directed toward backfire, $\theta_{MB} < 0$. At the limit frequency ω_{BF}, where $\beta = -k_0$, backfire radiation is achieved, i.e. $\theta_{MB} = -90°$;
- **Broadside,** $\omega = \omega_0$: Broadside radiation, i.e. $\theta_{MB} = 0$, is achieved at the frequency ω_0, where $\beta = 0$;
- **Forward region,** $\omega_0 < \omega \leq \omega_{EF}$: In this frequency range we have $\beta > 0$, therefore the main beam is directed toward endfire, $\theta_{MB} > 0$). At the limit frequency ω_{EF}, where $\beta = +k_0$, endfire radiation is achieved, i.e. $\theta_{MB} = +90°$.

Therefore, backfire-to-endfire frequency scanning capability is achievable with an open balanced CRLH structure. This is a very unique feature for an LWA, which cannot be obtained in conventional uniform or periodic LWA structures. Moreover, broadside radiation capability is a consequence of the fact that the usual frequency gap of CRLH TL is suppressed: consequently, a travelling wave always exists along the structure and broadside radiation can occur. Finally, another advantage is that, operating in a fundamental mode, this LWA can be fed by a very simple and efficient mechanism, such as a simple line, in contrast to typical LWA structures.

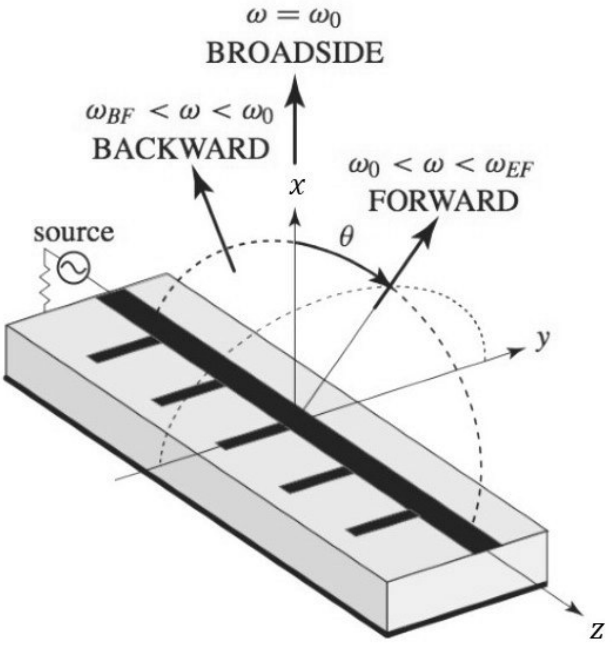

Fig. 3.3: Schematic CRLH LWA, highlighting the three radiation region: backward ($\beta < 0$), broadside ($\beta = 0$), forward ($\beta > 0$), from [50]

A useful array factor approach has been developed [67], considering the LWA as an array antenna in which the radiating elements are the unit cells. The radiation pattern $R(\theta)$ is then well approximated by the array factor $AF(\theta)$ of the equivalent array:

$$R(\theta) \approx AF(\theta) = \sum_{n=1}^{N} = I_n \, e^{j(n-1)k_0 \, p \sin\theta + j\xi_n}, \tag{3.11}$$

with

$$\xi_n = (n-1)\, k_0 \, p \sin\theta_{MB} \qquad \text{and} \qquad I_n = I_0 \, e^{-\alpha(n-1)p}, \tag{3.12}$$

where N and p represent the number of unit cells and period of the structure, I_n is an exponentially decaying function, determined by the leakage factor α. This formula may be applied to have a good approximation of the resulting radiation pattern, and provides excellent results in condition that the electrical length of the structure is sufficiently large ($L/\lambda_0 > 1$) [50].

3.2.1 Electronically Controlled Beam-Steering LWA

Although the wide angle scanning capability, the need to sweep frequency in order to steer the beam is a disadvantage, which has limited LWAs application in modern communication systems, generally requiring fixed frequency operation. Various studies have been conducted to develop frequency independent LWAs with another scanning mechanism than frequency tuning [50, 61, 68–70].

In [68] they used PIN diodes as switches to electronically vary the radiation angle by controlling the guided wavelength. However, only two discrete radiation angles were available in this approach because diodes have only two states: biased and unbiased.
The researchers in [69] reported a magnetically scanning LWA, built on a ferrite slab structure, in which the radiation angle is scanned by tuning a DC magnetic field.
Another possibility is to control the scanning angle thanks to liquid crystal insertion in the CRLH structure [70]. The proposed LWA can steer the main beam angle at a fixed frequency of 77 GHz. Liquid crystal material is placed under the gap capacitor in the unit cell, and the application of a DC voltage produces an orientation of the liquid crystal molecules parallel to EM field. This orientation corresponds to a difference between the two dielectric permittivities, and one can change the value of the capacitance and therefore steer the beam. Liquid crystal concept has attractive properties such as weak losses in the mmWave band, but at the same time is complicated to realize and it's not suitable for commercial application.

Very interesting is the electronically controlled Leaky Wave Antenna proposed in [61]. The concept developed in the cited article is the main idea that inspired the structure designed and simulated in my thesis. The research presents an LWA implemented on microstrip line, modified thanks to varactor diodes inserted in the unit cell. A varactor is basically a diode with a variable capacitance, controlled by the applied reverse bias voltage V. The proposed antenna is therefore capable of continuous beam steering at a fixed frequency by tuning the applied voltages. In addition, it provides a beamwidth control by using a nonuniform biasing distribution of the diodes. This concept represents an attractive alternative to conventional phased arrays with its advantages of requiring only one radiating element, utilizing a very simple and compact feeding mechanism and not necessitating any phase shifters.

As we have seen (Eq. 3.7) the main beam angle θ_{MB} of an LWA is function of the propagation constant β. Since the propagation constant (Eq. 3.10) in a CRLH TL depends both on frequency ω and on the LC parameters ($C_L,\ L_L,\ C_R,\ L_R$), once the CRLH structure is fixed, the angle becomes frequency dependent: $\theta_{MB} = \theta_{MB}(\omega)$. If we want to get around the problem of frequency dependence, we have to find a way to modify the inductance or capacitance parameters of the CRLH TL. In this case, varactor diodes can be integrated along the structure in each cell to provide a continuously variable capacitances via the control of their reverse bias voltage V. Using this scheme, we directly modify the constitutive parameters, and the propagation constant and the angle become voltage (and frequency) dependent: $\beta = \beta(V,\ \omega)$ and $\theta_{MB} = \theta_{MB}(V,\ \omega)$.

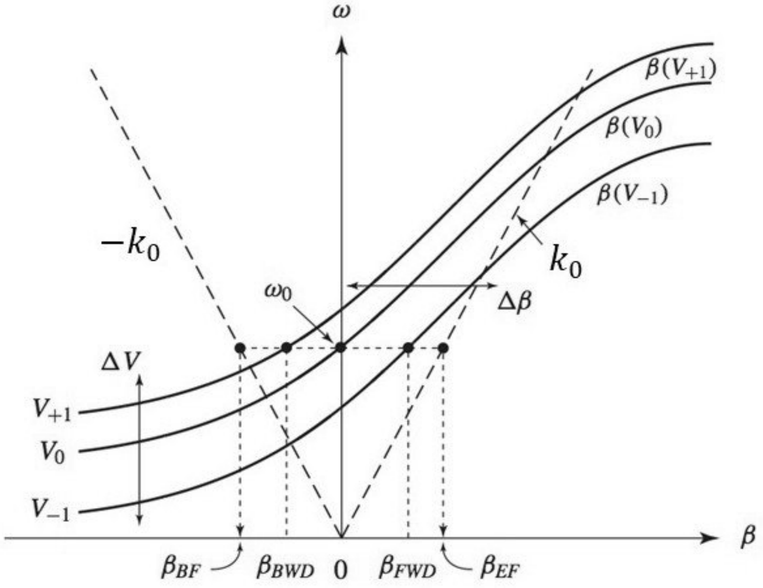

Fig. 3.4: Dispersion diagram of an electronically scanned LWA at fixed frequency ω_0, where we observe the shift of β at different bias voltages V, from [50]

As the value of the varactors capacitance is varied, the dispersion curve in the $\omega - \beta$ plane is shifted and also slightly altered in shape. Therefore we obtain an almost continuous family of curves $\beta(V)$, as we can observe schematically in Fig. 3.4, and the radiation angle θ_{MB} is varied at a fixed frequency ω_0 by varying voltage V. If the value of β can be shifted from $\beta_{BF} = -\omega_0/c$ to $\beta_{EF} = +\omega_0/c$ in a voltage range $[V_{BF},\ V_{EF}]$, a wide angle electronic scanning is achieved. It should be noted that the CRLH structure needs to be balanced only relatively to the dispersion curve crossing the frequency axis at ω_0 [50] since ω_0 does not correspond to the transition frequency of the other curves. This fact relaxes the design constraints of the antenna.

The antenna investigated in [61] is capable of an angle scanning range of $[+50°,\ -50°]$ in a bias voltage range of [0 V, 22 V]. The capacitance value of the varactor diodes decreases exponentially as the reverse bias voltage increases, and so we have a variation of the impedance Z and the admittance Y that reflects on β. As the voltage V increases, the phase constant β decreases toward zero and then becomes negative, so the main beam angle θ_{MB} will be steered from endfire toward backfire as the voltage is increased from low values. The realized LWA achieved a gain of 18 dBi at broadside, working at $f = 3.3$ GHz.

3.2.2 LWA on Substrate Integrated Waveguide

Besides the microstrip line application of LWA structure, there have been lots of researches also on LWAs implemented on Substrate Integrated Waveguide (SIW) [71–78], following

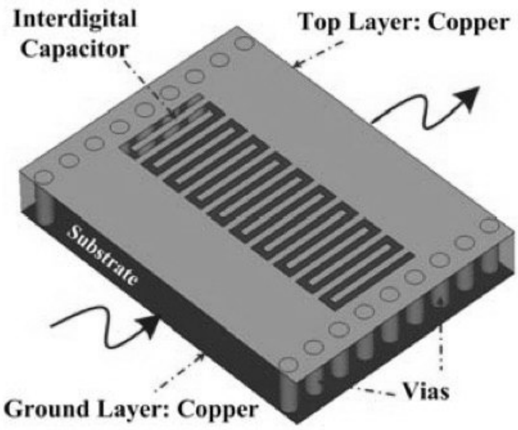

Fig. 3.5: Proposed unit cell on SIW with interdigital capacitor, from [71]

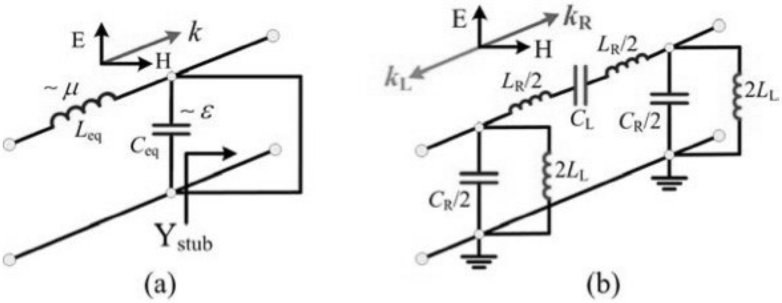

Fig. 3.6: Equivalent circuit model of an SIW unit cell without slots (a) and with slots (b), where are visible the LH and RH contributions, from [71]

the theory explained in Sec. 3.1 and 3.2

The working principle remains the same, and in particular is interesting the way of modifying the structure to introduce the necessary LH contributions, that are provided by slots of various shapes etched on the upper metal plate, and can be subsequently loaded with varactors.
In particular, in [71], Dong and Itoh carry out an interesting analysis on their SIW CRLH LWA. The developed SIW unit cell is depicted in Fig. 3.5 whereas the complete LWA is obtained by cascading 15 elementary cells. From this research, they deduce that the SIW can be modeled as a conventional two-wire TL with distributed series inductance L_R and distributed shunt capacitance C_R, and the metallic vias, represented as a short-circuited stub, provide the shunt inductance L_L. Moreover, the series capacitance C_L is due to an *interdigital* capacitor etched on the top metal surface, obtaining a complete CRLH behavior.
In Fig. 3.6 we observe the equivalent circuit model for the SIW unit cell without the slots, which is similar to the traditional rectangular waveguide, with an additional stub due to vias contribution, and the SIW unit cell with slots, where the LH contribution are visible.
They underlined that the series slot also plays the role of a radiating element for the LWA,

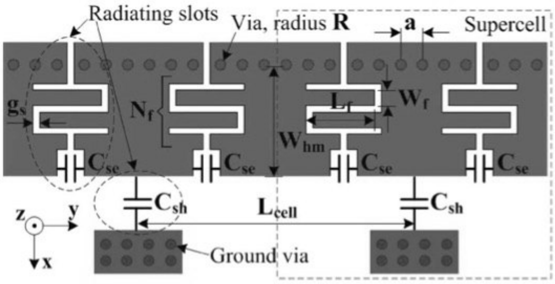

Fig. 3.7: Unit cell of the HMSIW LWA loaded with varactors, from [75]

in particular increasing the width and the length of the slots will make the radiation more efficient. Also, increasing the slot width leads to a decrease of C_L while increasing the slot length results in an increase of C_L, therefore enhancing the radiation does not conflict with achieving a balanced case, since we have to maintain valid the relation (2.18). The angle scanning capability is wide, indeed they get a steering from $\theta = -70^\circ$ at $f = 8.6$ GHz, to $\theta = +60^\circ$ at $f = 12.8$ GHz. Finally, they obtain a gain from 6 to 10 dBi, variable along the angle scanning.

Generally, the slots can be of various shape [72, 73]. Besides of the interdigital slot, there can be also simpler rectangular slots, placed symmetrically with respect to the waveguide longitudinal axis, or slots covering the entire SIW length, or other configurations. Moreover, various studies showed the possibility of integrating varactors in the SIW structure to obtain an electronically steerable beam [75–78]. For this application, researchers have focused on a modified SIW, the Half-Mode Substrate Integrated Waveguide (HMSIW), since it gives more design possibilities and more compactness. The HMSIW LWA in [75] presents this concept, designing a unit cell with interdigital capacitor and integrated varactors. The working frequency is set to 6.5 GHz, and the diodes are swept in a capacity range from 0.15 pF to 0.5 pF. They managed to steer the beam from $\theta = -31^\circ$ to $\theta = +35^\circ$, maintaining a gain of at least 9.5 dBi. In Fig. 3.7 is depicted the HMSIW LWA configuration. The presented researches are clearly important with respect to this project, since I retrieved precious information and guidelines to start the design of the proposed electronically beamsteering LWA implemented on CRLH SIW, described in the next chapters.

Chapter 4

Design of Reconfigurable Leaky Wave Antenna

After having analyzed and resumed the state of the art regarding Substrate Integrated Waveguide (SIW), Composite Right-Left Handed (CRLH) Transmission Line (TL), Leaky Wave Antenna (LWA), and thus having examined the necessary theoretic bases, we go on describing the developed antenna system. As already discussed, the concept is based on an SIW with microstrip transition, and the antenna type is the Leaky Wave working in the frequency range of 26 - 30 GHz, composed by a sequence of N_{cell} cell with a CRLH behaviour. All the simulations have been conducted using Ansys HFSS simulation software [36].

The LWA does not have a predetermined working frequency, as we have seen, since the main radiation angle varies with frequency, but we tuned the frequency scanning antenna to get a broadside radiation corresponding to $f = 28$ GHz. Next, variable capacitors will be added to the unit cell, in order to enable a fixed frequency ($f_w = 26.5$ GHz) angle scanning, tuning the bias voltage applied to the varactor diodes.

The system has been designed to achieve beamsteering in the elevation plane, starting from some basic and spread concept about common requirements for existing 5G antennas, with some constraints regarding peak gain, bandwidth, scanning range, beamwidth. These indicatively are:

- Working frequency range: 24.25 - 27.5 GHz or 27.5 - 28.35 GHz (see Sec. 1.2);
- Realized gain: approximately 15 dBi;
- Instantaneous bandwidth: 0.8 - 1 GHz;
- Half Power Beam Width (HPBW): approximately 5°;
- Elevation scanning angle range: at least 30° - 40°.

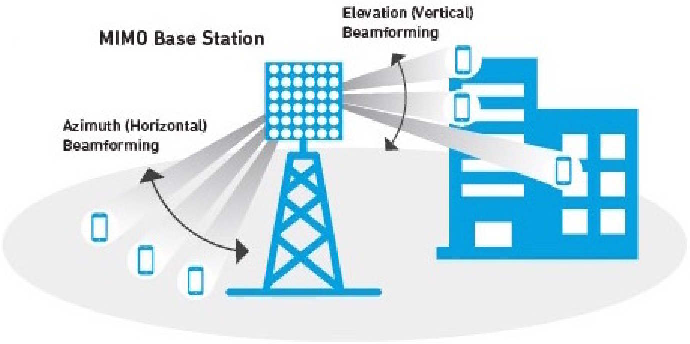

Fig. 4.1: Small cell use case with dual plane beamsteering characteristic

The designed antenna is suitable for outdoor small cell 5G application, where the communication range is limited to hundreds of meters and are required beamforming/beamsteering capability, a high directivity beam, MU-MIMO possibility. These are attainable functionalities with the developed LWA, considering that the conducted study is the first step of a project that has to be improved, to reach a full capability system.

Moreover, the single LWA can be used with other identical antennas in an array-like way: this configuration can enhance peak gain and can achieve beamsteering in both azimuth and elevation plane, the first thanks to a digital controlled phase shifting applied to single LWAs, the latter with an analog control through varactor tuning. In this way the system can obtain a narrower beam, steerable in a wide angle range, that can serve different areas and multiple users in a single area simultaneously, with reconfiguration times in the order of hundreds of nanoseconds. As depicted in Fig. 4.1, the dual plane beamsteering is required to: i) provide high speed connectivity at users distributed on different height levels, e.g. different floors of a building; ii) serve users spread in a fixed level area at various azimuth directions.

The LWA has been conceived, designed and then simulated working principally with the simulation software Ansys HFSS, starting from previously cited similar studies. The concept remains confined in the simulated results: the implementation of a prototype did not take place, because of mechanical problems related to the realization of such small features, and issues regarding the availability on time of the varactors. However, although simulations are clearly not so reliable as the tests on a concrete prototype, they are quite significative and they give an idea on the performances achievable by the developed antenna. The conducted work has to be considered more as a feasibility study, in which the designed system is analyzed in terms of pros-cons and trade off, regarding a company point of view that wants to create a developable and commercial product.

In the following chapter the design of two versions of the antenna are presented, starting from the waveguide used as the underlying structure, with its dimensioning and the microstrip transition performances. Then, the design and analysis steps are reported, explaining how the LWAs have been developed, concluding with the design of both the **frequency scanning LWA** and the **varactor tuned** version. In the next chapter the simulated results of the antennas will be presented, together with the performance analysis.

4.1 SIW and Mictrostrip Transition Design

The first step of our work is the design and the tuning of the SIW and the microstrip transition, to make them suitable for an LWA application. As examined in Sec. 2.1.1, there are some guidelines (2.3), (2.5), (2.6), to design an SIW with an indicative cutoff frequency f_{cut}, thus optimized in a certain frequency band.

Initially we have to choose the substrate material. Since at mmWave the major source of power losses in an SIW is the dielectric, the chosen material has to guarantee good EM propagation, minimizing the leakage. Therefore, we need a material with low dielectric constant ε_r and low loss tangent $\tan\delta$, since the losses are directly proportional to this quantity. Having fixed these requirements, the Rogers RT/duroid 5880 has been selected, considering also its widespread choice in numerous papers and prototypes of mmWave antennas for 5G application. This material has the following characteristics[1]:

- Relative dielectric constant $\varepsilon_r = 2.2$, loss tangent $\tan\delta = 0.0009$;
- Standard substrate thickness $H_{sub} = 0.787$ mm;
- Standard copper cladding thickness $H_{cop} = 18$ μm.

Once chosen the dielectric, H_{sub} and ε_r are fixed, and we can proceed with the dimensioning of the SIW. Observing Fig. 4.2, we remember that the needed parameters for the waveguide and the microstrip transition are: SIW width W_{SIW}; via diameter d; via pitch p; width and length of the tapered section W_{tap} and L_{tap}; width of the microstrip line W_0.

Setting an initial cutoff frequency $f_{cut} = 20$ GHz and a working frequency $f = 28$ GHz, with (2.3) we obtain the width of the equivalent Rectangular Waveguide (RWG), $a_{RWG} = 5.1$ mm. Afterwards, from (2.5) it results $W_{SIW} = 5.6$ mm, having set d to an initial indicative values of 1 mm, and $p = 2d$, following the constraints (2.6). Starting from these results, the values have been modified, reaching a trade off between performances and mechanical feasibility. Thanks to full wave parametric simulations, we have investigated the guiding

---

[1] From Rogers Corporation data sheet, `http://www.rogerscorp.com/acs/products/32/rt-duroid-5880-laminates.aspx`

characteristics of the designed SIW in terms of scattering parameters, adapting the waveguide dimensions to the constraints.

Increasing the pin diameter d and reducing pitch p cause a decrease of radiation losses due to gaps between via holes, but we have to consider mechanical issues related to pin drilling, where over-demanding dimensioning can lead to higher costs. Therefore, after some simulations, we set $d = 0.8$ mm and $p = 2d = 1.6$ mm.

Similarly, the SIW width has been modified also during the subsequent LWA design steps, for various reasons: i) to lower the cutoff frequency, ii) to enlarge the available region in which the slots will took place, allowing a more flexible design, iii) to shift the frequency at which $\beta(\omega) = 0$, i.e. change the transition frequency ω_0. Moreover, the used formulas are not strict rules, but they have to be intended as initial guidelines to begin the design, that subsequently has to be adapted according to needs. The final width of the SIW has been set to $W_{SIW} = 7$ mm.

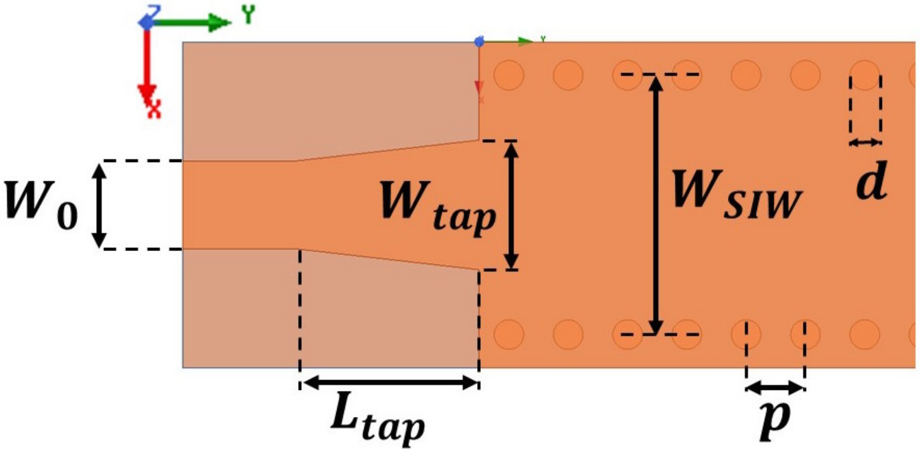

Fig. 4.2: Designed SIW and microstrip transition

W_{SIW}	p	d	H_{sub}	W_0	L_{tap}	W_{tap}
7	1.6	0.8	0.787	2.36	5	2.8

Tab. 4.1: Designed SIW and microstrip transition dimensions (all measures are in mm)

The next step is the design of the microstrip transition (Sec. 2.1.2), to permit the connection with a standard feeding microstrip line. Setting the characteristic impedance to $Z_0 = 50\ \Omega$, and following the cited formulas (2.8) and (2.9), we get the microstrip width, that results $W_0 = 2.36$ mm. Now, with the indications (2.10), found in the related scientific literature, we set width and length of the tapered section: $W_{tap} = 2.8$ mm and $L_{tap} = 5$ mm. With full wave simulations, the parameters have been tuned to minimize reflections at the interface between SIW and microstrip, in order to decrease power losses. Finally, the SIW and microstrip transition dimensions are reported in Tab. 4.1.

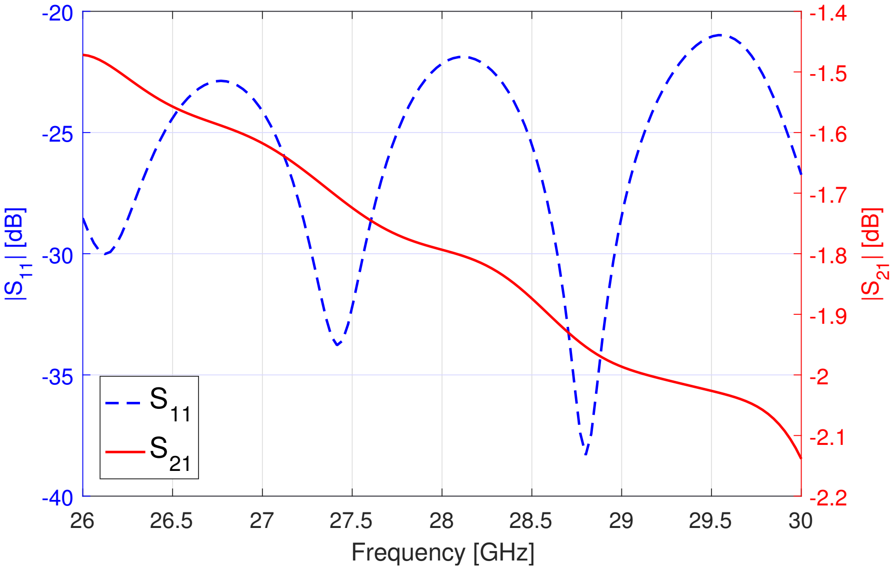

Fig. 4.3: Simulated scattering parameter $|S_{11}|$ and $|S_{21}|$ of the designed SIW with microstrip transition of Fig. 4.2

As already discussed, the SIW structure offers excellent guiding performances, similar to that of a bulky RWG, and they are confirmed by the simulated results. We can observe the scattering parameters of the designed SIW with microstrip transition in Fig. 4.3, for a waveguide of length $L_{SIW} = 80$ mm. The $|S_{11}|$ it's always lower than -20 dB, and also $|S_{21}|$ stays on a good range of values, despite of a degradation at higher frequencies. The realized parametric sweeps confirmed that the greater source of losses is the dielectric material, once the dimensions was optimized. It is generally observed a good EM propagation, noticing also the electric field magnitude distribution depicted in Fig. 4.4.

Notice how the transition gradually transforms and guides the EM field, exciting the TE_{10}

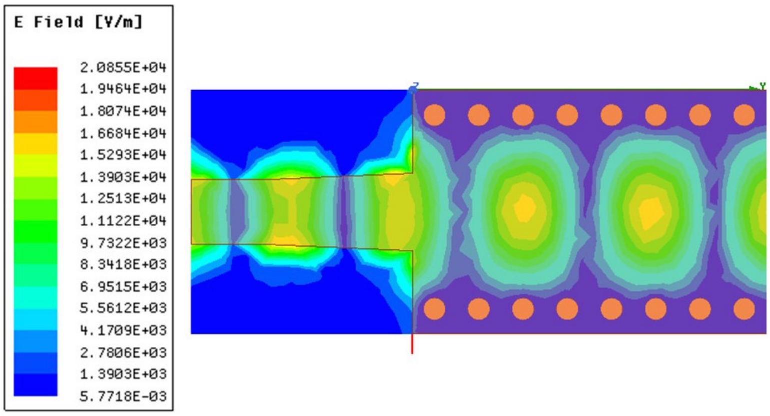

Fig. 4.4: Simulated electric field magnitude in the region of the microstrip transition, at $f = 28$ GHz

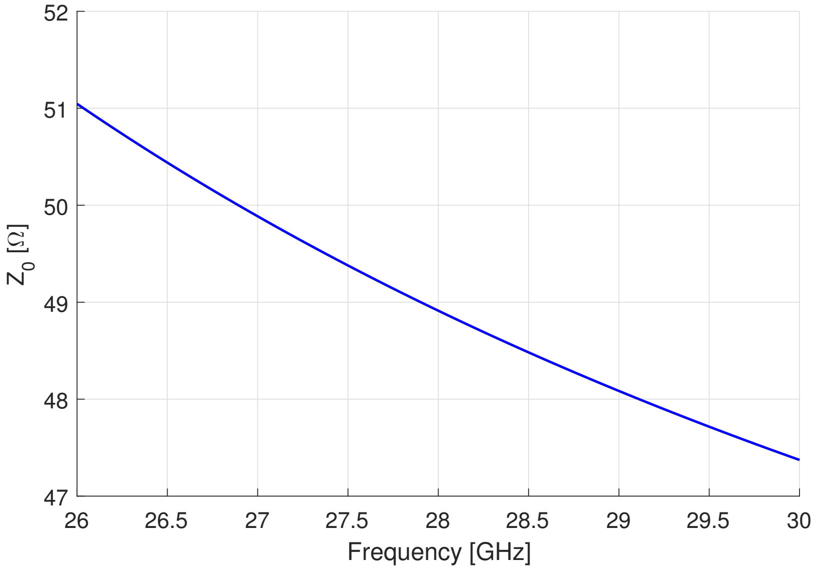

Fig. 4.5: Simulated characteristic impedance Z_0 of the SIW

mode in the SIW. The microstrip transition permits minor reflections also because the SIW was tuned to get a characteristic impedance Z_0 close to the standard value of 50 Ω: the results are confirmed by the plot of Fig. 4.5, where is reported the characteristic impedance of the designed SIW, that demonstrates a trend coherent with (2.11). Notice that, in the band of interest, Z_0 takes values between 47 Ω and 52 Ω, therefore the reflections due to impedance discontinuity are minimized, and the matching is improved. Finally, from these simulations is confirmed the availability of a wide bandwidth, from 26 GHz to 30 GHz, in which the SIW can be adopted as a TL for an LWA concept.

4.2 Leaky Wave Antenna Design

Once having analyzed the underlying waveguiding structure, we can go on with the design of the single cell and the LWA. As discussed in Sec. 3.2, the structure is based on a CRLH transmission line, so the SIW has to be perturbed to introduce Left Handed (LH) contribution, and later be analyzed to retrieve informations about its phase constant $\beta(\omega)$ behaviour. It has been explained in Sec. 3.2.2 that the vias of the SIW provide an LH inductance contribution L_L, so it is fundamental to introduce the necessary C_L contribution. This capacitance can be generated thanks to slots etched on the copper surface, and subsequently tuned thanks to varactor insertion.

In the following sections the analysis steps will be explained, concluding with the design of the frequency scanning LWA and the varactor tuned version.

4.2.1 Design Steps

The analysis of the developed antennas has been conducted following these steps:

- We started with the unit cell design, determining and testing slots geometry, position and dimensions. Through parametric sweeps, cell and slots size have been tuned, observing the effects on resulting simulated scattering parameters and phase constant $\beta(\omega)$. We remember that the unit cell and the complete LWA are both treated as a 2-port network, since they are analyzed as a metamaterial structure, i.e. a CRLH TL, that present an input and an output port.
- The important parameter to consider is the phase constant $\beta(\omega)$, plotted in the dispersion diagram. This can be obtained from scattering parameter S_{11} and S_{21}, and will be examined in order to check the CRLH behaviour of the structure, the balancing of the cell, and to distinguish between RH and LH range. The quantity $\beta(\omega)$ is computed starting from *ABCD* matrix elements [37]:

  $$\cos\left[\beta(\omega)L_{cell}\right] = \frac{A+D}{2} \quad \Rightarrow \quad \beta_L = \beta(\omega)L_{cell} = \cos^{-1}\left(\frac{A+D}{2}\right), \tag{4.1}$$

  where L_{cell} is the length of the unit cell. This expression is derived from microwave periodic filter theory in [37], and also used in [61] in a slightly different form, and in many other scientific papers on this subject. Substituting A and D with the S-parameters, using well known convertion formulas [37], we get:

  $$\beta_L = \cos^{-1}\left(\frac{1 - S_{11}S_{22} + S_{12}S_{21}}{2S_{21}}\right). \tag{4.2}$$

  In the ran simulations, the dispersion diagram has been computed thanks to this expression, starting from simulated S-parameters and taking the real part of (4.2). Notice how (4.2) depends on cell length L_{cell}, only as a scaling factor, that however is a parameter that strongly influences the results, as we will see hereafter.

  Equation (4.2) is clearly an important relation, since it permits to analyze the cell propagation characteristics and to understand how the LWA will behave, indeed we remember the importance of phase constant β in the CRLH LWA design, as discussed in Sec. 3.2. Fundamentally, it is possible to obtain and plot the dispersion diagram, as the one of Fig. 4.6, computed with the explained method and reported as an example.

  Observe how the graph is oriented differently with respect to dispersion diagrams already showed (Fig. 2.5, Fig. 2.6, Fig. 3.2). Indeed, for an easier and faster reading, angular frequency $\omega = 2\pi f$ has been replaced by ordinary frequency f, and placed

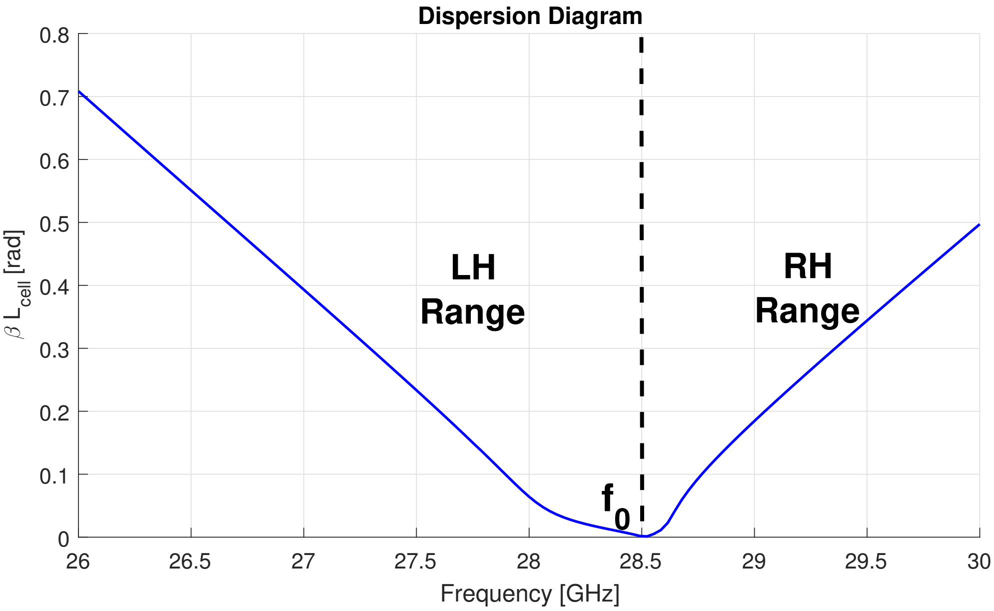

Fig. 4.6: Dispersion diagram example, with highlighted transition frequency f_0 and RH - LH range

on horizontal axis. Phase constant β is placed on vertical axis, and will be always reported as the quantity $\beta_L = \beta(f) \cdot L_{cell}$ [rad].
Since phase constant is computed with the inverse cosine function cos^{-1}, its values will be displayed as all-positive, so we have to bear in mind that LH frequency range will not show a negative β_L, but is related to the graph section with negative slope; conversely RH frequency range presents a positive slope.
The point in which $\beta_L(f) = 0$, as explained, indicates the transition frequency $f_0 = \omega_0/2\pi$. In the depicted dispersion diagram we can notice the distinction between LH and RH range and the transition frequency, related respectively to backward, forward and broadside radiation.
From $\beta_L(f)$ plot, it is possible to deduce if the CRLH structure is balanced, observing the trend near min $[\beta_L(f)]$: if the minimum region is wide, this means that the cell is not balanced, and a band gap is present, conversely if we get a tight minimum and the slope is steep, the band gap closes up and there's an almost seamless transition between LH and RH range.

- Once the unit cell has been studied and simulated, it is replicated N_{cell} times, composing a CRLH TL with periodicity L_{cell}. The structure, completed with the microstrip transition and 2 input ports, works in the radiated wave frequency range, thus will be our LWA. If the unit cell is balanced and shows a concrete CRLH behaviour, it is observed a coherent LWA functioning: this means that the main radiation beam angle θ_{MB} is frequency dependent and it will follow the relation (3.7), that is:

$$\theta_{MB}(f) = \sin^{-1}\left[\frac{\beta(f)}{k_0}\right] = \sin^{-1}\left[\frac{c\,\beta_L(f)}{2\pi f L_{cell}}\right]. \tag{4.3}$$

With (4.3) we can have an idea of the achievable scanning range also directly from the unit cell, without strictly needing the simulation of the entire LWA structure. Indeed, $\theta_{MB}(f)$ can be investigated starting from the elementary cell and then we can confirm the results with the antenna simulation.

- After the design of a frequency scanning LWA that works in the band 26 - 30 GHz, the work has been directed to the varactor tuned LWA. The slots have been adapted to permits the insertion of a diode, adding copper slab and tuning the dimensions. Varactors have been simulated firstly in an ideal manner, later with a more realistic model, creating their equivalent circuit scheme with Keysight ADS software [79] and including it in HFSS. The components have been treated as capacities whose value is swept in a parametric way, in order to simulate a voltage variation.
  For this version of the antenna, similarly to the frequency scanning LWA, the study concentrated on the single cell, investigating β_L at different capacity values, but focusing on a single working frequency. As discussed, varactor diodes modify the constitutive parameters of the CRLH line, therefore they make the LWA electronically tunable, and they enable an elevation beamsteering controlled by bias voltage.

Generally, in both cases, the design consists in the unit cell study, that is the fundamental part, in which the phase constant is tuned to our objective, modifying the cell and observing the effects on β_L. Subsequently, the entire LWA is composed and simulated, to obtain the radiation pattern. The advantage in the first design phase, in terms of efforts and time managing, is that it is not necessary to simulate the entire structure all the time, but the analysis can focus on the elementary cell, knowing that its behaviour will influence the complete LWA.

4.2.2 Frequency Scanning LWA Design

To develop a leaky wave antenna, as discussed above, the critical point is the design of the unit cell. Indeed this single element, with its geometry and dimensions, will strongly influence the overall antenna functionalities. For the initial LWA design, I started from the antennas investigated in [71, 80–82], getting ideas to shape the slots. After trying various configurations, the rectangular slots have been chosen, placed longitudinally along the cell, symmetrically with respect to cell center. Starting from [80], the proposed LWA has been adapted to work in the band of interest, dimensioning and modifying the structure. This

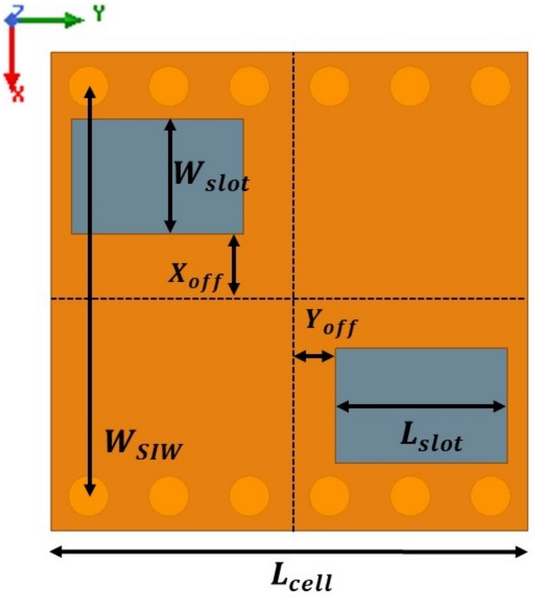

Fig. 4.7: Frequency scanning LWA unit cell

W_{SIW}	L_{slot}	W_{slot}	X_{off}	Y_{off}	L_{cell}
7	3	2	1	0.8	8.3

Tab. 4.2: Cell and slots dimensions of the frequency scanning LWA unit cell of Fig. 4.7 (all measures are in mm)

geometry has been selected because it is flexible and can be easily altered to adapt the cell to the required specification, moreover it is a simple and suitable shape for the subsequent varactor insertion.

Thanks to parametric simulations, cell and slots dimensions have been tuned in order to obtain a balanced dispersion diagram, centred in the frequencies of interest, and with transition frequency $f_0 \approx 28$ GHz. The modifications have been conducted operating on SIW width (W_{SIW}), on the slot dimensions (L_{slot}, W_{slot}), and on the slot offset (X_{off}, Y_{off}). These features are indeed the elements that cause the parasitic capacitance C_L, that permits the CRLH behaviour of the structure, thus modifying them will influence the $\beta_L(f)$ shape and particularly the f_0 position. We will observe these results in Chap. 5. Finally, the slots are made as large as possible, to enhance radiation efficiency.

The optimized slots dimensions are reported in Tab 4.2, and the elementary cell is depicted in Fig. 4.7. The single cell is then replicated N_{cell} times with L_{cell} periodicity, in order to compose the complete LWA, reported in Fig. 4.8 in the case $N_{cell} = 8$. The peak gain dependence on cell number is demonstrated and illustrated in Chap. 5, as well as frequency scanning capability, coherent with $\beta_L(f)$ shape.

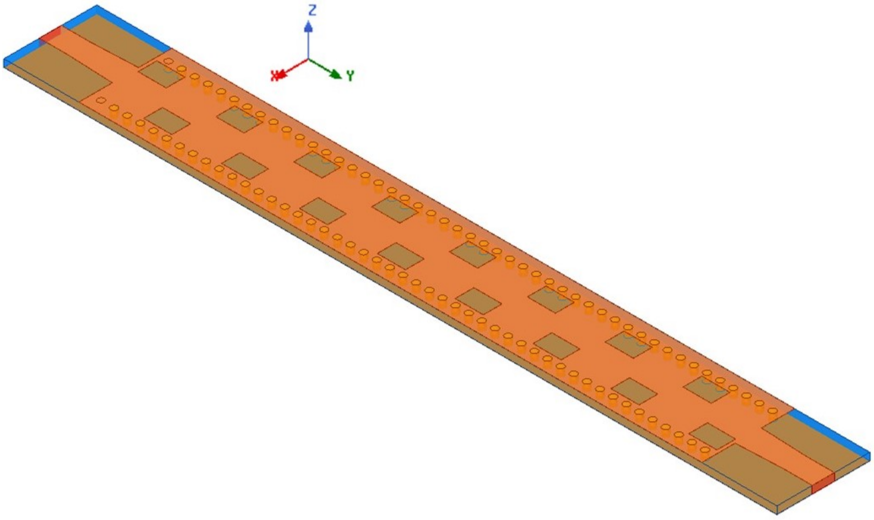

Fig. 4.8: Frequency scanning LWA composed by $N_{cell} = 8$ unit cells

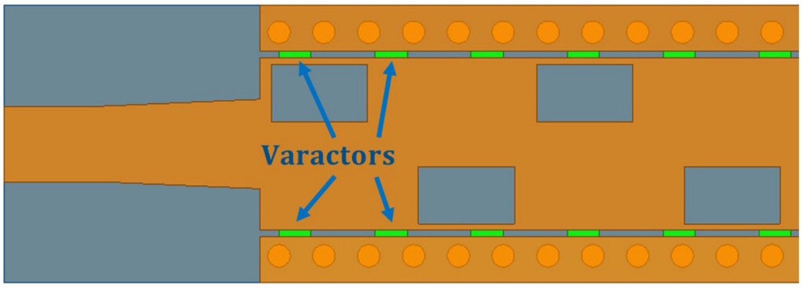

Fig. 4.9: Tentative design of an LWA with varactor-controlled cutoff frequency

4.2.3 Varactor Tuned LWA Design

Once having studied and optimized the "simple" LWA, the effort shifted to the application of the varactors to the elementary cell. We remember (Sec. 3.2.1) that these components are necessary to modify the LH capacitance C_L, in order to tune phase constant β_L through variation of the bias voltage applied to the diodes. In this way, working at a fixed frequency, we can shift β_L from negative to positive values, thus controlling the main beam direction θ_{MB} (see Eq. 3.10 and 3.7).

At high frequencies range the choice of the varactor is not easy, since too high capacitance values result approximately as a short circuit, that won't produce the desired effects but would only degrade signal propagation. For these reasons, after some tests, the choice has been directed towards diodes specifically designed to work at mmWave frequencies, with junction capacitance low enough, in the order of $0.1 \sim 2$ pF. Moreover, also dimensions determined the varactor selection: since slots size is 2 x 3 mm, it is not possible to install bulky components, but we look for highly compact varactors. To decide how to position

L_{cell}	L_{plate}	X_{off}	W_{var}	L_{var}	$W1_{plate}$	$W2_{plate}$	pl_{off}
8.3	1.5	0.7	0.3	0.7	0.6	0.3	1.35

Tab. 4.3: Optimized dimensions of the varactor tuned LWA unit cell of Fig. 4.10 (all measures are in mm)

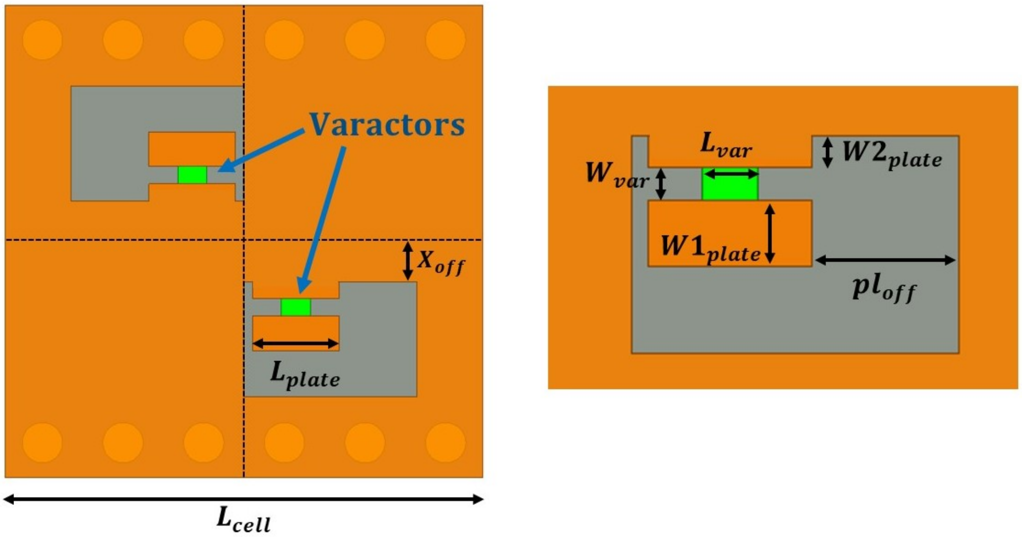

Fig. 4.10: Varactor tuned LWA unit cell, with zoom on the slot part

the diodes in the cell, various configurations have been tried, through geometries and dimensions modification, in order to obtain a smooth variation of β_L without degrading the performances of the complete LWA, and also staying on feasible capacitance values.

Initially, as investigated in [83], the slots geometry has been maintained, and along the entire LWA length have been added two slits, on which insert the varactors, as depicted in Fig. 4.9. In this way, a variation of the capacity results in a shift of the SIW cutoff frequency f_{cut}, since this modification is analogous to the waveguide width change. Varying f_{cut}, also β_L is shifted in frequency, thus it would be possible to control θ_{MB} through varactors tuning. However, after some simulations, the design has been discarded: the slits had to be overly tight, making difficult the mechanical realization and the positioning of the diodes, that moreover had to be too much numerous, leading to costs and feeding issues.

Afterwards, we focused on the possibility of varactors insertion directly in the slots. Trying some configurations, it was evident that we needed to add some copper slabs inside of the slots, to enhance varactor effectiveness and to ease the feeding network. The slabs have been dimensioned and optimized, examining which design was better to obtain a good β_L variation and field propagation. In many cases indeed, the configuration and the capacitance values led to a total degradation of the EM field, that made the antenna ineffective: the

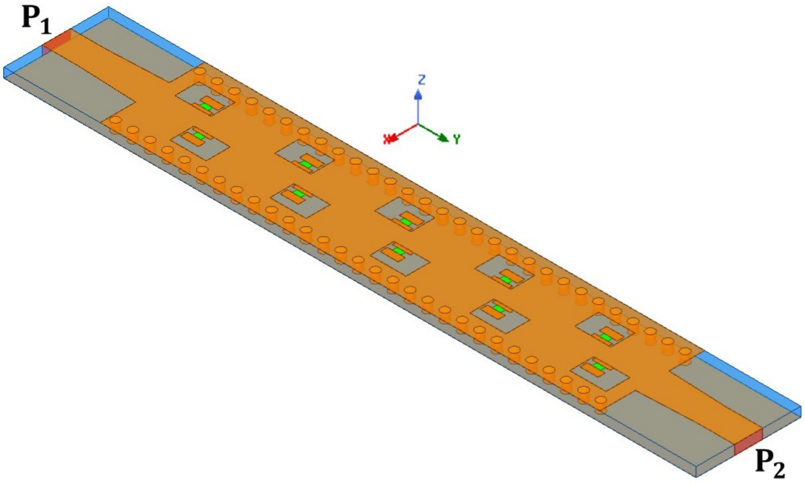

Fig. 4.11: Varactor tuned LWA composed by $N_{cell} = 5$ unit cells

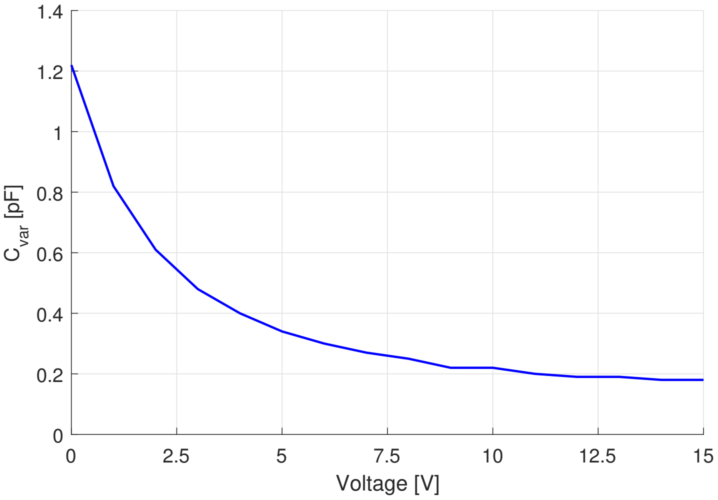

Fig. 4.12: Varactor capacity C_{var} dependence on bias voltage V (Macom MA46H120 component)

overall dimensioning is critical, since at mmWave frequencies also fractions of millimetre can result in significative performance variations. The final design is illustrated in Fig. 4.10, with relative dimensions in Tab. 4.3, remembering that the slots maintain the same dimensions as before. In Fig. 4.11 is depicted the complete varactor tuned LWA composed by 5 unit cells, in which we highlighted the 2 input ports, since it will be showed how we can enhance the beamsteering range using alternatively port 1 or port 2 as input.

As we can see, a symmetry has been maintained with respect to cell axes, and there is one varactor per slot. The design has been optimized to work at $f_w = 26.5$ GHz, and the varactors are tuned all together to the same capacitance value, that varies from 0.18 pF to 1.2 pF, varying the voltage in the range [0, 15] V. The results will be analyzed in Chap. 5, and the followed design steps are those illustrated in Sec. 4.2.1, particularly focusing on tuning the diodes capacitance.

The chosen varactor is the Macom MA46H120 [84, 85], commercially available, that offers a good compromise between costs, size (it measures 0.65 x 0.35 x 0.15 mm), and capacity range, that is suitable for our application. It was initially simulated as an ideal capacity, and subsequently its equivalent circuit model was designed with ADS software [79], to obtain data about its S-parameters, and utilize them in HFSS in order to simulate the LWA accounting also the varactor losses and create a more realistic model. In Fig. 4.13 we can observe the equivalent circuit model, and in Fig. 4.12 the graph shows how the varactor capacity C_{var} varies with bias voltage.

As already outlined, the slots have been modified with a metal slab, that helped with the varactor insertion and its voltage feeding. A possible feeding line has been designed, that is clearly needed to control the varactors capacity through voltage variation. The varactor diode is a device that works with a reverse applied voltage, therefore observing Fig. 4.14 we notice that the cathode is placed on the metal slab, and the anode on the upper copper plate of the SIW. The slot design has the advantage of separating the two pin, that otherwise would be harder, since at DC voltage all the waveguide is at the same potential. In this way, we can consider all the structure as a *ground*, and feed the metal slabs with a positive voltage, providing the needed potential difference that enables the varactor function.

Regarding separately both the slots, we can add a pin that connect the copper plate to an underlying feeding line that cover all the LWA length and brings the DC signal to the varactors cathode. Between the pin and the line should be placed an inductance that works as an RF choke, i.e. a component that blocks higher frequencies, while passing DC signal. The line has to be separated from the SIW, for this we can use a coplanar waveguide (CPW) structure. This configuration clearly will break the SIW continuity, thus altering its guiding characteristic: to avoid this problem, the overall system has to be accurately designed and simulated before its implementation. A possible solution to maintain the performances unchanged could be the addition of some metal *bridges* that connect the two plates separated by the CPW.

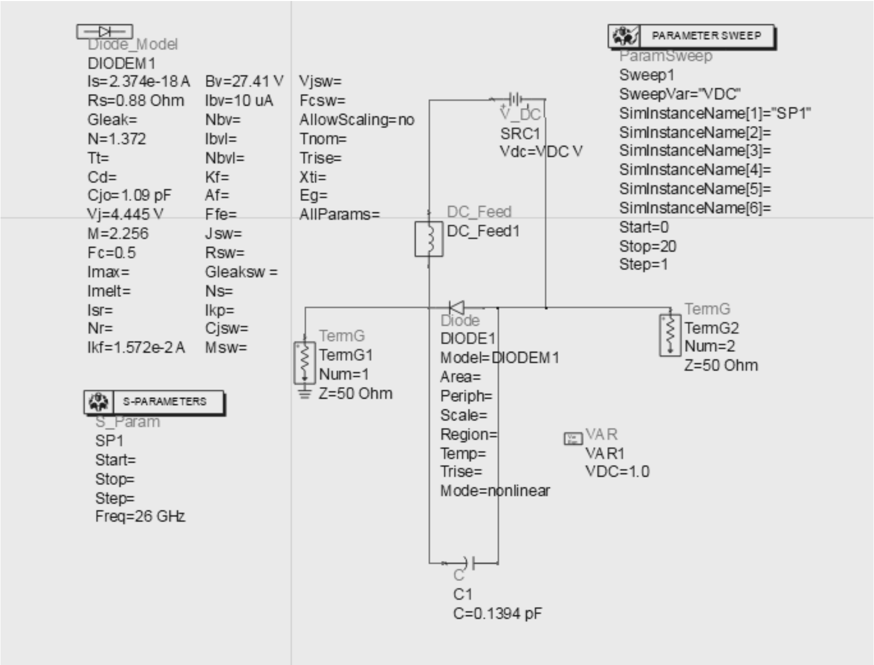

Diode_Model
DIODEM1
Is=2.374e-18 A
Rs=0.88 Ohm
Gleak=
N=1.372
Tt=
Cd=
Cjo=1.09 pF
Vj=4.445 V
M=2.256
Fc=0.5
Imax=
Imelt=
Isr=
Nr=
Ikf=1.572e-2 A
Bv=27.41 V
Ibv=10 uA
Nbv=
Ibvl=
Nbvl=
Kf=
Af=
Ffe=
Jsw=
Rsw=
Gleaksw =
Ns=
Ikp=
Cjsw=
Msw=
Vjsw=
Fcsw=
AllowScaling=no
Tnom=
Trise=
Xti=
Eg=
AllParams=

S-PARAMETERS
S_Param
SP1
Start=
Stop=
Step=
Freq=26 GHz

TermG
TermG1
Num=1
Z=50 Ohm

V_DC
SRC1
Vdc=VDC V

DC_Feed
DC_Feed1

Diode
DIODE1
Model=DIODEM1
Area=
Periph=
Scale=
Region=
Temp=
Trise=
Mode=nonlinear

C
C1
C=0.1394 pF

PARAMETER SWEEP
ParamSweep
Sweep1
SweepVar="VDC"
SimInstanceName[1]="SP1"
SimInstanceName[2]=
SimInstanceName[3]=
SimInstanceName[4]=
SimInstanceName[5]=
SimInstanceName[6]=
Start=0
Stop=20
Step=1

TermG
TermG2
Num=2
Z=50 Ohm

VAR
VAR1
VDC=1.0

Fig. 4.13: Equivalent circuit model of the Macom MA46H120 varactor

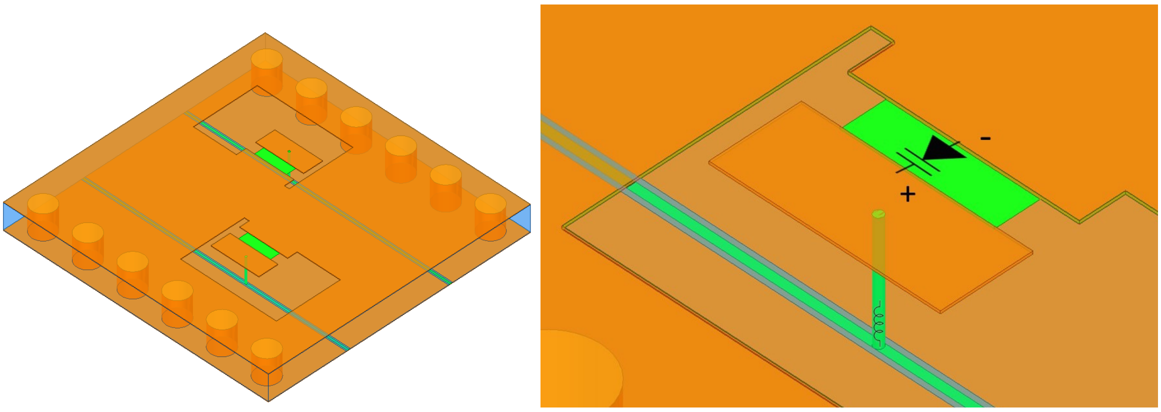

(a) Unit cell view **(b)** Zoom on the slot region

Fig. 4.14: Feeding network for the varactor diodes

Chapter 5

LWAs Simulation Results

The design of both the frequency scanning LWA and the varactor tuned LWA was optimized observing the results, mainly in terms of realized gain, scattering parameters, scanning range, radiation efficiency. Through cell parameters tuning, the main goal was to achieve a good scanning range, and secondly to maximize the gain, that is however influenced by the number of elementary cells, as we will see.

Considering that has not been possible to implement a prototype, the work has been focused on the study of the achievable performances of both the designed antennas, mostly analyzing which cell features modify the phase constant β_L, consequently the main beam angle θ_{MB}, and how the peak gain can change. All the dimensions, the geometries, and particularly the varactor placement, have been studied always bearing in mind the practical application, so they was tuned in a way that a future realization of the system is feasible and doable in the short time, to hereafter conduct real tests.

All the simulations have been ran using Ansys HFSS [36], in combination with ADS software [79] for the varactor model simulation, using a driven modal setting, a 3D model and a circuital scheme, in collaboration with Adant Technologies.

The following chapter presents the obtained results regarding the frequency scanning LWA, showing the radiation diagram, the performances of the final design, and analyzing some aspects of the unit cell. Subsequently, we pass to the varactor tuned LWA, investigating its voltage controlled main beam angle at a fixed frequency. Various features of this antenna will be analyzed, examining its pros and cons, trade-off, and overall performances, considering the initial requirements reported in Chap. 4.

5.1 Frequency Scanning LWA Results

As already discussed, this version of the antenna presents the classic characteristics of a metamaterial based LWA, that is a main beam angle that varies with the frequency sweep,

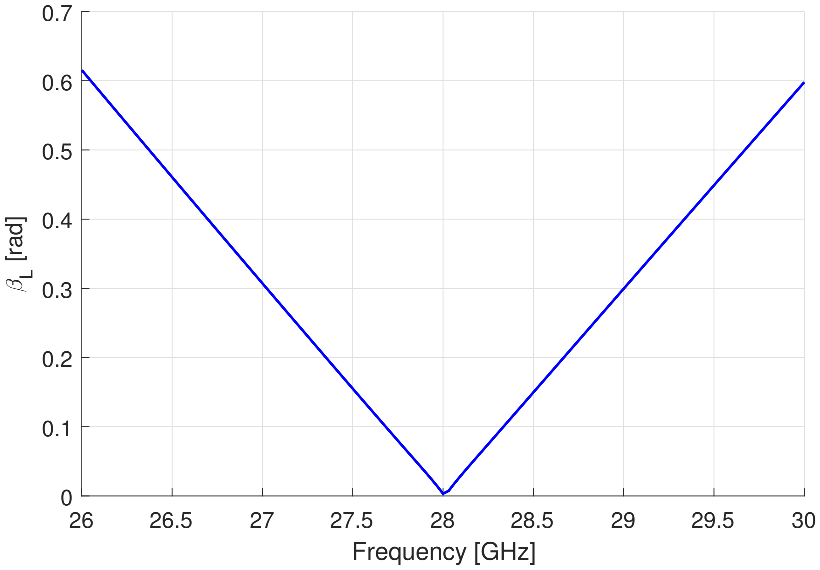

Fig. 5.1: Dispersion diagram of the frequency scanning LWA unit cell depicted in Fig. 4.7

from backfire direction, through broadside, towards endfire. The reported results are relative to the final design of the antenna, with unit cell and complete LWA depicted in Fig. 4.7 and Fig. 4.8.

Firstly, the fundamental cell analysis showed the phase constant $\beta_L(f)$ of Fig. 5.1, obtained from S-parameters with (4.2). In the dispersion diagram we can observe that there is a tight minimum at $f_0 \approx 28$ GHz, that clearly separates between RH ($f > f_0$) and LH ($f < f_0$) range: the CRLH structure of the fundamental cell results well balanced, therefore there is no band gap. This characteristic permits a broadside radiation and a quite constant gain through all the range of scanning, without beam degradation. Tuning the cell and SIW dimensions, we managed to fix the transition frequency f_0 at 28 GHz, central frequency of the band of interest (26 GHz to 30 GHz).

Thanks to (4.3) it is possible to get the main beam direction angle $\theta_{MB}(f)$, plotted in Fig. 5.2. We remember that this formula gives as result the angle relative to the longitudinal axis of the antenna, in our case is the angle in the radiation pattern in the elevation (yz) plane (compare with Fig. 4.8).
Considering that the frequencies $f < f_0$ belong to LH range, and therefore both β_L and θ_{MB} are to be considered negative, we can notice that the plot indicates a beam scanning from $\theta_{MB} = -8°$ at $f_1 = 26$ GHz, to $\theta_{MB} = +6.5°$ at $f_2 = 30$ GHz, with a broadside radiation at central frequency $f_0 = 28$ GHz. Notice that, observing Fig. 5.2, a gradual frequency sweep will cover all the beam directions included between -8° and +6.5°, and, clearly, widening the frequency range, also the scanning range will increase.

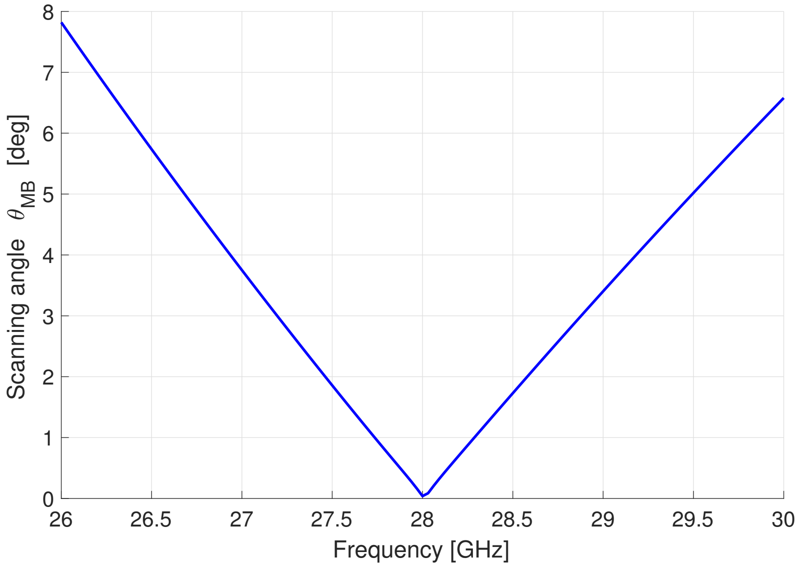

Fig. 5.2: Scanning angle $\theta_{MB}(f)$ of the frequency scanning LWA, computed with (4.3)

These relations are confirmed by the radiation patterns. The LWA is composed by a sequence of N_{cell} cells, and from its simulation we observe a radiation diagram coherent with the results of the unit cell. In Fig. 5.3 is reported the gain pattern in the case $N_{cell} = 8$, relative to elevation (yz) plane. The figure shows the *realized* gain at frequencies $f_1 = 26$ GHz, $f_0 = 28$ GHz, $f_2 = 30$ GHz, whose main beam points approximately at -7°, 0°, and +6°. Notice how the indications given from the θ_{MB} plot (Fig. 5.2) are quite exact with respect to the simulated gain, confirming the possibility of concentrating the effort on the study and optimization of the single cell, knowing that then its behaviour will reflect coherently on the LWA. Indeed, the relation between dispersion diagram $\beta_L(f)$ and main beam direction is confirmed, that is a radiation toward backfire when $\beta_L < 0$ (LH range), toward endfire when $\beta_L > 0$ (RH range), and broadside radiation when $\beta_L = 0$.

The main lobe is narrow and highly directive, as desired, and the radiation diagram is quite accordant to that expected from an LWA: it presents a good directivity and high side lobes, that however stay below 0 dBi. Moreover, the simulated peak gain increases through the scan, together with the frequency increasing, common characteristic of metamaterial LWAs (observed also in [71]). The good broadside radiation confirms the balancing of the CLRH structure. Resuming, in the case $N_{cell} = 8$, the simulated peak gains G_{peak}, main beam angles θ_{MB}, and radiation efficiencies η are:

- $f_1 = 26$ GHz: $G_{peak} = 9.8$ dBi, $\theta_{MB} = -7°$, $\eta = 83\%$;
- $f_0 = 28$ GHz: $G_{peak} = 10$ dBi, $\theta_{MB} = 0°$, $\eta = 83\%$;
- $f_2 = 30$ GHz: $G_{peak} = 10.61$ dBi, $\theta_{MB} = +6°$, $\eta = 86\%$.

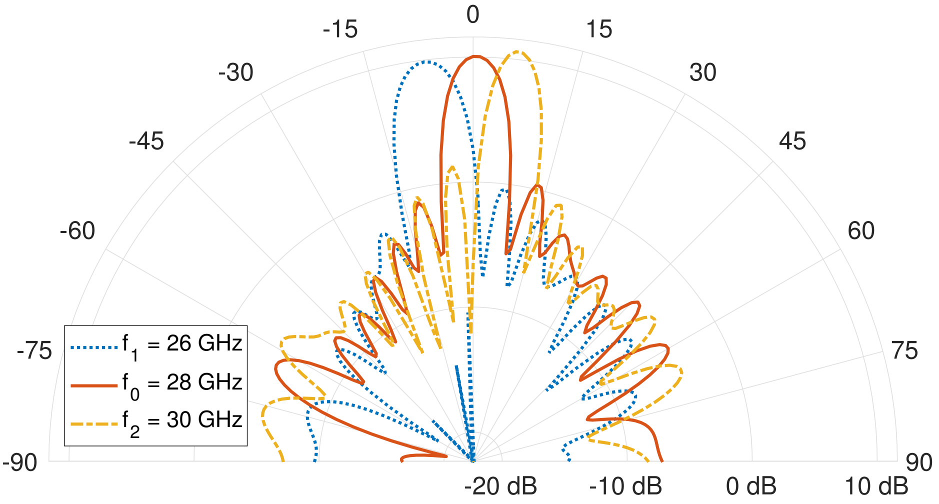

Fig. 5.3: Simulated radiation patterns in the elevation (yz) plane of the frequency scanning LWA of Fig. 4.8, with $N_{cell} = 8$ and at frequencies $f_1 = 26$ GHz, $f_0 = 28$ GHz, $f_2 = 30$ GHz

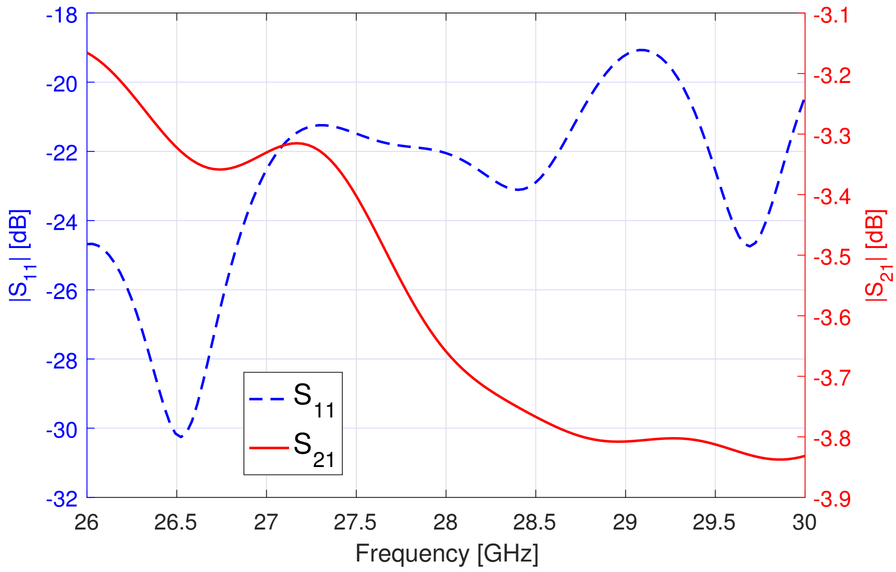

Fig. 5.4: Simulated S-parameters of the frequency scanning LWA, in the case $N_{cell} = 8$

Furthermore, also the scattering parameters give significative informations: in Fig. 5.4 we can observe the magnitude of S_{11} and S_{21}, remembering that an LWA is a two port device. Notice that the S_{11} is always below -18 dB, confirming the good impedance matching of the waveguide and the microstrip transition, and therefore the absence of major reflections, in this way the power insertion is maximized. The S_{21} parameter instead shows how much power gets to port 2: it would be better if it was even lower, indeed in an LWA, a lower S_{21} means that most of the power is radiated and partly dissipated by the losses mechanisms. Overall, the structure losses are not predominant, bearing in mind also the high frequency

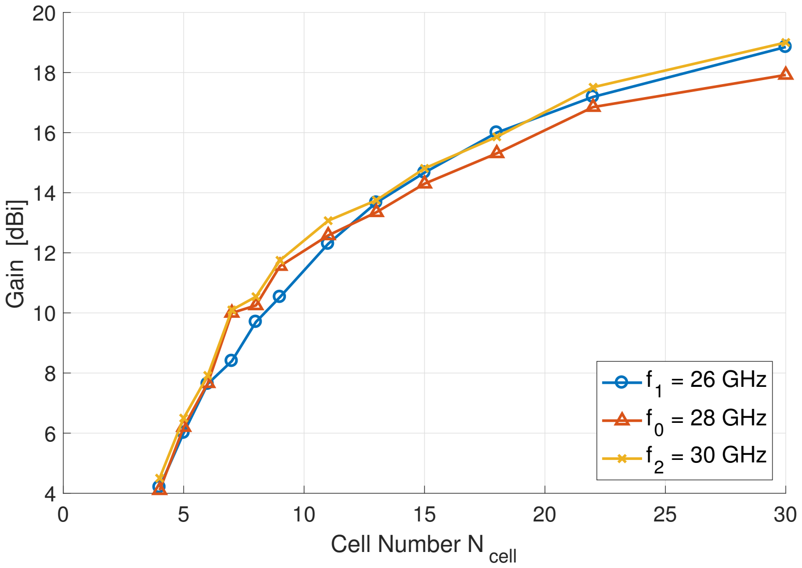

Fig. 5.5: Variation of the simulated peak gain in dependence of N_{cell}, at frequencies $f_1 = 26$ GHz, $f_0 = 28$ GHz, $f_2 = 30$ GHz, for the frequency scanning LWA

range, and indeed the radiation efficiency results about 83 - 86%.

Another interesting characteristic, as examined in Sec. 3.1, is the directivity dependence on the length of the LWA: increasing the number of cells, the gain should rise, since a longer structure permits the irradiation of a larger power fraction. In this way, we obtain a higher peak gain and, related to this, a higher directivity and a narrower main beam. This relation is confirmed by the results obtained simulating various LWAs, varying the number of cells, N_{cell}, from 4 to 30, and observing the peak gain and the HPBW. In Fig. 5.5 is depicted the variation of the peak gain with the N_{cell} parameter, at frequencies $f_1 = 26$ GHz, $f_0 = 28$ GHz, $f_3 = 30$ GHz (and therefore respectively at different main beam angles).
Notice the coherence of this result with the reported theory. We observe that the gain behaviour is similar for all the three frequencies: it increases rapidly when $N_{cell} < 10$, and then it tends approximately to 20 dBi, limit value, dictated mainly by the transmission capacity of the waveguide. Clearly we can not make the antenna indiscriminately big, so a good compromise between gain and compactness may be the value $N_{cell} = 15$, which guarantees a good mean peak gain of 14.5 dBi, and makes the total length of LWA and microstrip transition equal to 130 mm.

To visualize this result, the radiation pattern in the case $N_{cell} = 15$ is reported in Fig. 5.6, for the frequency $f_0 = 28$ GHz (broadside radiation). Notice the narrower main beam, associated with a higher peak gain, and a lower HPBW, that is approximately 4.5°, while in the case $N_{cell} = 8$ it measures 9°. We can observe also an increase of the Side Lobe Level (SLL) and of the back lobe, in which a non negligible part of the energy is wasted. A

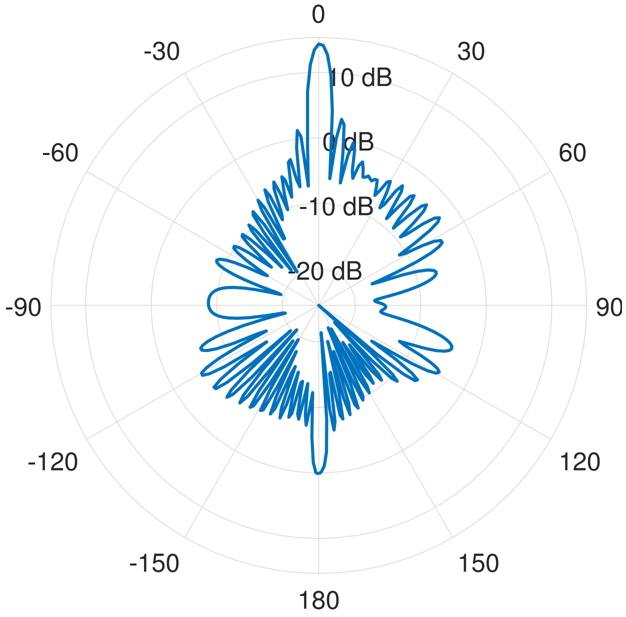

Fig. 5.6: Simulated radiation pattern in the elevation (yz) plane of the frequency scanning LWA, with $N_{cell} = 15$, at frequency $f_0 = 28$ GHz. Notice the higher gain, the narrower main beam, and the higher side lobe level, with respect to the patterns of Fig. 5.3

solution to minimize the back lobe is to enlarge the ground plane, but this would augment in particular the lateral total size of the antenna, leading to complications in the realization of an array. Another possibility is to apply a taper to cell geometries, as investigated in [86], that can help in shaping the main beam and decreasing the SLL.

5.1.1 Unit Cell Parameters Variations

As already discussed and demonstrated, the fundamental cell determines the radiation characteristics of the complete LWA. Parametric simulations have been conducted to investigate how the cell features and slot dimensions produce modifications in the phase constant β_L, that is the main quantity that influences the main beam angle. In this way it is possible to know on which parameters we have to operate if we want to obtain a desired shape of β_L or a particular transition frequency f_0.

- **SIW width, $\mathbf{W_{SIW}}$**: It has been explained in Sec. 2.1.1 how the cutoff frequency f_{cut} of the SIW structure depends principally on the parameter W_{SIW}, similarly to the case of a rectangular waveguide. Widening the SIW, i.e. increasing W_{SIW}, the cutoff frequency decreases, and vice versa. Changing the quantity f_{cut} means to shift in frequency all the SIW-related behaviours, and in particular also the phase constant β_L. We confirm this relation observing Fig. 5.7, where is plotted the dispersion diagram relative to different values of W_{SIW}, for a cell as the one depicted in Fig. 4.7. Notice

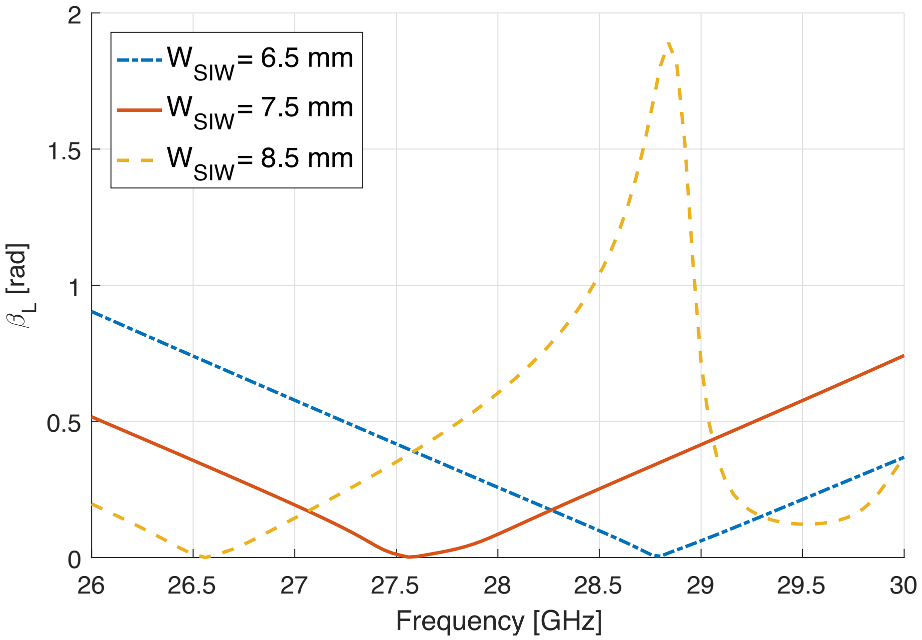

Fig. 5.7: Effect of the SIW width variation on the phase constant β_L of the frequency scanning LWA unit cell (Fig. 4.7), in the cases $W_{SIW} = 6.5$ mm, $W_{SIW} = 7.5$ mm, $W_{SIW} = 8.5$ mm.

that corresponding to the increase of W_{SIW}, the β_L shape remains quite unaltered, but it is totally shifted to lower frequencies, coherently with the f_{cut} decreasing. However this variation has to be done carefully, indeed in the case $W_{SIW} = 8.5$ mm we observe a significant modification in the β_L, particularly for higher frequencies: a too low f_{cut} (relative to TE_{10} mode) lead to unwanted propagation of higher modes that result above their cutoff frequencies. In this way, the propagation becomes multi-modal, and the guiding and radiating performance are degraded.

- **Cell length, L_{cell}**: This is an important parameter too, since it modifies the overall phase delay of the propagating field, proportional to $\beta \cdot L_{cell}$. In particular we observe also in this case a frequency shift of the dispersion diagram: in Fig. 5.8 we notice that increasing the cell length, the phase constant moves to lower frequencies.
- **Lateral and longitudinal offsets, X_{off} and Y_{off}**: Also these quantities demonstrated influences on the β_L behaviour, but in a less significative manner. However, they have been used in the cell tuning, in particular to adjust how the slot interacts with the electric field, since the offsets modify the slot position relatively to the maximum of the field.
- **Slot width and length, W_{slot} and L_{slot}**: The slots are clearly important, since they're the features that introduce the parasitic capacitance C_L and therefore they enable the CRLH behaviour of the structure. Their dimensions and positions determine the C_L value, that is present in the β expression (2.20), and consequently they influence

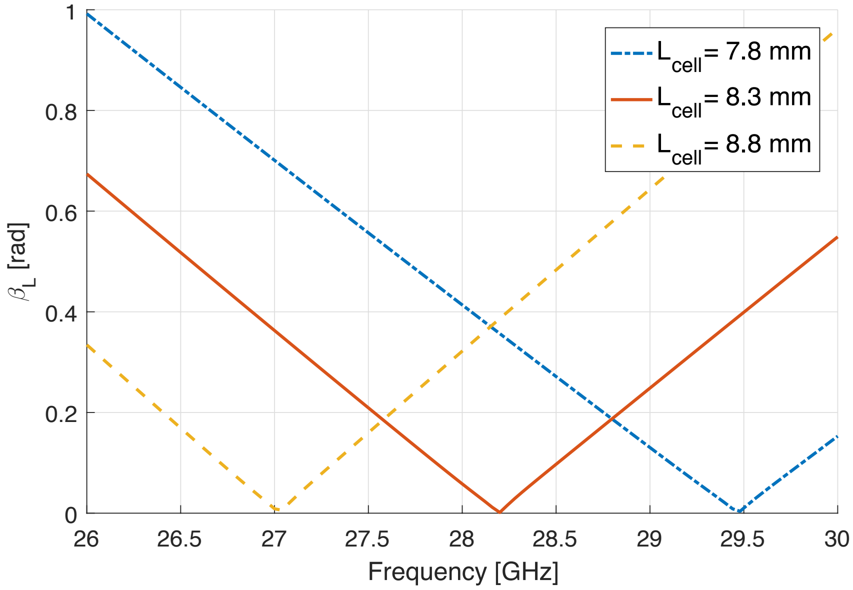

Fig. 5.8: Effect of the cell length variation on the phase constant β_L of the frequency scanning LWA unit cell (Fig. 4.7), in the cases $L_{cell} = 7.8$ mm, $L_{cell} = 8.3$ mm, $L_{cell} = 8.8$ mm.

the transition frequency f_0 (2.21). Therefore, they were the main parameters to be tuned to modify the β_L shape and to fix f_0 at 28 GHz. In particular, an increase of C_L results in a lower transition frequency, since in the case of a balanced cell we have $f_0 = 1/(2\pi\sqrt{L_R C_L})$. In the conducted simulations, we get the results depicted in Fig. 5.9, where we can see how W_{slot} and L_{slot} change the phase constant: mainly the slot width modifies the position and the shape of the minimum of β_L. Overall, we can say that the increase of the slot area lower the transition frequency f_0.

All these parameters have been tuned to obtain the final design depicted in Fig. 4.7, and the dispersion diagram of Fig. 5.1. Besides the possibility of obtaining a phase constant β_L with tight minimum and thus closing the band-gap, it's interesting to observe how it is possible to shift the transition frequency f_0, that is the frequency of broadside radiation. Since the band of interest and the central frequency are not strictly defined yet (see Sec. 1.2), mostly because of the absence of a defined 5G standard, it is useful to dispose of a flexible system, easily adaptable and modifiable depending on the needs. Therefore the designed antenna, with slight changes in the development phase, permits to be centred in all the frequencies between 26 GHz and 30 GHz, as illustrated, thanks to both the cell tuning and the SIW structure that provides a wide impedance matching.

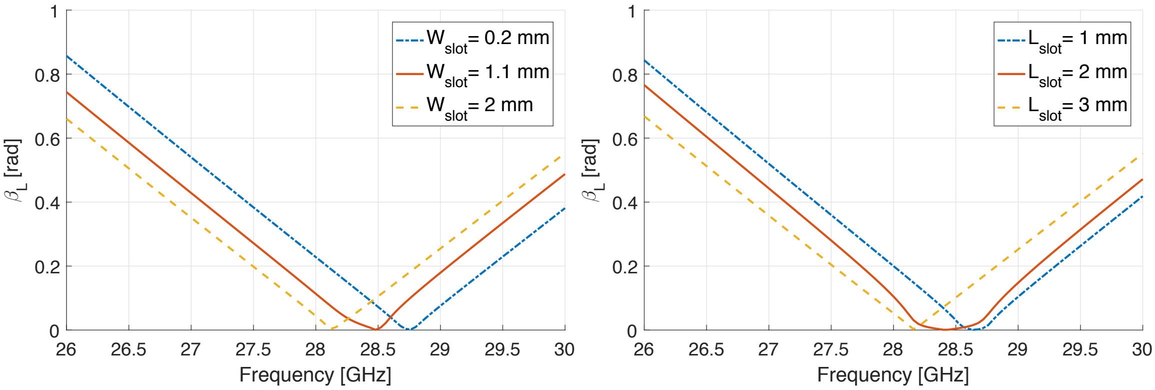

(a) W_{slot} variation. **(b)** L_{slot} variation.

Fig. 5.9: Effect of the slots width and length variation on the phase constant β_L of the frequency scanning LWA unit cell (Fig. 4.7), in the cases $W_{slot} = 0.2$ mm, $W_{slot} = 1.1$ mm, $W_{slot} = 2$ mm; and $L_{slot} = 1$ mm, $L_{slot} = 2$ mm, $L_{slot} = 3$ mm.

5.2 Varactor Tuned LWA Results

As explained in Sec. 4.2.3, after the optimization of the frequency scanning LWA, we continued investigating how to place the varactors. The final design is showed in Fig. 4.10 and Fig. 4.11. We remember that, also in this case, N_{cell} is a variable parameter, that was tuned to optimize the LWA in terms of peak gain and HPBW. The varactors are inserted in the unit cell slots, and their capacity C_{var} is electronically tuned to the same value along the entire LWA. In this way, through a voltage variation, we are able to modify the phase constant β and thus the main beam angle θ_{MB}, at a fixed frequency, as discussed in Sec. 3.2.1.

A beamsteering in the elevation plane can be performed, with an overall good peak gain and at high frequency range, using a relatively simple structure, mostly because we avoid using phase shifters. These components are indeed the first choice for the implementation of a phased array for beamsteering application, but they are very lossy, particularly at mmWave frequencies, and they complicate the design of the feeding network. Varactors are therefore a good alternative, that minimize the power losses, as investigated for example in [61]. Moreover, a non negligible factors are the cost issues, mostly expecting a practical application and the development of a commercial product. In a company point of view, the components cost is important: for this reason the varactor solution has been selected, since most of the phase shifters suitable for mmWave applications have important costs.

Scanning Range: As we have done in the previous section, the first quantity to be analyzed is the phase constant β_L, but this time in dependence of the voltage V. We remember the varactor capacity variation with respect to bias voltage V, reported in Fig. 4.12: it changes from $C_{var} = 1.2$ pF at $V = 0$ V, to $C_{var} = 0.18$ pF at $V = 15$ V, noticing how the

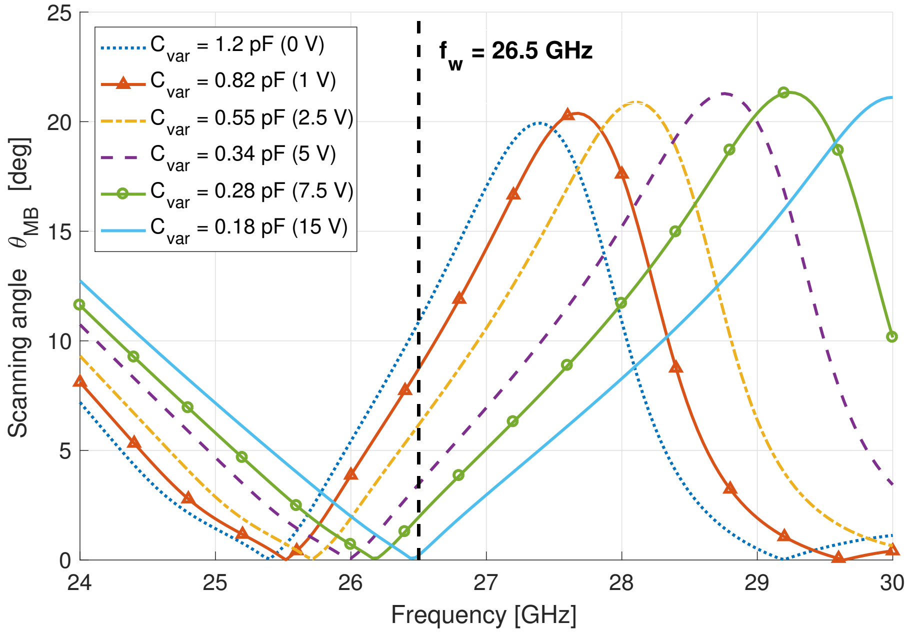

Fig. 5.10: Scanning angle θ_{MB} computed with (4.3) from simulated phase constant β_L of the varactor tuned LWA. The various traces of θ_{MB} correspond to different varactor capacity values, controlled by bias voltage variation. Notice in particular the values taken at $f_w = 26.5$ GHz.

trend is not linear, but negative exponential-like. We can examine directly the quantity θ_{MB} obtained with (4.3).

In Fig. 5.10 is reported the scanning angle variation corresponding to various bias voltage values, and therefore different C_{var} values. We notice how the θ_{MB} graph is shifted toward higher frequencies as the voltage increases (and C_{var} decreases). Observe in particular the values of θ_{MB} at the fixed frequency $f_w = 26.5$ GHz, chosen as working frequency: the design has been tuned in order to obtain a $\beta_L = 0$ (and consequently $\theta_{MB} = 0°$) when $V = \max(V)$ and $C_{var} = \min(C_{var})$. In this way we can have a sweep of the angle from 0° to $\max(\theta_{MB}) \approx 11°$, and indeed since at $f_w = 26.5$ GHz all the β_L curves belong to RH range, the beamsteering will be entirely in the forward radiation region.

This configuration has been chosen because the LWA can be power-fed from both the ports P1 and P2 (see Fig. 4.11). Since the structure is symmetric, the phase delay and the scanning angle are to be considered relatively to the input port, therefore, using the same reference axis, if we feed port 1 and results $\theta_{MB} = \theta_0 > 0$, with the same configuration but using port 2 as power input, we will have a main beam directed toward the symmetric negative angle $-\theta_0 < 0$. This relation will be evident lately, when the simulated radiation patterns will be shown. This system is feasible, although it requires a slightly more complicated feeding network, but it presents the advantage of maximizing the scanning range.

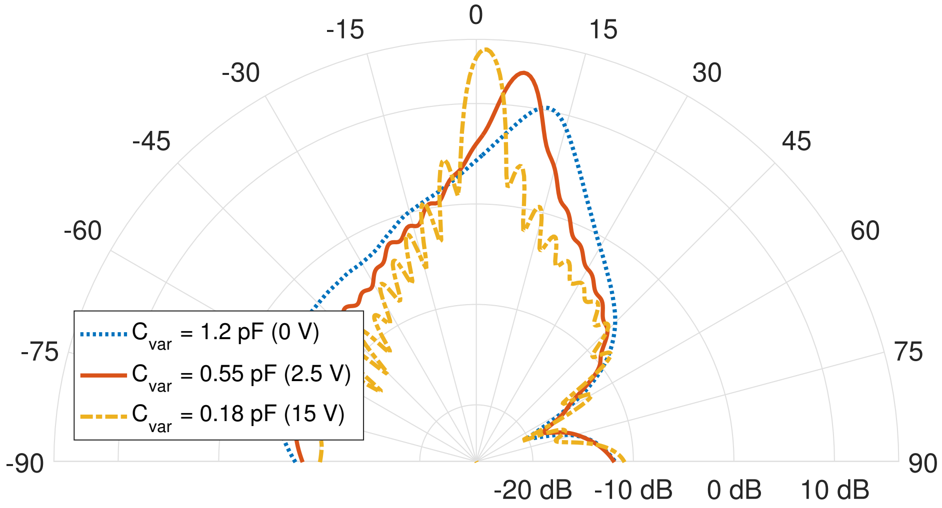

Fig. 5.11: Radiation patterns of the varactor tuned LWA of Fig. 4.11 at frequency $f_w = 26.5$ GHz and with $N_{cell} = 15$. The three traces corresponds to three different capacity (voltage) values, showing how the beam can be steered.

Alternatively, the antenna can be tuned by shifting f_w or modifying the fundamental cell, in order to utilize a single input port and perform a beamsteering with an angle that varies from negative to positive values, but halving the total scanning.

Gain Pattern: We consider now the gain pattern of the LWA. In Fig. 5.11 are reported three radiation patterns relative to three different voltage values, at frequency $f_w = 26.5$ GHz and with $N_{cell} = 15$. Notice the coherence between Fig. 5.11 and the graph in Fig. 5.10: the values of θ_{MB} resulting with (4.3), evaluated starting from the phase constant β_L, can be inspected in the radiation pattern. When $V = 15$ V and $C_{var} = 0.18$ pF, the main beam points toward broadside, whereas if $V = 0$ V and $C_{var} = 1.2$ pF, the main beam points at $\theta_{MB} \approx 12°$. Therefore, increasing the varactor bias voltage from 0 V to 15 V, we will gradually sweep the angle from 12° to 0°.

The gain values are quite good, but they vary from broadside radiation towards θ_{max}, decreasing from 15 dBi to 10 dBi. We observe indeed how the beam corresponding to $V = 0$ V and $C_{var} = 1.2$ pF is degraded with respect to the case $V = 15$ V and $C_{var} = 0.18$ pF: it is wider and the power is not precisely radiated, thus it presents a lower peak gain and a larger HPBW. This characteristic appears gradually when sweeping the angle from 0° to θ_{max}, and it happens in correspondence with higher capacity values, that clearly worsen the EM propagation and cause the beam degradation.

S-Parameters: The outlined characteristics can be confirmed also observing the scattering parameters of the complete antenna, reported in Fig. 5.12 and Fig. 5.13 at different voltage

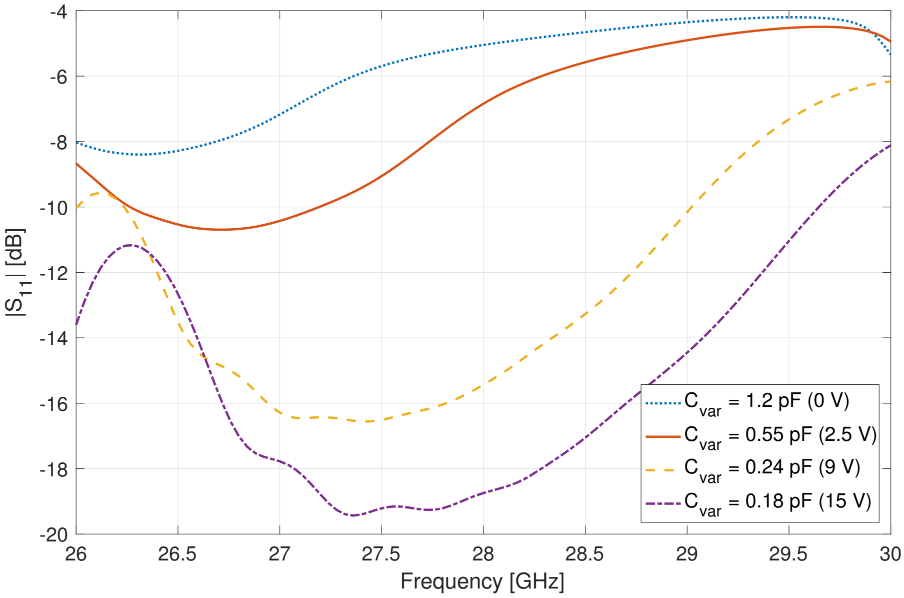

Fig. 5.12: Simulated S_{11} parameter of the varactor tuned LWA, in the case $N_{cell} = 15$. The traces corresponds to different capacity (voltage) values.

values, in the case $N_{cell} = 15$. Notice how the $|S_{11}|$ (return loss) stays below -10 dB at the working frequency of 26.5 GHz, apart from the case of higher capacity values (low voltages). We underline that, since the structure is geometrically symmetric, it is verified that the 2-port network is also symmetric, and indeed $S_{11} = S_{22}$ and $S_{21} = S_{12}$. The $|S_{21}|$ parameter (insertion loss) is very low in the entire band of interest, showing that there is no transmission to port 2 of a large fraction of power, since most of it has been radiated or dissipated in the dielectric and varactor losses. The different shape of the radiation patterns at θ_{max}, due to EM field degradation corresponding to the higher capacity values (observe the trace for $C_{var} = 1.2$ pF, $V = 0$ V), is therefore confirmed by the S-parameters, that show how at mmWave frequencies we have to be careful in designing the structure and choosing the varactors.

Angle - Gain vs Voltage: In Tab. 5.1 are reported the values of the main beam angle θ_{MB}, the corresponding peak gain G_{peak}, and the HPBW in the elevation plane, at different voltages values (i.e. varactor capacity values). All these data refer to the fixed frequency $f_w = 26.5$ GHz and the case $N_{cell} = 15$. This table numerically represents the values plotted in the graph of Fig. 5.14, that visually shows how the voltage sweep will control the main beam direction, together with the (unwanted) gain variation. We can see the voltage on x-axis, the corresponding peak gain and the scanning angle respectively on right and left y-axis. Notice the coherence between these values and the computed θ_{MB} values (Fig. 5.10) and the radiation pattern (Fig. 5.11).

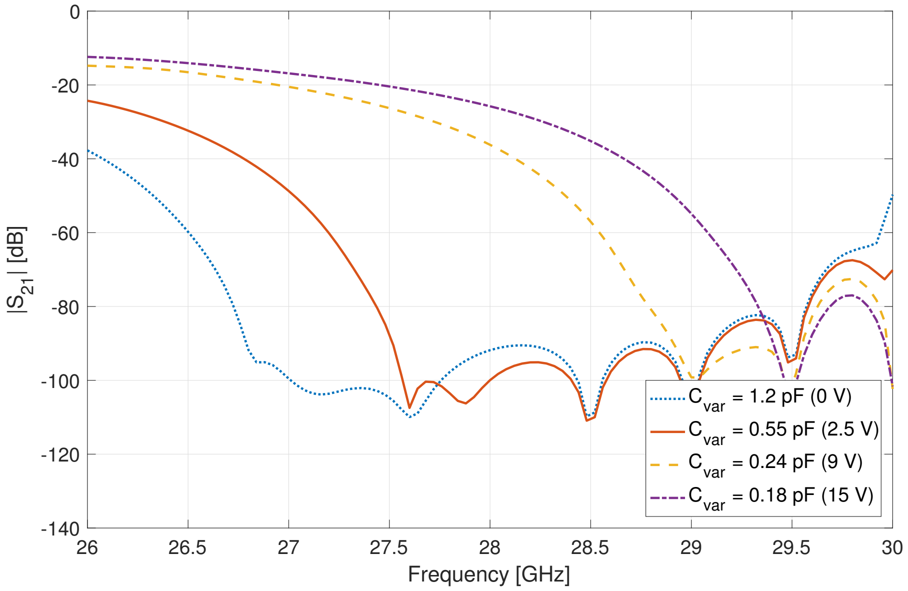

Fig. 5.13: Simulated S_{21} parameter of the varactor tuned LWA, in the case $N_{cell} = 15$. The traces corresponds to different capacity (voltage) values.

Analyzing these data, we observe a scan loss of approximately 5.2 dB (i.e. the gain variation between the scanning range ends). It is clearly a disadvantage, since it is quite high, but it will be handled with the LWA array application, since using more than one antenna the gain will rise. Moreover, one can decide to limit the scanning range, for example to $8° - 9°$, to reduce the scan loss to 4 dB.

Regarding this, we remember the possibility of making the beam scanning symmetric with respect to broadside direction, feeding alternatively port 1 or port 2 (see Fig. 4.11). If we use port 2 as power input port, the radiation behaviour in the elevation plane is overturned, as we can observe in Fig. 5.15: maintaining the same frequency and the same capacity value, we can obtain the symmetrical angle of scanning. In this way, a total scanning range of 24° can be achieved.

Moreover, we should notice that the diode capacity variation is not linear (see Fig. 4.12 and Tab. 5.1), indeed C_{var} halves when V changes from 0 V to 2 V, then it gradually decreases to 0.18 pF with V reaching 15 V. The characteristic is peculiar of the *hyperabrupt* varactor type, as the chosen Macom MA46H120, different from the *abrupt* ones, that demonstrates a smoother variation of the capacity. This trend clearly influences the angle sweep, that changes of 4° when the voltage increases from 0 V to 2 V, and then instead θ_{MB} has a variation of only 1° when V goes from 11 V to 15 V. The non-linear relation between the beamsteering angle and the control voltage has to be considered in future utilization of the antenna system, and therefore it requires components and a feeding network that enable an accurate tuning of the voltage, particularly at low values. This characteristic arises directly from the varactor behaviour, that is intrinsically a non-linear device. It's a problem

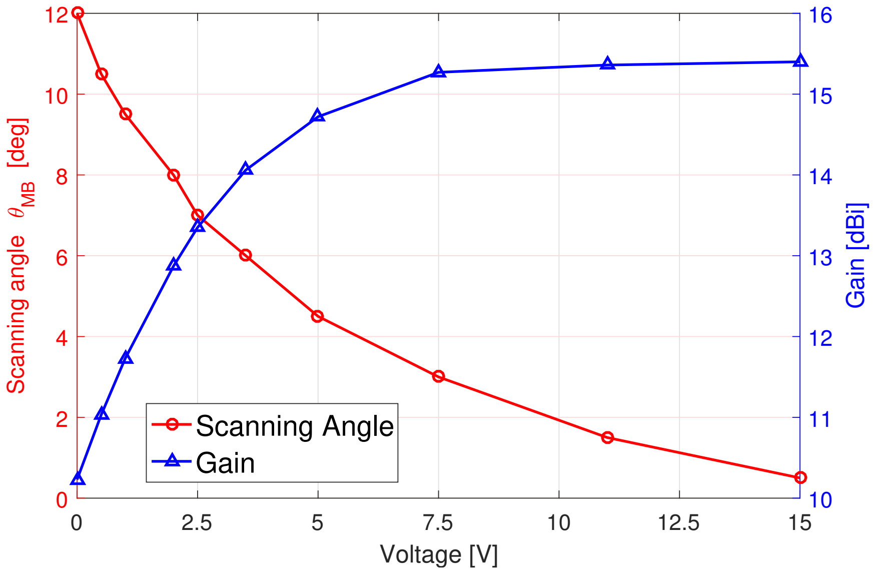

Fig. 5.14: Variation of the main beam angle (left y-axis) and the corresponding peak gain (right y-axis) with varactor bias voltage sweep. The simulations are conducted at frequency $f_w = 26.5$ GHz and with $N_{cell} = 15$.

that cannot easily be solved, but we could bypass it using diodes with a smoother capacity variation (abrupt varactors), eventually tuning them in the higher voltage range.

Furthermore, the above considerations are related to the *reconfiguration speed* of the system, i.e. the time needed to switch through the different possible configurations. Remembering the field of application of the antenna, it's clear that the switching time between one beam direction angle and another should be the shortest possible, to allow an efficient service to

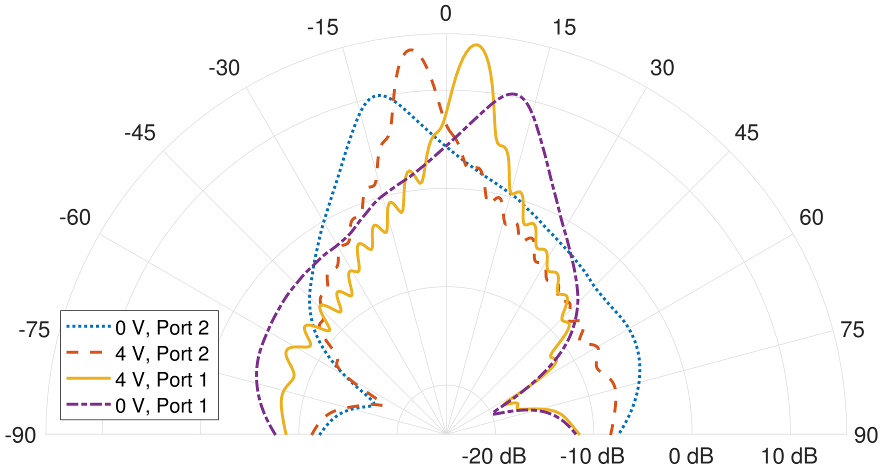

Fig. 5.15: Simulated radiation patterns that show the symmetrical behaviour of the varactor tuned LWA. Fixing the varactor capacity and feeding the antenna from input port 2, we steer the beam towards the symmetric negative angles, with respect to port 1. The simulations are conducted at frequency $f_w = 26.5$ GHz and with $N_{cell} = 15$.

Voltage [V]	**Varactor Capacity C_{var}** [pF]	**Scanning Angle θ_{MB}** [deg]	**Peak Gain G_{peak}** [dBi]	**HPBW** [deg]
0	1.2	12	10.23	11
0.5	1	10.5	11.03	9.5
1	0.82	9.5	11.73	8.5
2	0.61	8	12.87	7
2.5	0.55	7	13.35	6.5
3.5	0.45	6	14.06	5.5
5	0.34	4.5	14.72	5.5
7.5	0.28	3	15.27	5
11	0.2	1.5	15.36	5
15	0.18	0.5	15.4	4.5

Tab. 5.1: Varactor capacity value, scanning angle, peak gain, and HPBW of the main beam at different bias voltage values. The data regarding θ_{MB} and G_{peak} are represented in the graph of Fig. 5.14. The simulations are conducted at frequency $f_w = 26.5$ GHz and with $N_{cell} = 15$.

all the considered area. Generally, for outdoor small cell applications, the required scanning reconfiguration speed is in the order of 1° every tens-hundreds of nanoseconds.

Principally two factors contribute to this requirement: the varactor diode transit time, and the boost converter slew rate. The latter is a device that is needed to convert a fixed voltage in a variable voltage used to control the varactors. The transit time is a characteristic of the diodes, that affects the capacity variation time, once the voltage has been applied to the varactor pins. It should not be a problem, since in the case of low junction capacity, the varactors transit times are in the order of tens of nanoseconds.

Instead the slew rate of the boost converter will mostly influence the overall reconfiguration speed. It is a measure of the time response of the device, and it indicatively represents the time needed to switch from one voltage value to another. It can vary with the device quality, but generally it's in the range 4 - 10 V/μs. Therefore, once received the signal for the angle variation, the time response of the system will principally depend on the boost converter. In any case, this characteristic is influenced by many factors, thus the reasoning can be confirmed only by tests on a real prototype, that can give many more informations about the real overall functioning of the antenna system.

N_{cell} Variation: An important parameter, as already outlined, is the LWA length, directly dependent on the cells number N_{cell}. Also in this version of the LWA, the effects of N_{cell} variation have been investigated. Various data regarding peak gain and HPBW are reported in Tab. 5.2 and Fig. 5.16. At fixed frequency $f_w = 26.5$ GHz, we have varied N_{cell} from 4 to 20: we measured the peak gain with different varactor capacity values, that correspond to different beam directions (broadside, 8° and 12°), and the HPBW at broadside direction.

Cells Number N_{cell}	Gain at 0° [dBi]	Gain at 8° [dBi]	Gain at 12° [dBi]	HPBW at 0° [deg]
4	8.75	8.99	8.9	18
6	10.89	10.72	9.9	10
9	13.14	12.12	10.1	7
12	14.36	12.63	10.2	6
15	15.36	12.87	10.23	5
20	16.26	12.98	10.25	3.5

Tab. 5.2: Variation of the peak gain corresponding to different N_{cell} values, at frequency $f_w = 26.5$ GHz. The gain is measured in the case of the beam pointing at different directions (i.e. different C_{var} values), and is reported also the HPBW of the beam at broadside radiation.

Notice how, at broadside radiation ($V = 15$ V and $C_{var} = 0.18$ pF), the peak gain follows the trend predicted by theory (see Sec. 3.1), ad therefore it increases as the LWA length increases, setting toward a limit value of approximately 17 dBi. Differently, at $V = 0$ V and $V = 2$ V, corresponding to $C_{var} = 1.2$ pF and $C_{var} = 0.6$ pF, the gain rapidly saturates to a limit values and remains lower. This testifies once again the EM field degradation caused by the higher capacity values, and shows the impossibility of counteracting this phenomenon with the N_{cell} increasing. Moreover, the HPBW gets narrower as the length is increased, especially at lower N_{cell} values, indeed it decreases from 18° to 10°, varying N_{cell} from 4 to 6. Reading the rest of the Tab. 5.2, we notice that the HPBW continues to decrease, and this trend is related to the gain increase. We underline that this trend is present also at different scanning angle, but with minor improving. Finally, thanks to the above relations, we chose $N_{cell} = 15$ as final design parameter, also for the varactor tuned LWA.

Bandwidth and Beam Variation: Analyzing the frequency range of an LWA, it has to be remembered that its behaviour is strongly frequency dependent, and this fact clearly influences the available bandwidth. Although the varactor tuning design enables a fixed frequency beamsteering, when a C_{var} value is fixed, in any way the beam will change direction with frequency variation, as in the frequency scanning LWA. This is an inevitable intrinsic characteristic of the LWA structure, that cannot be neglected and has to be accounted since it can be an advantage or a disadvantage, depending on the application. We have to consider that using a channel with a significant bandwidth, the beam will enlarge with the frequency variation.

This characteristic is well explained observing Fig. 5.17. In these figures we can see the simulated radiation pattern (with $N_{cell} = 15$) in the elevation plane, corresponding to voltage values $V = 15$ V and $V = 2$ V, and in a configuration that simulates a channel bandwidth of 500 MHz: the gain patterns at $f_1 = 26.25$ GHz, $f_2 = 26.5$ GHz, $f_3 = 26.75$ GHz are reported.

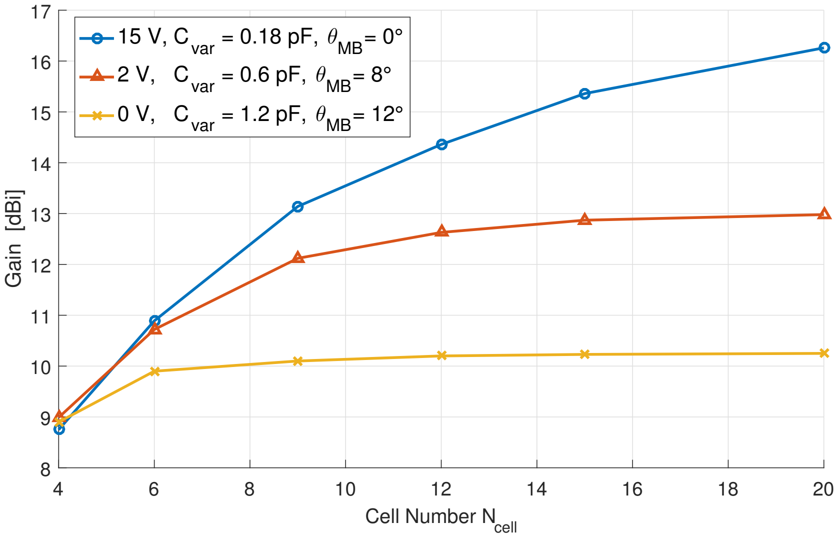

Fig. 5.16: Variation of the peak gain corresponding to different N_{cell} values, at frequency $f_w = 26.5$ GHz. The gain is measured in the case of the beam pointing at different directions (i.e. different C_{var} values).

In the case $V = 15$ V ($C_{var} = 0.18$ pF), the beam points towards broadside, and we notice that at different frequencies, the beam will steer, thus obtaining an overall beam approximately 4° wide, and with a gain that varies of 1 dB along the angle variation. Similarly, in the case $V = 2$ V ($C_{var} = 0.6$ pF), the gain and angle variation are quite the same. The total width of the radiated beam is therefore widened, depending on how much we increase the bandwidth.

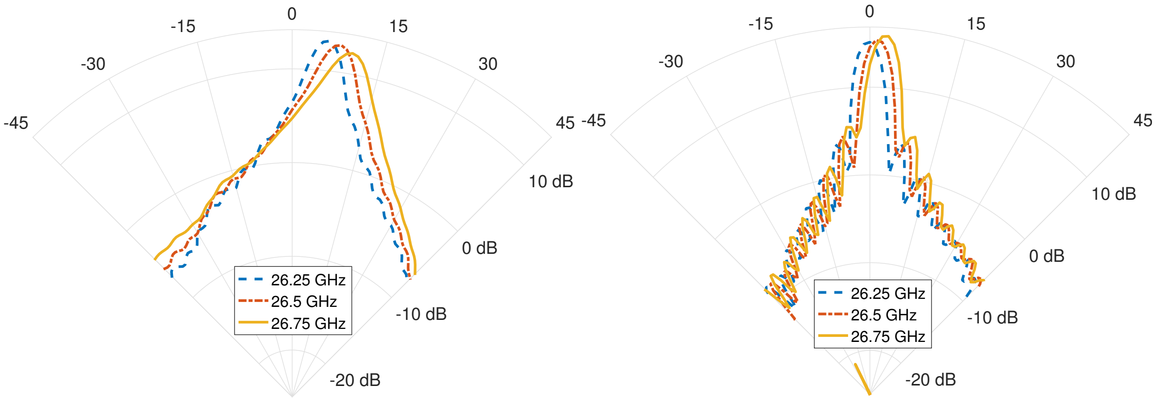

(a) $V = 2$ V, $C_{var} = 0.6$ pF

(b) $V = 15$ V, $C_{var} = 0.18$ pF

Fig. 5.17: Simulated radiation patterns with $N_{cell} = 15$ at frequencies $f_1 = 26.25$ GHz, $f_2 = 26.5$ GHz, $f_3 = 26.75$ GHz, in the case (a) $V = 2$ V and (b) $V = 15$ V.

Regarding this analysis, the positive aspect is that also with a frequency variation of hundreds of MHz, the LWA will keep its good behaviour, showing high gain and beamsteering, since the underlying SIW structure permits a wide impedance matching (as the S-parameters show), although the beam will widen. The beam widening is not a critical disadvantage, in the sense that to simultaneously reach a great number of users, a small cell will not require an extremely narrow beam, but it should maintain a certain width. Moreover, this problem has to be analyzed also in relation with the bandwidth that will be effectively used: indeed, as discussed, a 5G standard has not been finalized yet, and the channel bandwidth is not completely determined. The purpose is to get up to 1 GHz of instantaneous bandwidth, that is clearly challenging for an LWA structure, but it always depends on how the overall bandwidth will be eventually channelized.

A possible way to go round this problem is to try a cell tuning that manage to obtain a flatter β_L shape. In this way, the β_L and θ_{MB} variation with frequency will be reduced, therefore the beam will maintain more its angle even in the case of a wider bandwidth. To achieve a good beamsteering range, this solution should then be compensated with a larger capacity variation, with all the related problems already seen.

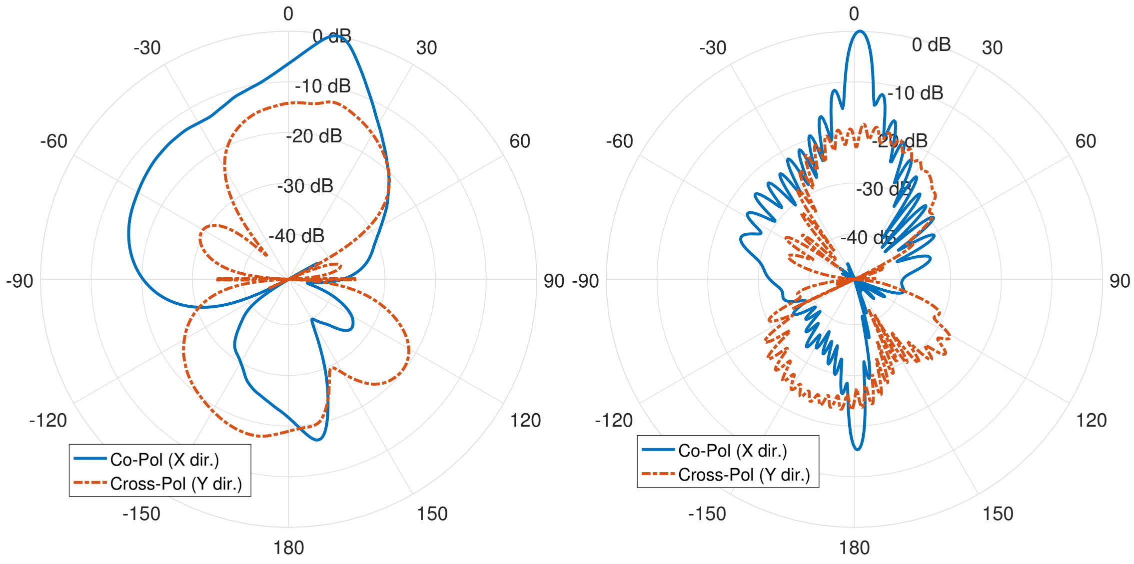

(a) $V = 0$ V, $C_{var} = 1.2$ pF **(b)** $V = 15$ V, $C_{var} = 0.18$ pF

Fig. 5.18: Normalized radiation patterns of the cross-polarized and the co-polarized components, in the case (a) $V = 0$ V and (b) $V = 15$ V. The simulations are conducted at frequency $f_w = 26.5$ GHz and with $N_{cell} = 15$.

Polarization: To investigate the radiated field polarization, we can observe Fig. 5.18. The complete normalized radiation patterns (with $N_{cell} = 15$ and at $f_w = 26.5$ GHz) in the two extreme case $V = 0$ V and $V = 15$ V ($C_{var} = 1.2$ pF and $C_{var} = 0.18$ pF) are reported,

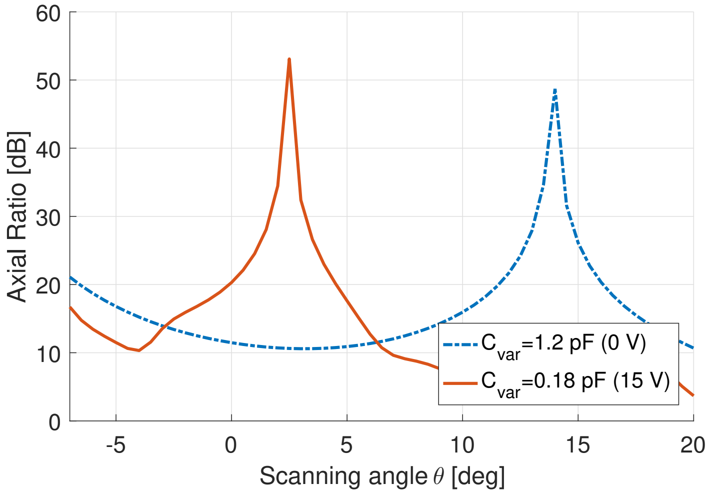

Fig. 5.19: Axial ratio in the case $V = 0$ V and $V = 15$ V, at frequency $f_w = 26.5$ GHz and with $N_{cell} = 15$.

in which we can observe the entire gain pattern as well as its two components, the cross-polarized and the co-polarized. We notice that the dominating co-polarization is the E-field component in the **x**-direction, indeed the cross-pol level in the **y**-direction is always at least 12 dB lower than the co-pol maximum and does not contribute too much to the overall gain. It is evident that the polarization is therefore linear, and it becomes a bit less pure in the $V = 0$ V case. The result is confirmed observing the Axial Ratio (AR), i.e. the ratio of the orthogonal components of the E-field. In Fig. 5.19 the AR it's reported in the angle range of interest, in the two cases $V = 0$ V and $V = 15$ V, so we can see that its values it's higher than 20 dB in correspondence of the angles of maximum radiation, respectively $\theta_{MB} = 12°$ and $\theta_{MB} = 0.5°$.

Azimuth Radiation Pattern: We also investigated the gain patterns in the azimuth (xz) plane, orthogonal to the main radiation plane, always referring to the coordinate system orientation of Fig. 4.11. The varactor tuned antenna demonstrates the classical LWA *fan* shaped beam, that is narrow in the beamsteering (yz) plane, and wide in the orthogonal (xz) plane, and covers almost all the upper hemisphere with respect to the antenna plane. We can observe the 3D radiation pattern in Fig. 5.20, that gives an idea of the overall shape of the radiated beam.

Moreover, in Fig. 5.21(a) are reported the gain patterns in the azimuth plane, in the case of: i) a single frequency scanning LWA, at $f = 28$ GHz, ii) a single varactor tuned LWA iii) two identical varactor tuned LWAs put side by side with a center-to-center distance of $d_{LWA} = 9$ mm, and that are fed by signals at the same phase. All the LWAs are composed by $N_{cell} = 15$ cells, and the simulations of the varactor tuned LWAs are conducted at $f_w = 26.5$ GHz, and relative to the case of $V = 15$ V, $C_{var} = 0.18$ pF.

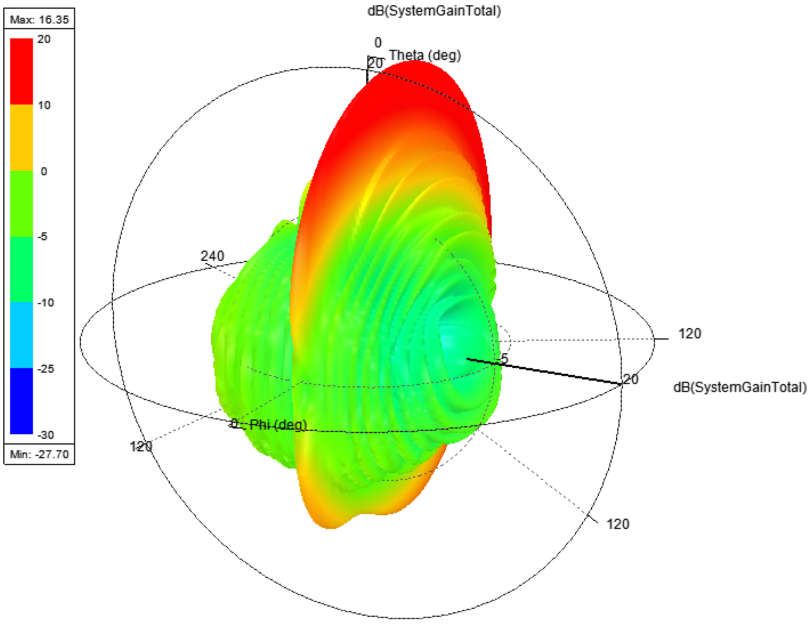

Fig. 5.20: 3D simulated radiation pattern of the varactor tuned LWA, at frequency $f_w = 26.5$ GHz and with $N_{cell} = 15$. Notice the fan shaped beam, that is wide in the azimuth plane and narrow in the elevation plane.

Notice how in the first two cases the beam is wide, indeed this characteristic is suitable for an array application. As already discussed in Chap. 4, a number of identical LWAs can be used as single elements, to create a *columns* array that can perform azimuth beamsteering, besides the elevation one. Considering this concept, we perform simulations to confirm the possibility, and the results are good: we can see how, with 2 LWAs, the beam in the azimuth plane is narrower with respect to the single LWA cases. Since the radiated fields interfere constructively, the peak gain in the main beam direction increases to 18.5 dBi, approximately 3 dBi higher with respect to the case of a single varactor tuned LWA (see Tab. 5.1 and Fig. 5.11). The side lobes level is however high, but can be lowered increasing the number of LWAs and tuning their distances.

Moreover, we can notice that the gain patterns of Fig. 5.21(a) demonstrate a certain asymmetry with respect to $\theta = 0°$. This can lead to some problems regarding the azimuth beamsteering functionality, but with a higher number of LWAs placed side by side, the lateral lobes will significantly decrease, thus minimizing the asymmetry. However, the issue depends once again on the unit cell behaviour, since also its gain pattern in the azimuth plane it's a bit asymmetric. We can observe this characteristic in Fig. 5.21(b), that presents the radiation pattern of the unit cell in the case of: i) unit cell without varactors (Fig. 4.7) at $f = 28$ GHz, ii) unit cell with varactors (Fig. 4.10), at $f_w = 26.5$ GHz, with voltage $V = 15$ V. Notice how the shape of the cell gain pattern influences the patterns of the complete LWAs, comparing Fig. 5.21(b) with Fig. 5.21(a).

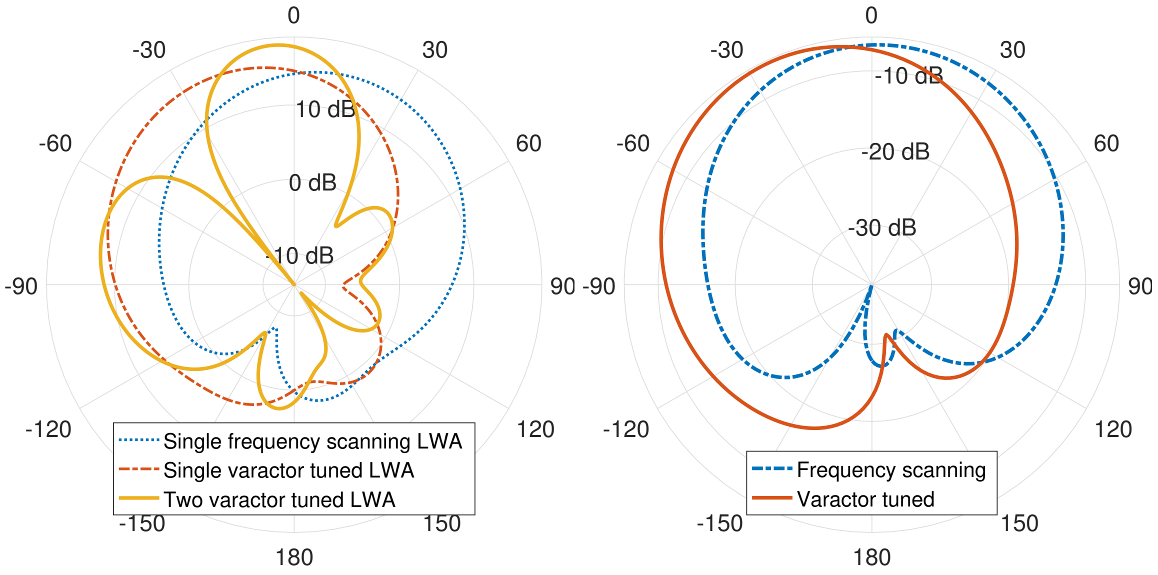

(a) LWAs **(b)** Unit cells

Fig. 5.21: Simulated radiation patterns in the azimuth plane, in the case of (a) different configurations of the complete antenna, (b) frequency scanning and varactor tuned unit cells

The simulations regarding this array-like application are still preliminary, but they give good indications on the feasibility of a narrower beam also in the azimuth plane, that can be steered thanks to phase shifting between the single LWAs. In this way the system can almost achieve a *pencil* beam that can perform a 3D scanning in a hemisphere.

Bloch Impedance: The overall performances of the LWA are related also to the impedance of the CRLH TL. In the case of periodic transmission lines, the quantity to be investigated is the *Bloch* impedance Z_B, that gives informations regarding the matching of the line and the balancing of the unit cell [50, 75]. In particular, the real part $\mathrm{Re}(Z_B)$ is related to the impedance discontinuity between the CRLH TL and, in our case, the microstrip transition. Therefore, this quantity should be as much close as possible to the value of 50 Ω. The imaginary part $\mathrm{Im}(Z_B)$ it's constant and equal to zero in the case of an ideal balanced CRLH TL, remembering that this particular line demonstrates a characteristic impedance constant and real over the entire bandwidth (Sec. 2.2.1). In the case of a concrete CRLH TL, if the line is well balanced, the $\mathrm{Im}(Z_B)$ will be always close to zero, except for the frequencies near f_0: the cell balancing arises from a zero-pole cancellation in the characteristic impedance expression [50], therefore, since in a real CRLH TL this cancellation will never be totally precise, the f_0 region in the Z_B plot will always show a peculiar behaviour, with wide fluctuations.

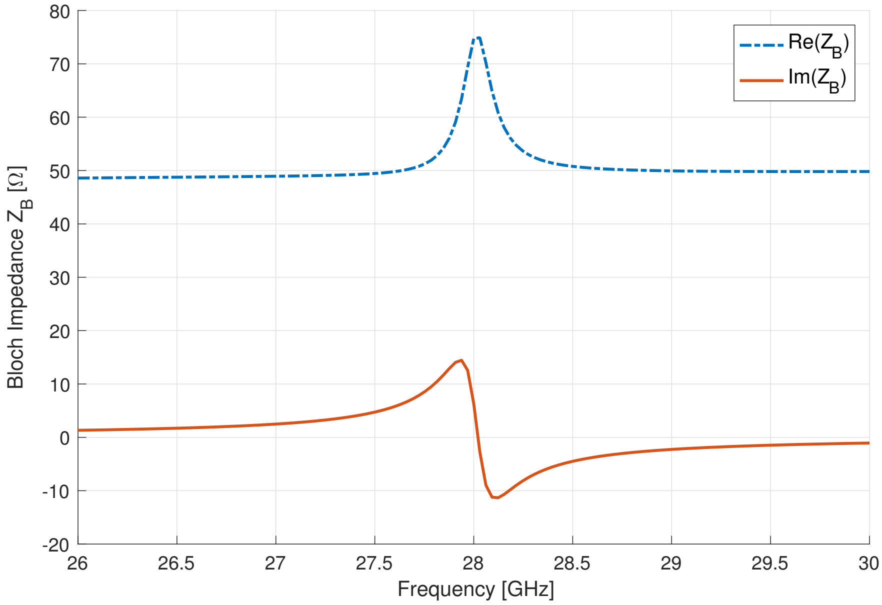

Fig. 5.22: Bloch impedance real and imaginary part of the frequency scanning LWA unit cell.

The Bloch impedance can be computed from ABCD matrix parameters as [50]:

$$Z_B = \frac{A - D + \sqrt{(A+D)^2 - 4}}{2C}, \tag{5.1}$$

which reduces to

$$Z_B = \frac{B}{\sqrt{A^2 - 1}} = \frac{\sqrt{D^2 - 1}}{C}, \tag{5.2}$$

if the unit cell is symmetric ($A = D$). These expressions, substituting ABCD parameters with S-parameters, become [76]:

$$Z_B = Z_0 \sqrt{\frac{(1 + S_{11})^2 - S_{21}^2}{(1 - S_{11})^2 - S_{21}^2}}, \tag{5.3}$$

where Z_0 is the reference impedance, i.e. 50 Ω in our case. In the following results, the Bloch impedances have been computed using (5.3).

In Fig. 5.22 are depicted the real and imaginary part of the Bloch impedance of the frequency scanning LWA unit cell (Fig. 4.7). Remembering the above considerations, we notice that $\mathrm{Re}(Z_B)$ takes values near 50 Ω apart from the peak near f_0, confirming the good impedance matching of the line. The imaginary part $\mathrm{Im}(Z_B)$, similarly, stays always near zero and has a *jump* between 27.5 GHz and 28.5 GHz. These results are coherent with the good characteristics of the frequency scanning LWA, in terms of radiation pattern shape (Fig. 5.6, Fig. 5.3) and gain (Fig. 5.5).

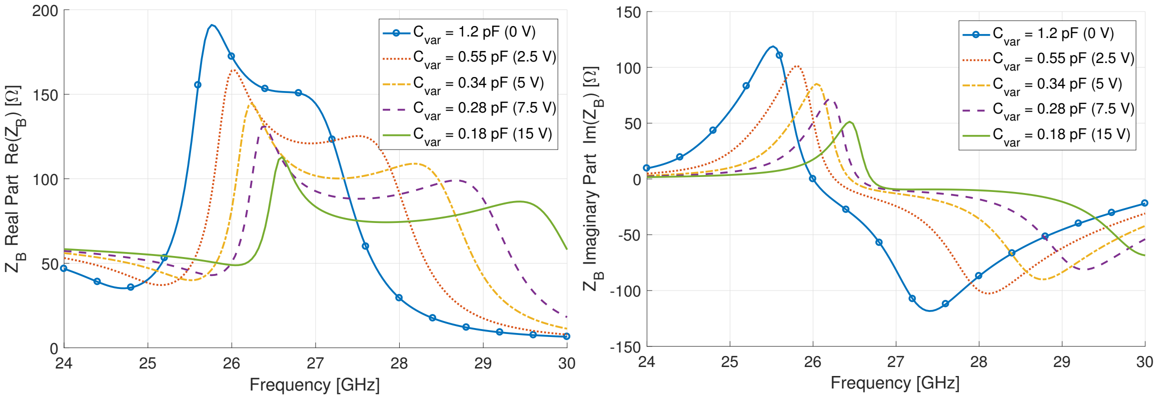

(a) Real part

(b) Imaginary part

Fig. 5.23: Bloch impedance of the varactor tuned LWA unit cell, at different capacity (voltage) values.

Considering the varactor tuned LWA unit cell, we can observe the real and imaginary part of Z_B in Fig. 5.23, in which are reported $\mathrm{Re}(Z_B)$ and $\mathrm{Im}(Z_B)$ at different capacity (voltage) values. Notice how the real part shape changes significantly from the case $C_{var} = 0.18$ pF to $C_{var} = 1.2$ pF: in the latter case, the value of $\mathrm{Re}(Z_B)$ at $f_w = 26.5$ GHz it's approximately 150 Ω, clearly too far from the reference value $Z_0 = 50\,\Omega$. In the case $C_{var} = 0.18$ pF instead, $\mathrm{Re}(Z_B)$ stays on values next to 50 Ω.
The imaginary part shows the same worsening, sweeping from $\min(C_{var})$ to $\max(C_{var})$: we can see how, in the first case, the fluctuations far from $\mathrm{Im}(Z_B) = 0$ are restrained, on the contrary instead, when C_{var} increases, the oscillations become wider, underlining the lack of balancing of the unit cell in correspondence of high capacity values. All these behaviours confirm the reported characteristics of the varactor tuned LWA, in particular the gain pattern (Fig. 5.11) that gets worse when C_{var} increases. Once again this fact can be related to the unit cell behaviour, confirming the possibility and the need of a deep investigation of its design and characteristics, in order to improve the overall LWA performances.

β_L and k_0 Considerations: As already largely observed, the phase constant β_L heavily determines the achievable scanning range of the LWA. We remember that the formula of the main beam angle θ_{MB} is determined also by other quantities, that are the wavenumber $k_0 = 2\pi f/c$ (also called *airline*) and the cell length L_{cell}:

$$\theta_{MB}(f) = \sin^{-1}\left[\frac{\beta(f)}{k_0}\right] = \sin^{-1}\left[\frac{\beta_L(f)}{k_0\; L_{cell}}\right]. \tag{5.4}$$

We can then affirm that is the ratio between β_L and $k_0 \cdot L_{cell}$ that determines the maximum beamsteering angle: if this ratio tends to ±1, θ_{MB} tends to ±90°, that is the maximum reachable angle. We deduce that it's useful to observe the two quantities in the same graph,

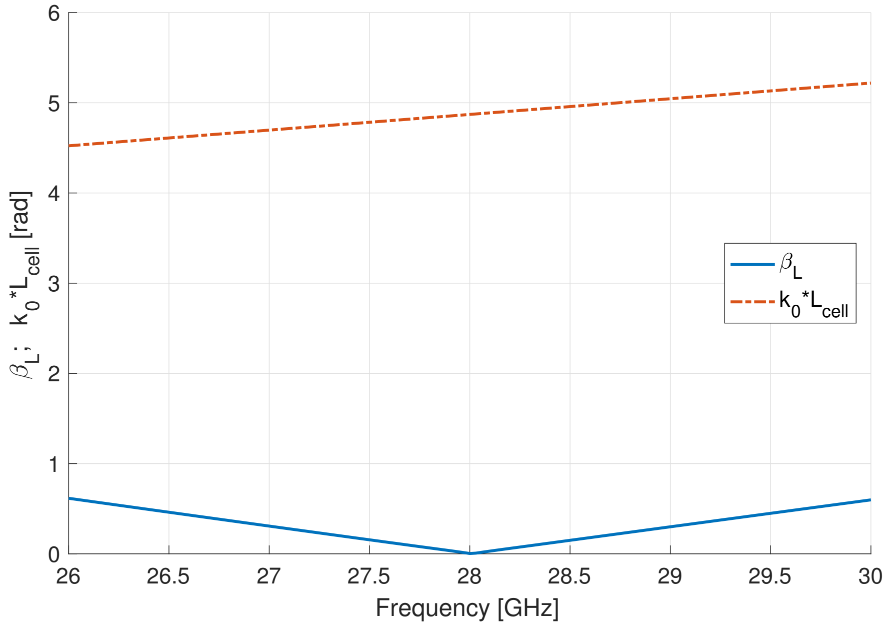

Fig. 5.24: Dispersion diagram of the frequency scanning LWA unit cell, with *airline* trace.

because we can see that the more their values are close to each other, the more the scanning range will be wide. In Fig. 5.24 is depicted a dispersion diagram together with the trace of $k_0 \cdot L_{cell}$. The β_L is the same of Fig. 5.1, relative to the unit cell of the frequency scanning LWA. Clearly, as already seen, this quantity then affects also the varactor tuned LWA.

Notice how β_L and $k_0 \cdot L_{cell}$ are far apart, thus their ratio will be $\ll 1$ and the scanning range is limited. To improve this, the goal is to increase the β_L slope, making it possibly steeper, in order to bring its values near to $k_0 \cdot L_{cell}$. We remember that the wavenumber cannot be modified, since it is directly proportional to frequency, and it does not depend on the cell geometry, although there's L_{cell} but only as a scaling factor. Therefore, the only chance is to modify the phase constant through cell tuning, changing its geometry and trying to increase the CRLH contributions. Obtaining a wider variation of β_L clearly improves the scanning range, but remembering the above considerations, this will affect the performances in terms of bandwidth.

Conclusions

The incoming 5G system will bring many changes and improvements in the mobile communications and, because of that, it's pushing the research community to develop new solutions. These regard various fields of application, and in particular the new network architecture will bring to the deployment of a large number of small cells. This short range type of communication requires new antenna systems, that, as already discussed, work at higher frequencies. For this reason, it is necessary to develop radiating elements with a high directivity, a narrow beam, and beamsteering capability, so that the antenna can serve efficiently different areas. This is the background in which has been drafted the thesis, that investigated the possibility of developing a metamaterial based Leaky Wave Antenna, on a Substrate Integrated Waveguide, that works in the band of 26 GHz - 30 GHz and provides high gain and beamsteering functionality.

The chapter 1 presented an introductory review on 5G system and related innovations, together with an overview on mmWave propagation characteristics and antennas. Chapter 2 described the state of the art regarding SIW structure and CRLH transmission line, the two main and fundamental concepts that make the basis for our antenna. In chapter 3 the LWA theory is reported, explaining how the antenna radiates the EM energy, and in particular presenting the functioning of the metamaterial based LWAs. The antennas design is described in chapter 4, where firstly the frequency scanning LWA is reported, followed by the varactor tuned version. Finally, the chapter 5 presented the obtained results, for both the antenna versions, investigating their overall performances in terms of peak gain and beamsteering range.

The two LWAs provide good functionalities, and they meet, albeit partially, the general small cell antenna requirements. The frequency scanning version is only a preliminary study, that is needed for the subsequent analysis of the varactor tuned LWA. It demonstrated good characteristics, with a peak gain of 14.5 dBi in the case $N_{cell} = 15$, and a beamsteering range of 13° sweeping the frequency from 26 GHz to 30 GHz. We underline that this is not an antenna completely useful for a small cell application, since one wants to be able to steer the beam at a fixed frequency, but this LWA can still be prototyped to verify the simulated performances with real tests, using a simpler design with respect to the varactor tuned version. This last one is indeed the main objective of the study, and it has been deeply described and investigated.

The varactor tuned LWA, thanks to the diodes insertion, provides a voltage controlled beam that can be steered at fixed frequency $f_w = 26.5$ GHz from 12° to 0.5° increasing the voltage from 0 V to 15 V, and moreover can cover also the symmetric negative angles using alternatively as input port 1 or port 2. The peak gain with $N_{cell} = 15$ is maximum at broadside radiation, where it reaches 15.4 dBi, and decreases to 10.2 dBi at $\theta_{MB} = 12°$. The antenna presents good characteristics with respect to the 5G small cell antennas requirements, although it has to be improved in particular regarding the beamsteering range.

The work then concentrated on investigating the achievable performances and on the unit cell effects, understanding which features affected most the complete LWA. In particular we verified that the design phase can concentrate on the fundamental cell study, since this element strongly influences the radiating performances, and we described which quantities influence the gain, the beamsteering range, the beam shape. In this way, a future designer who wants to improve this system will know which parameters he should observe, and will have a lot of precious informations to develop new versions of the SIW varactor tuned LWA.

In general, this work is a feasibility study that wants to understand if this type of antenna system is suitable for a small cell application. We can conclude that the LWA is a promising candidate, remembering also the important advantage of the absence of phase shifters that lowers the overall cost and the complexity of the system. The future works will clearly focus on the implementation of a prototype, to confirm the simulated results with real measurements. In particular the varactor placements will be critical, and the accordance between simulations and tests should be verified. Moreover, other unit cell geometries can be designed, starting from the numerous available references, trying to optimize and improve the gain and the beamsteering range. Finally, also the possibility of composing an array of LWAs, that can steer the beam both in elevation and azimuth plane, should be deeply investigated, to make the antenna ready and suitable for a real 5G small cell application.

Bibliography

[1] G. S. C. Frank Mademann. *System architecture milestone of 5G Phase 1 is achieved*. Dec. 2017. URL: `http://www.3gpp.org/news-events/3gpp-news/1930-sys_architecture` (visited on 01/10/2018).

[2] Ericsson and N. Heuveldop. *Ericsson Mobility Report*. Nov. 2017. URL: `https://www.ericsson.com/en/mobility-report` (visited on 01/10/2018).

[3] K. Mallinson. *The path to 5G: as much evolution as revolution*. May 2016. URL: `http://www.3gpp.org/news-events/3gpp-news/1774-5g_wiseharbour` (visited on 01/25/2018).

[4] ITU-R. *ITU towards IMT for 2020 and beyond*. URL: `https://www.itu.int/en/ITU-R/study-groups/rsg5/rwp5d/imt-2020/Pages/default.aspx` (visited on 01/10/2018).

[5] ITU-R. *Emerging Trends in 5G - IMT 2020*. Sept. 2016. URL: `https://www.itu.int/en/membership/Documents/missions/GVA-mission-briefing-5G-28Sept2016.pdf` (visited on 01/30/2018).

[6] ITU-R. *Minimum requirements related to technical performance for IMT-2020 radio interface(s)*. Feb. 2017. URL: `https://www.itu.int/md/R15-SG05-C-0040/it` (visited on 01/30/2018).

[7] ITU-R. *IMT Vision - Framework and overall objectives of the future development of IMT for 2020 and beyond*. Sept. 2015. URL: `https://www.itu.int/dms_pubrec/itu-r/rec/m/R-REC-M.2083-0-201509-I!!PDF-E.pdf` (visited on 01/10/2018).

[8] M. Agiwal, A. Roy, and N. Saxena. "Next generation 5G wireless networks: A comprehensive survey". In: *IEEE Communications Surveys & Tutorials* 18.3 (2016), pp. 1617–1655.

[9] A. Osseiran, J. F. Monserrat, and P. Marsch. *5G mobile and wireless communications technology*. Cambridge University Press, 2016.

[10] J. G. Andrews et al. “What will 5G be?” In: *IEEE Journal on selected areas in communications* 32.6 (2014), pp. 1065–1082.

[11] A. Gupta and R. K. Jha. “A survey of 5G network: Architecture and emerging technologies”. In: *IEEE access* 3 (2015), pp. 1206–1232.

[12] C.-X. Wang et al. “Cellular architecture and key technologies for 5G wireless communication networks”. In: *IEEE Communications Magazine* 52.2 (2014), pp. 122–130.

[13] Huawei Whitepaper. *5G: New Air Interface and Radio Access Virtualization*. Apr. 2015. URL: `http://www.huawei.com/minisite/has2015/img/5g_radio_whitepaper.pdf` (visited on 01/24/2018).

[14] T. Wild, F. Schaich, and Y. Chen. “5G air interface design based on universal filtered (UF-) OFDM”. In: *Digital Signal Processing (DSP), 2014 19th International Conference on*. IEEE. 2014, pp. 699–704.

[15] U. F. C. Commission. *FCC Adopts Rules to Facilitate Next Generation Wireless Technologies*. July 2016. URL: `https://www.fcc.gov/document/fcc-adopts-rules-facilitate-next-generation-wireless-technologies` (visited on 01/30/2018).

[16] ITU-R. *Studies on frequency-related matters for International Mobile Telecommunications identification including possible additional allocations to the mobile services on a primary basis in portion(s) of the frequency range between 24.25 and 86 GHz for the future development of International Mobile Telecommunications for 2020 and beyond*. Nov. 2015. URL: `https://www.itu.int/dms_pub/itu-r/oth/0c/0a/R0C0A00000C0014PDFE.pdf` (visited on 01/30/2018).

[17] J. Qiao. “Enabling Millimeter Wave Communication for 5G Cellular Networks: MAC-layer Perspective”. Ph.D. Dissertation. University of Waterloo, 2015.

[18] T. S. Rappaport et al. “Millimeter wave mobile communications for 5G cellular: It will work!” In: *IEEE access* 1 (2013), pp. 335–349.

[19] W. Roh et al. “Millimeter-wave beamforming as an enabling technology for 5G cellular communications: Theoretical feasibility and prototype results”. In: *IEEE communications magazine* 52.2 (2014), pp. 106–113.

[20] E-Band Communications. *E-band technology*. URL: `https://www.e-band.com/index.php?id=86` (visited on 01/30/2018).

[21] S. Rangan, T. S. Rappaport, and E. Erkip. “Millimeter-wave cellular wireless networks: Potentials and challenges”. In: *Proceedings of the IEEE* 102.3 (2014), pp. 366–385.

[22] T. S. Rappaport et al. “Overview of Millimeter Wave Communications for Fifth-Generation (5G) Wireless Networks—With a Focus on Propagation Models”. In: *IEEE Transactions on Antennas and Propagation* 65.12 (2017), pp. 6213–6230.

[23] S. Geng et al. “Millimeter-wave propagation channel characterization for short-range wireless communications”. In: *IEEE Transactions on Vehicular Technology* 58.1 (2009), pp. 3–13.

[24] 3rd Generation Partnership Project (3GPP). *Study on channel model for frequencies from 0.5 to 100 GHz*. Aug. 2017. URL: `http://www.3gpp.org/DynaReport/38901.htm` (visited on 01/30/2018).

[25] J. du Preez and S. Sinha. *Millimeter-Wave Antennas: Configurations and Applications*. Signals and Communication Technology. Springer International Publishing, 2016.

[26] G. Brown, Qualcomm, and Heavy Reading. *Exploring the potential of mmWave for 5G mobile access*. June 2016. URL: `https://www.qualcomm.com/media/documents/files/heavy-reading-whitepaper-exploring-5g-new-radio-use-cases-capabilities-timeline.pdf` (visited on 01/30/2018).

[27] W. Hong et al. “Multibeam Antenna Technologies for 5G Wireless Communications”. In: *IEEE Transactions on Antennas and Propagation* 65.12 (2017), pp. 6231–6249.

[28] M. Ando et al. “PoC of mmWave (40 and 60 GHz) Integrated 5G Heterogeneous Networks”. In: *European Wireless 2016; 22th European Wireless Conference; Proceedings of*. VDE. 2016, pp. 1–4.

[29] Anokiwave. *AWMF-0129 5G Active Antenna Innovator's Kit*. 2017. URL: `http://www.anokiwave.com/products/awmf-0129/index.html` (visited on 01/30/2018).

[30] B. Sadhu and IBM. *Presented Today at IEEE Conference: Making 5G a Reality*. Feb. 2017. URL: `https://www.ibm.com/blogs/research/2017/02/presented-today-at-ieee-conference-making-5g-a-reality/` (visited on 01/30/2018).

[31] X. Gu et al. "A multilayer organic package with 64 dual-polarized antennas for 28GHz 5G communication". In: *Microwave Symposium (IMS), 2017 IEEE MTT-S International*. IEEE. 2017, pp. 1899–1901.

[32] M. I. ul haq Malik, H. Kaouach, and E. Korkmaz. "Linearly-polarized transmit-arrays for mmwave applications; comparative study and perspective". In: *Antennas and Propagation (EuCAP), 2016 10th European Conference on*. IEEE. 2016, pp. 1–5.

[33] A. U. Zaman and P.-S. Kildal. "Different gap waveguide slot array configurations for mmwave fixed beam antenna application". In: *Antennas and Propagation (EuCAP), 2016 10th European Conference on*. IEEE. 2016, pp. 1–4.

[34] J. Hirokawa and M. Ando. "Single-layer feed waveguide consisting of posts for plane TEM wave excitation in parallel plates". In: *IEEE Transactions on Antennas and Propagation* 46.5 (1998), pp. 625–630.

[35] H. Uchimura, T. Takenoshita, and M. Fujii. "Development of a" laminated waveguide"". In: *IEEE Transactions on Microwave Theory and Techniques* 46.12 (1998), pp. 2438–2443.

[36] ANSYS HFSS. *High frequency electromagnetic field simulation, ver. 18.1*. Ansys, Inc., 2017.

[37] D. M. Pozar. *Microwave engineering*. John Wiley & Sons, 2009.

[38] F. Xu and K. Wu. "Guided-wave and leakage characteristics of substrate integrated waveguide". In: *IEEE Transactions on microwave theory and techniques* 53.1 (2005), pp. 66–73.

[39] D. Deslandes and K. Wu. "Accurate modeling, wave mechanisms, and design considerations of a substrate integrated waveguide". In: *IEEE Transactions on microwave theory and techniques* 54.6 (2006), pp. 2516–2526.

[40] J. E. Rayas-Sanchez and V. Gutierrez-Ayala. “A general EM-based design procedure for single-layer substrate integrated waveguide interconnects with microstrip transitions”. In: *Microwave Symposium Digest, 2008 IEEE MTT-S International*. IEEE. 2008, pp. 983–986.

[41] Y. Cassivi et al. “Dispersion characteristics of substrate integrated rectangular waveguide”. In: *IEEE Microwave and Wireless components letters* 12.9 (2002), pp. 333–335.

[42] M. Bozzi, A. Georgiadis, and K. Wu. “Review of substrate-integrated waveguide circuits and antennas”. In: *IET Microwaves, Antennas & Propagation* 5.8 (2011), pp. 909–920.

[43] T. Djerafi, A. Doghri, and K. Wu. “Substrate Integrated Waveguide Antennas”. In: *Handbook of Antenna Technologies*. Springer, 2015, pp. 1–60.

[44] D. Deslandes and K. Wu. “Integrated microstrip and rectangular waveguide in planar form”. In: *IEEE Microwave and Wireless Components Letters* 11.2 (2001), pp. 68–70.

[45] D. Deslandes. “Design equations for tapered microstrip-to-substrate integrated waveguide transitions”. In: *Microwave Symposium Digest (MTT), 2010 IEEE MTT-S International*. IEEE. 2010, pp. 704–707.

[46] A. Suntives. “High-speed data transmission using substrate integrated waveguide-type interconnects”. PhD thesis. McGill University, 2009.

[47] D. R. Smith et al. “Composite medium with simultaneously negative permeability and permittivity”. In: *Physical review letters* 84.18 (2000), p. 4184.

[48] A. Lai, T. Itoh, and C. Caloz. “Composite right/left-handed transmission line metamaterials”. In: *IEEE microwave magazine* 5.3 (2004), pp. 34–50.

[49] V. G. Veselago. “The electrodynamics of substances with simultaneously negative values of and μ”. In: *Soviet physics uspekhi* 10.4 (1968), p. 509.

[50] C. Caloz and T. Itoh. *Electromagnetic metamaterials: transmission line theory and microwave applications*. John Wiley & Sons, 2005.

[51] A. Lai, C. J. Lee, and T. Itoh. "Metamaterials for antenna applications". In: *Advanced Millimeter-Wave Technologies: Antennas, Packaging and Circuits* (2009), pp. 385–412.

[52] M. A. Antoniades, H. Mirzaei, and G. V. Eleftheriades. "Transmission-line based metamaterials in antenna engineering". In: *Handbook of Antenna Technologies* (2014), pp. 1–60.

[53] I.-H. Lin, C. Caloz, and T. Itoh. "A branch-line coupler with two arbitrary operating frequencies using left-handed transmission lines". In: *Microwave Symposium Digest, 2003 IEEE MTT-S International*. Vol. 1. IEEE. 2003, pp. 325–328.

[54] A. Sanada et al. "A planar zeroth-order resonator antenna using a left-handed transmission line". In: *Microwave Conference, 2004. 34th European*. Vol. 3. IEEE. 2004, pp. 1341–1344.

[55] M. Facco and D. Piazza. "Reconfigurable zero-order loop antenna". In: *Antennas and Propagation Society International Symposium (APSURSI), 2012 IEEE*. IEEE. 2012, pp. 1–2.

[56] X. Q. Lin et al. "Novel composite phase-shifting transmission-line and its application in the design of antenna array". In: *IEEE Transactions on Antennas and Propagation* 58.2 (2010), pp. 375–380.

[57] X. Q. Lin et al. "Design and analysis of super-wide bandpass filters using a novel compact meta-structure". In: *IEEE Transactions on Microwave Theory and Techniques* 55.4 (2007), pp. 747–753.

[58] W. W. Hansen. *Radiating electromagnetic wave guide*. US Patent 2,402,622. June 1946.

[59] A. A. Oliner and D. R. Jackson. "Leaky-wave antennas". In: *Antenna engineering handbook*. Vol. 4. New York: McGraw-Hill, 1993.

[60] T Tamir. *Leaky-wave antennas*. 1969.

[61] S. Lim, C. Caloz, and T. Itoh. "Metamaterial-based electronically controlled transmission-line structure as a novel leaky-wave antenna with tunable radiation angle and beamwidth". In: *IEEE Transactions on Microwave Theory and Techniques* 52.12 (2004), pp. 2678–2690.

[62] J. H. Choi and T. Itoh. “Beam-Scanning Leaky-Wave Antennas”. In: *Handbook of Antenna Technologies*. Ed. by Z. N. Chen et al. Springer, 2016, pp. 1697–1735.

[63] C. Caloz, T. Itoh, and D. R. Jackson. “Leaky-Wave Antennas”. In: *Frontiers in antennas: next generation design & engineering*. Ed. by F. Gross. McGraw Hill Professional, 2010.

[64] J. Du Preez and S. Sinha. “Leaky-Wave Antennas”. In: *Millimeter-wave antennas: configurations and applications*. Springer International Publishing, 2016.

[65] C. Caloz. “A ten-year journey in leaky-wave antennas”. In: *Antenna Measurements & Applications (CAMA), 2015 IEEE Conference on*. IEEE. 2015, pp. 1–4.

[66] L. Liu, C. Caloz, and T. Itoh. “Dominant mode leaky-wave antenna with backfire-to-endfire scanning capability”. In: *Electronics Letters* 38.23 (2002), pp. 1414–1416.

[67] C. Caloz and T. Itoh. “Array factor approach of leaky-wave antennas and application to 1-D/2-D composite right/left-handed (CRLH) structures”. In: *IEEE Microwave and wireless components letters* 14.6 (2004), pp. 274–276.

[68] R. E. Horn et al. “Electronic modulated beam-steerable silicon waveguide array antenna”. In: *IEEE transactions on microwave theory and techniques* 28.6 (1980), pp. 647–653.

[69] H. Maheri, M. Tsutsumi, and N. Kumagai. “Experimental studies of magnetically scannable leaky-wave antennas having a corrugated ferrite slab/dielectric layer structure”. In: *IEEE transactions on antennas and propagation* 36.7 (1988), pp. 911–917.

[70] K. Sato et al. “Electronically scanned left-handed leaky wave antenna for millimeter-wave automotive applications”. In: *Antenna Technology Small Antennas and Novel Metamaterials, 2006 IEEE International Workshop on*. IEEE. 2006, pp. 420–423.

[71] Y. Dong and T. Itoh. “Composite right/left-handed substrate integrated waveguide and half mode substrate integrated waveguide leaky-wave structures”. In: *IEEE Transactions on Antennas and Propagation* 59.3 (2011), pp. 767–775.

[72] S. Doucha, M. Abri, and H. A. Badaoui. “Leaky Wave Antenna Design based on SIW Technology for Millimeter Wave Applications”. In: *WSEAS Transactions On Communications* 14 (2015), pp. 2224–2864.

[73] Y. J. Cheng et al. "Millimeter-wave substrate integrated waveguide long slot leaky-wave antennas and two-dimensional multibeam applications". In: *IEEE Transactions on Antennas and Propagation* 59.1 (2011), pp. 40–47.

[74] J. Xu et al. "Half-mode substrate integrated waveguide (HMSIW) leaky-wave antenna for millimeter-wave applications". In: *IEEE antennas and wireless propagation letters* 7 (2008), pp. 85–88.

[75] A. Suntives and S. V. Hum. "A fixed-frequency beam-steerable half-mode substrate integrated waveguide leaky-wave antenna". In: *IEEE Transactions on Antennas and Propagation* 60.5 (2012), pp. 2540–2544.

[76] A. Suntives and S. V. Hum. "An electronically tunable half-mode substrate integrated waveguide leaky-wave antenna". In: *Antennas and Propagation (EUCAP), Proceedings of the 5th European Conference on*. IEEE. 2011, pp. 3670–3674.

[77] S. M. A. Ali, Z. Ahmed, and M. B. Ihsan. "Beam steering in HMSIW LWA at fixed millimeter wave frequency". In: *High-Capacity Optical Networks and Enabling/Emerging Technologies (HONET), 2015 12th International Conference on*. IEEE. 2015, pp. 1–2.

[78] T. Jang and S. Lim. "Novel capacitor-loaded substrate-integrated-waveguide structure and its electronically controlled leaky-wave antenna application". In: *Electromagnetics* 34.8 (2014), pp. 585–592.

[79] Keysight. *Advanced Design System (ADS)*. Keysight EEsof EDA, 2017.

[80] S. Doucha and M. Abri. "New design of leaky wave antenna based on SIW technology for beam steering". In: *International Journal of Computer Networks & Communications* 5.5 (2013), p. 73.

[81] N. Kumar et al. "A CRLH leaky wave antenna on SIW with continuous scan using novel S-slots". In: *International Journal of Electronics Letters* (2017), pp. 1–9.

[82] J. Liu, D. R. Jackson, and Y. Long. "Substrate integrated waveguide (SIW) leaky-wave antenna with transverse slots". In: *IEEE Transactions on Antennas and Propagation* 60.1 (2012), pp. 20–29.

[83] Y. F. Hou et al. “Reconfigurable Substrate Integrated Waveguide.” In: *PIERS Proceedings*. 2014.

[84] MACOM. *MA46H120 Series Datasheet*. URL: `https://cdn.macom.com/datasheets/MA46H120%20Series.pdf` (visited on 03/12/2018).

[85] MACOM. *MA46H120 ADS-Spice Diode Model*. URL: `https://cdn.macom.com/files/MAVR-000120_MA46H120SPICE-ADSModel.pdf` (visited on 03/12/2018).

[86] Y. Mohtashami and J. Rashed-Mohassel. “A butterfly substrate integrated waveguide leaky-wave antenna”. In: *IEEE Transactions on Antennas and Propagation* 62.6 (2014), pp. 3384–3388.